ROMA TRE
UNIVERSITÀ DEGLI STUDI

Dipartimento di Matematica e Fisica

Dottorato di Ricerca in Fisica - XXIX Ciclo

Slow Dynamics of Supercooled Water in Biological and Glass Forming Solutions

Insights from Molecular Dynamics

A thesis submitted in partial fulfillment of the requirements for the degree of Doctor of Philosophy in Physics

by

Gaia Camisasca

PhD Program Coordinator

Prof. Roberto Raimondi

PhD Thesis Advisor

Prof.ssa Paola Gallo

January 2017

To be defended publicly on Monday February 6, 2017.

Slow Dynamics of Supercooled Water in Biological and Glass Forming Solutions
Ph.D. Thesis Roma Tre University
Version: January 9, 2017
Author's email: camisasca@fis.uniroma3.it

Contents

Acronyms

FSC Fragile to Strong Crossover. 24, 25, 61–65, 79–81, 100, 101

HB Hydrogen Bond. 5, 6, 44, 94, 96, 97, 100, 114

HDA High Density Amorphous. 7, 12, 14

HDL High Density Liquid. 12, 14–16

LDA Low Density Amorphous. 7, 12, 14, 15

LDL Low Density Liquid. 12, 14–16

LJ Lennard-Jones. 37, 39–41, 113

LLCP Liquid-Liquid Critical Point. 12, 14, 16, 24, 25, 62

MCT Mode Coupling Theory. 16–20, 22–24, 56, 60–63, 79–81, 100, 110–112

MD Molecular Dynamics. 8, 12, 16, 29–33, 35–38, 42, 46, 49–51, 55, 57, 67

MSD Mean Squared Displacement. 17, 43, 47, 83–87

PBC Periodic boundary conditions. 33, 37, 38, 42, 45

PDT Protein Dynamical Transition. 26, 50, 66, 70, 101, 102

PME Particle Mesh Ewald method. 37

RDF Radial Distribution Function. 43, 54, 84, 85, 87–91, 93, 108, 113–120, 122, 130–133

SISF Self Intermediate Scattering Function. 17, 20, 21, 42, 46, 47, 49, 54–59, 64, 67–69, 77, 107–111

SPC/E Simple Point Charge Extended. 12, 16, 21, 37, 38, 50, 61, 63, 66, 68, 71, 107–109

TIP4P Transferable Interaction Potential with 4 Points. 12, 13, 16, 17, 37–39, 109, 111, 113, 120

TMD Temperature of Maximum Density. 9, 10, 12, 13, 38, 103

Acknowledgements

My first and sincere thanks go to my supervisor Professor Paola Gallo. She is a passionate researcher and a patient guidance. I am grateful to her for introducing me to the exciting field of supercooled water and for the support and the encouragement she gave me during the Ph.D. program. This Thesis would never have come into being without her. I owe her a lot.

Many thanks must go to Professor Mauro Rovere, for the helpful suggestions, invaluable discussions and the kindly help he offered to me during these years.

I would like to express my deep gratitude to Dr. Antonio Budano and Dr. Federico Bitelli of the Cluster Roma Tre, always generous with their advice and expertise.

I need to thank Dr. Claudio Masciovecchio for his support.

I wish to give special thanks to my friends and colleagues Margherita and Alessandro, with whom I shared this long journey. Thank you for the scientific and the non-scientific moments spent together. Your friendship means a lot for me. Wish you all the success for your upcoming future.

I would like to thank some past and current Ph.D. students: Dr. Margherita De Marzio, Dr. Alessandro Di Cicco, Dr. Paolo Lami, Dr. Enrico Maiorino, Dr. Adriana Postiglione, Dr. Gabriele Ria, Dr. Federica Ricci, Dr. Lorenzo Riggio, Dr. Giorgio Salerno. I greatly appreciate the good times we have had in Room 81 and outside.

In this moment my sincere gratitude also goes to my friends not related to work, to Ely, Marti, Gaia and Elena for their constant friendship since the days of the High School, and to Simone and Monica since the first year at the University.

Finally, I want to thank my family. A special thought goes to my grandparents. I truly cannot put into words the gratitude to my parents, Serenella and Luigi, and to my brothers, for their unconditional love and encouragement.

I dedicated this Thesis to Adalberto and Eugenio.

Roma, Jan 2017
Gaia

Introduction

Water is most fascinating. How does a such small molecule give life to our planet remains a mystery [1–5]. We perceive water as a simple and normal liquid, this is because we call normal what it is familiar to us. In the reality, from the physical point of view, water is probably the most peculiar molecule in our planet. Water in fact shows the largest number of anomalies. About ten years ago they were sixty three, five years ago they were sixty eight, up to date they are seventy four: this number does not seem to stop growing. These anomalies regard its phase, its density, its structure, its thermodynamics and its dynamics and they are encountered over all its puzzling phase diagram.

Water has a liquid metastable state with respect to the crystalline state and here water is called supercooled water. Water can be also metastable with respect to the crystal, in this case it is glassy water [6]. Bulk water at ambient pressure can be supercooled down to the limit T_H = 235 K, known as its homogeneous nucleation temperature. Glassy water can be heated up to T_g = 136 K obtaining the ultraviscous supercooled water, but it transforms, upon further heating, into cubic ice at T_x =150 K, known as its spontaneous crystallization temperature. Both T_H and T_x actually depend on pressure. Therefore there is a gap bounded by T_H from above and by T_x from below where water exists only in its crystalline solid phase: this is the so-called *no-man's land*.

Water anomalies become more evident in the low-temperature metastability regions. For instance, thermodynamic response functions rapidly increases upon decreasing temperature at ambient pressure with a universal apparent divergent temperature T = 228 K [7], inside the no-man's land. Here also a hierarchical cascade of other anomalies regarding the structure, the dynamics and the thermodynamics with different bounds appears [8].

Many have been the attempts to explain these anomalies and a number of interpretations have been proposed [5]. Among them, the presence of a Liquid-Liquid Critical Point [9] is a most fascinating hypothesis, capable to frame anomalies of water in a very elegant explanation, that gives continuity to the glassy states of water. At low temperature two glassy states of water, the low density and the high density amorphous states, are indeed divided by a first order phase transition [6]. Their coexistence line should extend into the no man's land, separating a low density liquid from a high density liquid and finally ending in a liquid-liquid critical

point. The difference between the two liquid phases vanishes at normal conditions and the ordinary liquid phase of water is found. In this scenario the second critical point of water lyes therefore at high pressure and low temperature of the phase diagram with respect to normal conditions, approximately located at a temperature T ≈ 220 K and a pressure P ≈ 100 MPa, as estimated from extrapolation of experimental results [10]. Thus deep inside the no-man's land and thus directly investigable only, up to date, through computer simulations.

Water plays a paramount role also in biology, and not by chance it has been termed *"matrix of life"* [11]. In particular, the first layers of water that hydrate macro-biomolecules like proteins, seem to play the principal role. The biochemical activity of many proteins is in fact guaranteed only if a minimal critical numbers of water molecules corresponds to each protein, i.e. the hydration level strongly influences the proteins functioning. In that respect, also the temperature influences the protein activity, which is typically absent at low temperature, where proteins are in glassy solid-like states. If they are minimally hydrated, then they suddenly restores their ability upon heating [12, 13]. This occurs in the supercooled region of water, assessing the leading role that assumes supercooled water in biology. Despite the considerable effort done by the community in this field, still there is not a complete understanding of this dynamical coupling, especially in the cooled regime, where the coupling of the protein with its hydration water is fundamental to activate its function.

The study of supercooled hydration water is also very important in more practical field like long term storage and cryopreservation. It would be desirable to store biomolecules only in supercooled water with respect other substances, because that would offer a more plasticized and naturally bio-compatible environment. Nonetheless this is not possible, because of the homogeneous nucleation of supercooled water. In general biological material is damaged by the freezing of water and thus cryoprotectants substances are usually added to water. Cryoprotectors are in fact molecules which can prevent the ice formation and therefore the damage of biomolecules at low temperature. Today the most effective cryoprotectants are cytotoxic, for example the dimethyl sulfoxide which can penetrate deep in the tissue. Thus sugars and among them the trehalose [14] are widely employed as excipients in preparing cryoprotectant solutions because of their biocompatibility. Controlling fluctuations in density and inhibiting ice formation of the water surrounding a macromolecules by the use of green substances like sugars is fundamental to improve cryopreserving protocols which can maintain ex-vivo organs and tissues and it is thus essential for medical progress.

The leitmotiv of this Thesis is supercooled water, with particular fo-

cus on its structural relaxations. The characterization upon cooling of the typical structural relaxation of supercooled water, the α-relaxation, is framed within the Mode Coupling Theory of glassy dynamics. This investigation has been done in supercooled bulk water and when water is in different local environments: supercooled water at the protein interface and supercooled water in contact with salty ions.

A total of four systems have been investigated in this work. The first system is composed by a lysozyme protein immersed in water. The second system is a ternary system containing a lysozyme protein immersed in a trehalose-water solution. In these two systems we focused the analysis on the dynamics of the protein hydration water. The third system is a box of bulk water, needed for comparing the results of hydration water. Finally, the fourth system is a glass forming water solution, the $LiCl{:}6H_2O$ system. The temperature behavior of the α-relaxation of water and, in the case of bio-systems, the onset of new relaxational phenomena of supercooled water at the protein interface have been characterized in this work. Structural properties and water hydrogen bonding behavior have also been investigated in the four systems.

In the following we illustrate the structure of this Thesis.

In **Chapter 1**, we present the general context and the scientific background in which our studies are performed. The main features of the water molecule, comprehending its hydrogen bond network, phase diagrams of stable and metastable states are presented. A description of the water anomalies, with particular regard to those happening in the supercooled region, indroduces the scenarios proposed to explain their appearance, the LLCP scenario is treated in greater extent. The central part of the Chapter is devoted to the slow dynamics of water in the supercooled regime, here we present the phenomenology and the theory describing the slow dynamics of water. The thermodynamic connection with the LLCP is also outlined. The relevant features happening in the supercooled regime and related issues as seen from the biological point of view are finally presented in the last Section.

In **Chapter 2** we illustrate the methodology used in this work. The main elements of the MD technique are firstly described. This is followed by the general description of how MD handles interaction potentials between the system constituents. We then describe in details the potentials force fields used to model our systems in the simulations. Finally, the observables calculated from the MD trajectories are presented, both from the physical and computational point of views.

Chapter 3 deals with the protein hydration water relaxations in the system composed of one lysozyme immersed in pure water. After a brief introduction on the state of the art on relaxation processes of hydration water, the specific simulation details for our system, together with its de-

scription, are given. Then we show the results on the characterization of the dynamics of hydration water. Firstly we present the density-density correlation functions and then we analyze the temperature behavior of the structural relaxation times of hydration water. Then the internal dynamics of the protein is investigated and the dynamical transition is detected for our lysozyme. Dynamical crossovers of relaxation times are discussed in relation with this last feature. The last Section is devoted to conclusions.

In **Chapter 4** we present the second simulated bio-system, the lysozyme immersed in a trehalose-water solution, and the description of the specific simulation details for this system. In this Chapter, all the results are presented through a comparative study of this system with the lysozyme immersed in pure water and bulk water. First, we report the results on the dynamics of hydration water and on the internal dynamics of lysozyme. This is done, in analogy to what done in the previous Chapter, through the calculation of density-density correlation functions of hydration water, the temperature analysis of relaxation times and the determination of the protein dynamical transition of lysozyme. We conclude our dynamical characterization of hydration water by presenting the mean squared displacement of the water molecules in both the hydration layer of the protein and in bulk system. Then we present the structural analysis of the protein systems, in terms of number density and pair correlation functions of water and trehalose molecules as a function of the distance from the protein. Finally we characterize the hydrogen bond networks of protein hydration water, when and when no trehalose is present in the system, and compare these results with the network of bulk water. The last Section is devoted to conclusions.

Chapter 5 deals with the glass-forming $LiCl{:}6H_2O$. We review the phase diagram of lithium-chloride and water solutions, with particular regard to our specific solution. We then provide the simulation method details for the set of simulations run on this system. Results on the structural α-relaxation of the water contained in this glass-forming liquid are presented and discussed within the MCT. This is followed by the results of the structural properties of the whole system in terms of water-water, water-ion and ion-ion pair correlation functions. Finally, results on the water hydrogen bond network are presented. The last Section is devoted to conclusions.

Last Chapter is devoted to the final remarks and general conclusions of the present Thesis. Outlooks are also outlined.

Appendix A contains figures of data relative to $LiCl{:}6H_2O$, not shown in Chapter 5.

Appendix B contains publications, poster presentations and oral contributions given by myself relative to the systems studied in this Thesis.

1

The Puzzling Behavior of Water

1.1. Stable and Metastable Water

Water is a small molecule made up of two hydrogen atoms covalently bonded to one oxygen atom. These atoms are stuck together in the non-linear V-shaped geometry shown in Figure 1.1. In the isolated H_2O molecule, the O-H length is 0.958 Å and the H-O-H angle is 104.5° [15], about 5° less than the pure tetrahedral angle. The valence electrons of the oxygen atom form two lone pairs, that with the two hydrogen atoms shape an approximately tetrahedral structure. The covalent O-H bonds have actually about the 33 % of ionic character, due to the different electronegativy of the two species. Consequently the two hydrogen atoms are then strongly attracted by the oxygen and move towards it, leaving the protons of the hydrogen atoms partially unscreened. This fact together with the non-linear geometry of the molecule gives a permanent molecular dipole moment of 1.85 D, directed from the center of the negative charge to the center of the positive charge. This makes water a polar molecule.

Different water molecules attract each other because the opposite charges on the oxygen and hydrogen atoms with the consequently formation of Hydrogen Bonds (HBs). Due to hydrogen bond interactions the ionic character of the covalent O-H bond decreases, and the structure of the water molecule in the liquid phase is quite relaxed with respect to the isolated molecule. At ambient condition, the O-H bond length in liquid water is 0.991 Å and the H-O-H angle is 105.5° [16].

HBs characterize the structure of water in both the liquid and the crystalline phases. The energy associated with this bond is high, circa 20 kJ/mol at ambient temperature, when compared to typical intramolecular interaction, as the dipole-dipole van der Waals of circa 1 kJ/mol. The bond is also characterized by an high degree of directionality and tends

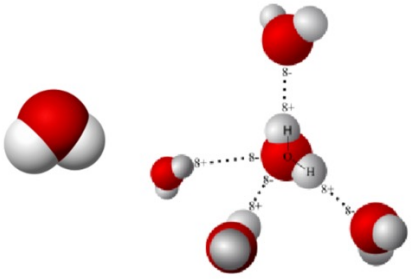

Figure 1.1: Structure of the water molecule and a picture of the tetrahedral hydrogen bond network that water locally forms.

to be linear on the O–H···O axis, where the symbol ··· indicates the HB. Water is an example where the dynamics of hydrogen bonds is cooperative: the formation of a single bond by a water molecules enhances in fact the tendency of the same molecule to form other HBs. Generally, a single water molecule can act by donating two bonds and accepting other two, for a total of four HBs. This causes the formation of an extended HB-network in liquid water, that becomes even more stable in the crystalline I_h phase, with the typical tetrahedral symmetry shown in Figure 1.1. Most of the peculiar properties of liquid water that will be covered in the following sections arise as consequences of this hydrogen bonded structure of water.

The phase diagram for the stable phases of water is shown in Figure 1.2. At ambient condition water is stable in the liquid phase. If the temperature is raised above 373 K, water becomes steam, which means that above this temperature water is stable in the gas phase. If the temperature is lowered below 273 K, it becomes ice I_h because there the stable phase is the solid one. The phase diagram of stable phases of water is indeed complex. For example, it has several triple points because of the polymorphism of crystalline water: the hexagonal ice I_h is not the only solid phase of water. Fourteen different crystalline stable phases are known today, each of them is stable in a certain $P - T$ region. For example in the shown diagram several high pressure ices are indicated.

The peculiarities of water extend over all the phase diagram. The liquid-gas critical point, for example, even if the classical theory of liquid-gas transition involves no diversification above this one, actually emanates a line that separates a more liquid-like vapor from a more gas like one [18, 19]. This line is called Widom line.

An other example of the peculiar features of the phase diagram of water, that affects our life on earth, is the negative slope of the coexistence line between the solid and liquid phases. The Clausius Clapeyron

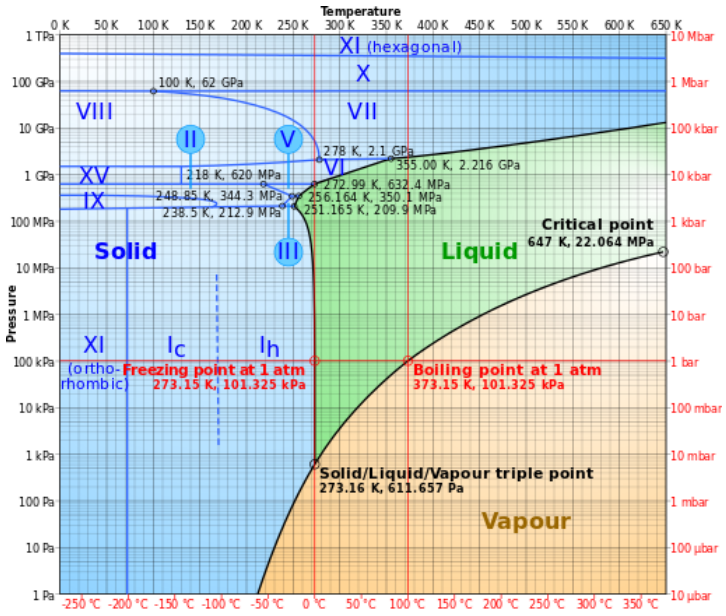

Figure 1.2: Phase diagram of the stable phases of water in the $P-T$ plane. Figure from Ref. [17].

relation, that reads:

$$\frac{dP}{dT} = \frac{1}{T}\frac{\lambda}{\Delta V} \tag{1.1}$$

where λ is the latent heat of fusion, implies that when liquid water become ice, its volume increases. Most of the substances behave on the contrary, being their solid phases denser than their liquids phases. This particular characteristic of water is related to another anomaly, called *density anomaly* that will be discussed in the next section.

If we consider also metastable phase states of water, the phase diagram becomes even more complex. Four crystalline ices of water are metastable, for example the Ice I_c is a metastable form of ice that can be formed by condensation of water vapor at ambient pressure and at a temperatures less than 193 K.

Water also has three distinct forms of solid amorphous ice. The High Density Amorphous (HDA) ice and the Low Density Amorphous (LDA) ice are two glassy states of water separated by a first order phase transition and confined to the low temperature part of the space diagram [6], see Figure 1.3. The third amorphous ice, the Very High Density Amorphous, is less known.

In the same Figure are also drawn the boundaries of the liquid metastable phase of water: liquid water can be supercooled below the melting temperature $T_M(p)$ down to the temperature of homogeneous nucleation $T_H(p)$. Below this temperature supercooled liquid water *rapidly* becomes ice. It

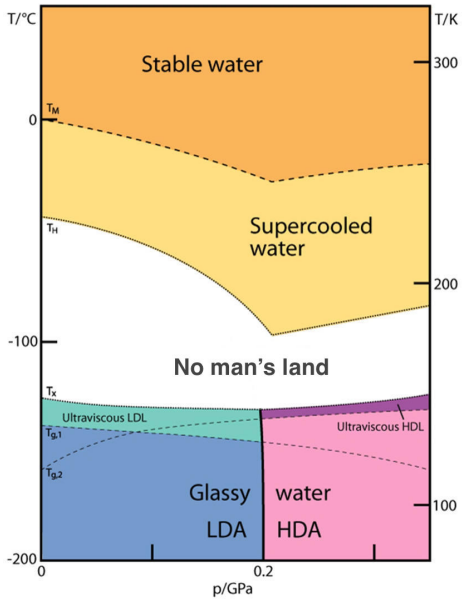

Figure 1.3: Schematic representation in the $p - T$ plane of the metastable phase diagram of supercooled and glassy water. Figure adapted from Ref. [5].

must be noted that the homogeneous nucleation temperature is a kinetic limit and not a thermodynamic one. As thus it can be considered as a practical limit, function of the cooling rate and of the observation time [2]. The other two, named ultraviscous liquid metastable phase of water, are bounded by the glass transition temperature of water $T_g(p)$ from below and by the temperature of spontaneous crystallization $T_x(p)$ from above, at which the ultraviscous liquid turns into ice. The interval between the homogeneous nucleation temperature $T_H(p)$ and spontaneous crystallization temperature $T_x(p)$ is the so-called *no man's land*. The name comes evidently from the fact that ice nucleation prevents any attempts to keep water in a liquid state inside this region. This fact is indeed true with respect to the available experimental techniques. The existence of metastable liquid water below the homogeneous nucleation temperature is not in principle forbidden by thermodynamic constraints [2]. Molecular Dynamics (MD) simulations typically can enter inside the no-man's land, thanks to the very fast cooling rates this technique reaches.

1.1.1. The Anomalous Properties of Water

Water, the most abundant liquid in our planet, is probably also the most anomalous liquid. At least 74 properties of water are indeed quite different from those expected from a simple liquid [20]. Actually water behaves in quite different way from high to low temperatures and anomalies are encountered all over the phase diagram. It is the intra-

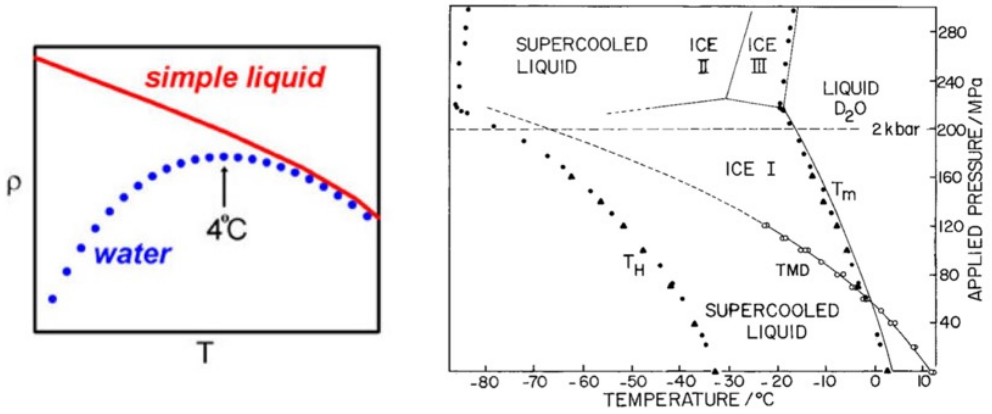

Figure 1.4: Left Panel: Temperature trend of density in water and in normal liquids. Figure from Ref. [5]. TMD line for D_2O in the $p - T$ plane. Circles are from experiments and the line is a low temperature extrapolation. $T_M(p)$ is the melting line and $T_H(p)$ the locus of homogeneous nucleation. Figure from Ref. [21].

molecular hydrogen bonding structure that determines the highly complex and anomalous behavior of water. Anomalies regard its density, rheological properties, thermodynamics and physical chemical properties.

The *density anomaly* is probably the most known counterintuitive property of water because it affects our every-day life. It is usual for liquids to contract upon decreasing temperature. Conversely, at ambient pressure, the density of water does not increase monotonically with decreasing temperature, but it shows a maximum at T = 277 K. When pressure is varied, the maximum occurs at a different temperature. Drawing the position of all these maxima on the phase diagram, results in a line called the Temperature of Maximum Density (TMD) line. In Figure 1.4 the experimental TMD of D_2O is shown. As anticipated in Sec. 1.1, this anomaly is connected to the negative slope of the liquid-solid coexistence line.

At a temperature below the TMD, water must show a minimum in its density if no phase change occurs, i.e. supercooled water has a mininum in density, since the density of deeply supercooled water is lower and increases with decreasing temperature. This minimum should lie inside the no-man'd land and its estimation is 203 K [22]. The density minimum in deep supercooled water has been observed in computer simulation studies [23] and in deep supercooled confined water has been observed experimentally [22, 24].

Figure 1.5 shows the different behavior of the thermodynamic response functions of water when compared to simple liquids. It is shown,

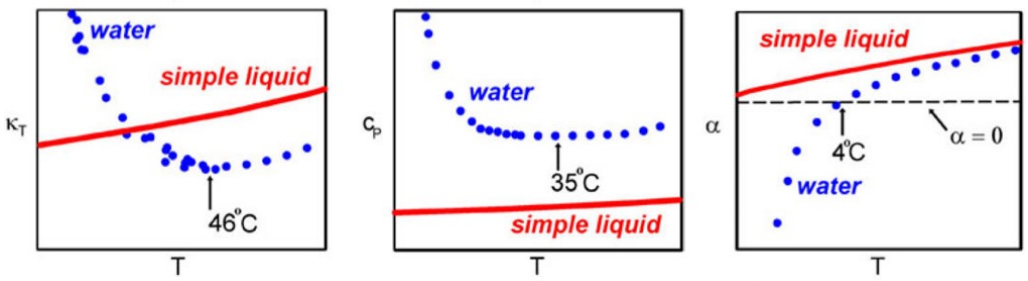

Figure 1.5: Temperature trends of isothermal compressibility κ_T, isobaric specific heat c_p and coefficient of thermal expansion α_p in water and in normal liquids. Figures adapted from Ref. [5].

from the left to the right, the isothermal compressibility κ_T, the isobaric specific heat c_p and the coefficient of thermal expansion α_p.

These quantities are defined by the relations:

$$\begin{aligned} \kappa_T &= -\frac{1}{V}\left(\frac{\partial V}{\partial p}\right)_T \\ c_p &= \frac{T}{N}\left(\frac{\partial S}{\partial T}\right)_P \\ \alpha_p &= \frac{1}{V}\left(\frac{\partial V}{\partial T}\right)_p \end{aligned} \tag{1.2}$$

and they are connected to the fluctuations of volume and entropy by the equalities:

$$\begin{aligned} \langle(\partial V)^2\rangle &= V k_B T \kappa_T \\ \langle(\partial S)^2\rangle &= N k_B c_p \\ \langle \partial V \cdot \partial S\rangle &= V k_B T \alpha_p \end{aligned} \tag{1.3}$$

In a simple liquid, κ_T and c_p decrease monotonically upon decreasing temperature, in water they show a minimum at T = 319 K and T = 308 K respectively. At a fixed pressures α_p becomes zero in water in coincidence of the TMD and then becomes negative and rapidly decreases. In a simple liquid α_p is expected to decrease monotonically with decreasing temperature, but remaining greater than zero. Upon further decreasing temperature all the three response functions depart most from the normal liquid behavior, increasing or decreasing rapidly toward the deep supercooled region. Besides their steep increase upon cooling can be described by a power law [7, 25] given by:

$$X \sim \left(\frac{T}{T_S} - 1\right)^{\lambda_X} \tag{1.4}$$

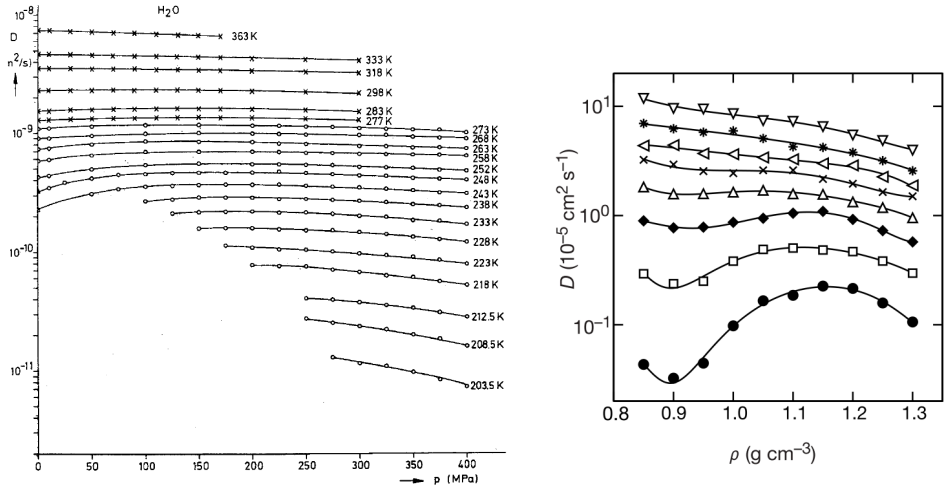

Figure 1.6: Left: Experimental self-diffusion coefficient D of water as a function of the pressure along different isotherms. Figure from Ref. [26]. Right: Density dependence of the D along isotherms for SPC/E water showing also diffusivity minima. Figure from Ref. [8].

where X is the generic response function, T_S the divergent temperature and λ_X the associated exponent to the divergent quantity X. At $p = 1$ bar, the estimated divergent temperature is $T_S = 228$ K, the same for all the response functions. Since T_S is nine degrees below T_H, the divergences of thermodynamic response functions should take place inside the no-man's land, consequently they named after *apparent divergences*.

The *diffusion anomaly* is an example of the anomalies regarding the dynamics of water. See Figure 1.6. In simple liquids the diffusion coefficient is expected to decrease upon increasing compression. At a variance with this behavior, at $T \sim 283$ K the diffusivity of water increases upon increasing the pressure until a maximum is reached (P $\approx$ 150 Mpa at that temperature). In computer simulations, it has been shown that upon further decreases temperature, the diffusivity restores the normal behavior, so it passes through a minimum. Maxima and minima of the diffusivity can be joined drawing a line of diffusivity extrema.

It has been shown in theory and computer simulations [8, 27, 28] that thermodynamic and dynamic anomalies of water are accompanied by structural anomalies. The structural anomalies region was defined considering two order parameter, q and t [8]. The orientational parameter q gives a measure of the degree of tetrahedrality of the arrangement of four first nearest neighbor water molecules, the translational parameter t measures the tendency of two water molecules to adopt a preferential separation. The decreases of translational and orientational orders upon compression is called the *structural anomaly*, since normal liquids

behaves in reverse with increasing order upon compression.

The relationship between the structurally, dynamically and thermodynamically anomalous regions has been clarified firstly by Errington and Debenedetti [8]. They showed that the regions of thermodynamic anomalies is encompassed by the region of dynamical anomalies, which is in turn encompassed by the wider region of structural anomalies studying SPC/E water. Figure 1.7 displays these regions of anomalies of SPC/E water in the $\rho - T$ plane. The structurally anomalous region of water is bounded by the loci of q maxima and t minima and corresponds in the Figure to the region included below the outer drawn line. There, water becomes more disordered when compressed. Inside this region, lies the dynamically anomalous region bounded by the loci of diffusivity minima and maxima: there the diffusion coefficient of water increases if the density increases. Finally, enclosed inside by the dynamically anomalous region, the thermodynamically anomalous region lies. In this region, defined by the TMD, the density of water decreases upon cooling at constant pressure. Similar findings have been found for the TIP4P model of water, these are shown in the bottom part of the same Figure.

The picture that comes out is that anomalies of water occur as a cascade of different phenomena that are more pronounced toward the deep supercooled region.

Scenarios for Supercooled Water

As seen in the previous Section, the anomalous behavior of water is more pronounced in the deep supercooled region. Several scenarios have been proposed to explain the observed behavior of water. These comprehend the *stability limit conjecture* [25], the Liquid-Liquid Critical Point (LLCP) by Poole et al. [9] the *critical point free* scenario by Poole et al. [30] and the *singularity free* scenario proposed by Sastry et al. [31]. We focus on the LLCP.

1.1.2. The Liquid-Liquid Critical Point

In the seminal 1992's paper of Poole et al. [9], the existence of a LLCP was deduced by a series of simulations of water modeled with the ST2 potential, a five sites rigid potential of water. The study was actually aimed to investigate in MD simulations the *Speedy's stability limit conjecture*. In fact their results were suggesting a different scenario, involving a second critical point of water, located in the deep supercooled region of ST2 water, uncorrelated with the liquid-gas (first) critical point of water.

In Figure 1.8 the putative phase diagram of water, according to the up to date LLCP scenario, is shown.

The idea is that two distinct liquid phases in the deep supercooled region exist, the Low Density Liquid (LDL) and the High Density Liquid (HDL), corresponding to the experimentally observed LDA and HDA

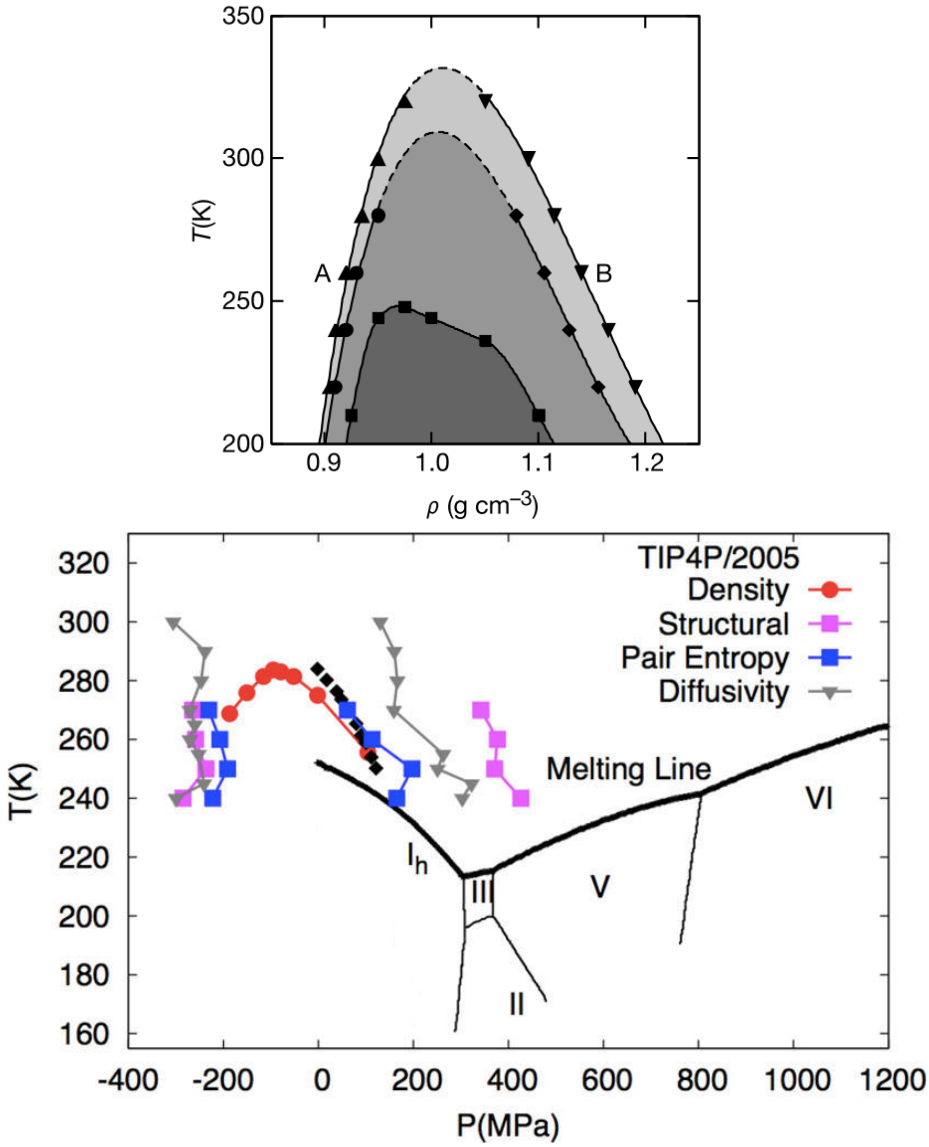

Figure 1.7: Relationship between structural, dynamic and thermodynamic anomaly region of SPC/E water (Upper panel) and TIP4P/2005 water (Bottom panel). The structurally anomalous region of water is bounded by the loci of q maxima (upward pointing triangles in the upper panel) and t minima (downward pointing triangles in the upper panel) (both magenta squares in the bottom panel). The dynamically anomalous region bounded by the loci of diffusivity minima (circles) and maxima (diamonds) (grey downward pointing triangles below). The thermodynamically anomalous region is defined by the TMD (black squares up and red circles below). Data and Figure from ref [8]. Right Panel. Relationship between structural, dynamic and thermodynamic anomaly region of TIP4P/2005 water. Also in this model of water the structural anomalous region encompassed the other two. Note that this rigid potential correctly reproduces the TMD of real water. Figure adapted from Ref. [29].

states of water, respectively. The two liquid phases are separated by a first order phase transition, in analogy to the first order phase transition experimentally detected for their amorphous phase counterparts (see Sec. 1.1). The coexistence line ends in a LLCP, located at positive high pressure and low temperature, deep inside the no-man's land. From the LLCP a line of the thermodynamic response function is emanated, the so called Widom line, that in analogy of the Widom line of the liquid-gas critical point, can be thought as an extension of the coexistence line in the one phase region [32].

The presence of a LLCP gives explanations to the anomalies of water outlined in the previous Section [33]. Apparent divergences of the thermodynamic response functions are explained with the progressive increase of the correlation length upon approaching the coexistence line or Widom line, that eventually diverges at the critical point. The anomalous properties of liquid water at higher temperatures with respect to the supercooled ones, can be also framed in this scenario as consequences of long range fluctuations reminiscence of the presence of the LLCP.

In the work of Poole et al. [9], the evidence of the existence of LLCP came out from four points: (i) low-temperature isotherms showing inflection point at $\rho_c \approx 1$ g/cm^3, which increases in strength toward lower temperatures; (ii) observation of two distinct phases below the estimated critical point, one of them structurally more resembling the structure of the HDA and the other one more resembling the structure of the LDA states of glassy water; (iii) observation of the phase transition HDL-LDL in a simulated isothermal compression experiment plus validation of ST2 model of water at low temperature (observation of the phase transition HDA-LDA at 77 K); and (iv) validation of ST2 model versus experimental results above the no-man's land (quantitative reproduction of the maxima of ρ, κ_T, c_p). With successive works they located the LLCP in ST2 water at $T_C \approx 235$ K, $P_C \approx 200$ MPa, $\rho_C = 1$ g/cm^3.

The four points were robust, so that the scientific community working in the field of water fervently gave its feedback to Poole et al.'s works. In successive years, much work has been done from the experimental, theoretical and computational physics communities to enrich the scenario proposed and to contribute to what it is the today version [2, 6, 8, 9, 34]. All the important contributions on the implication of a LLCP in the phase diagram of supercooled water, as well as supporting and contesting works have been reviewed this year by Gallo et al. [5]. Farther on we resume some important issues related to this.

Experimental investigation of water in the deep supercooled region is hampered by the homogeneous nucleation toward ice phases, as already said. Nonetheless also several experiments sustained the LLCP scenario. Among these, it must to be mentioned the experiment performed by

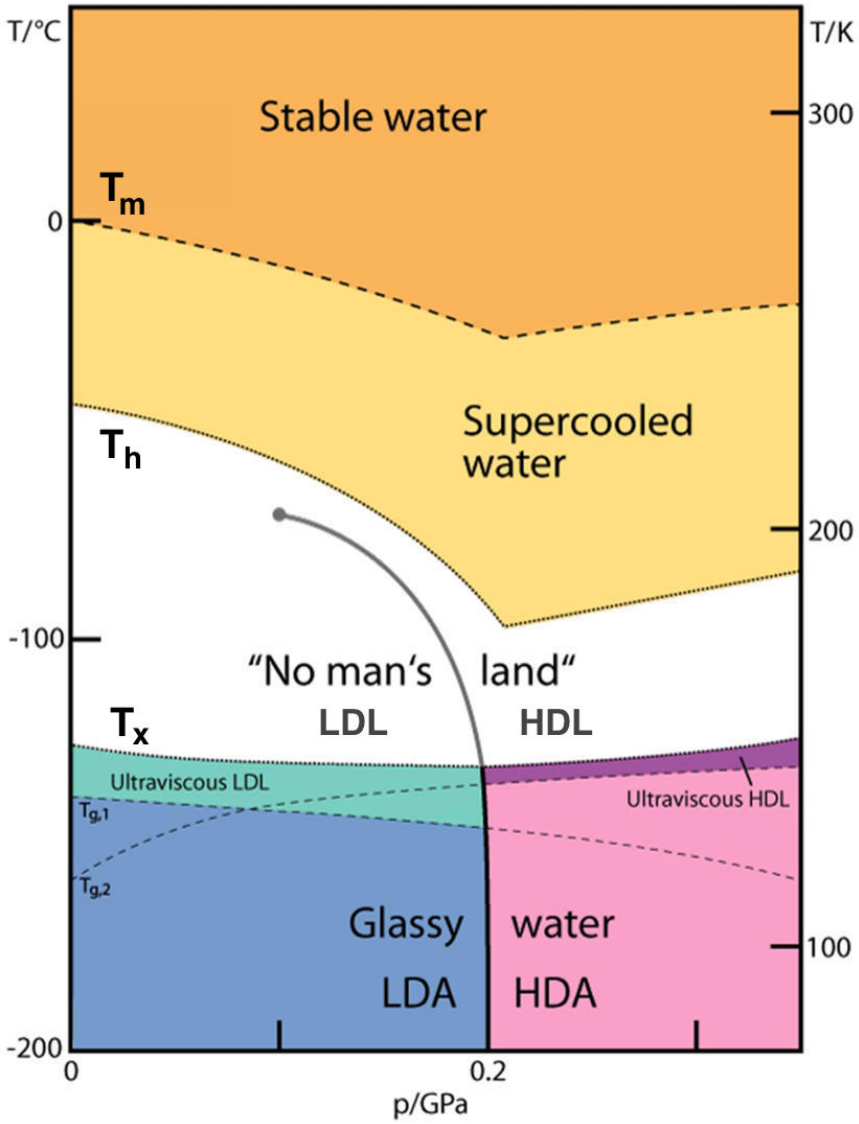

Figure 1.8: The phase diagram of the non-crystalline forms of water showing the second, liquid-liquid critical point, C, and the coexistence line along which LDL and HDL coexist inside the no-man's land. At low enough temperatures, both the liquid phases become structurally arrested into their corresponding glassy forms (LDA, LDA). Lines T_H is the homogeneous ice nucleation locus from above and T_X denotes the temperature of spontaneous crystallization from below. These lines enclose the no-man's land. From the negative slope of the LDL-HDL coexistence line, the LDL is expected to be less denser than the HDL. Figure adapted from ref. [5]

Mishima and Stanley [6, 10], who, studying the decompression–induced melting of different high–pressure crystalline phases of water in oil emulsion, claimed to detect the transition to either LDL and HDL before crystallization took place. They also located the LLCP of water at T_C = 220 K and P_C =100 MPa, which is today generally considered the estimated position of the liquid-liquid critical point of bulk real water (the one reported in Fig. 1.8).

Computer simulations played a paramount role in this context, not only because, as already mentioned, the LLCP hypothesis was based on a computational work, but because computer simulations overcome the experimental issues related to crystallization, through fast cooling rates, and thus permit to enter the no-man's land. The LLCP location has been, up to date, located in the supercooled region of the phase diagram of water simulated with several different potentials. These include variants of ST2, TIP4P and TIP5P potentials (See Ref. [5] and Refs. therein). The phase diagram of SPC/E potential was shown to be consistent with the presence of a LLCP [35] and its location was estimated on free energy–based calculations [36].

It must to be highlighted also the contribution of MD simulations in the opening of experimentally viable routes aimed to the detection of the liquid-liquid transition or its signature. Following their example, several experiments are performed on supercooled water in confinement, nanodroplets, water at negative pressure and water solutions of salts.

Finally, particular relevant is the Widom line issue. Widom line flow close to the upper bound of the noman's land, the temperature of homogeneous nucleation of water. So, if water is supercooled from above toward the noman's land, the Widom line is the first detectable feature that one encounters upon cooling and that indicates the presence of the LLCP. This point is very important, and it will be discussed again in the next Section, where the connection with the translational dynamics of water is outlined.

1.2. Slow dynamics in supercooled regime

In this Section the Mode Coupling Theory (MCT) aspects relevant for interpreting the slow dynamics are addressed, together with the important phenomenology of water and glass forming liquids at low temperatures.

1.2.1. Stretched Dynamics of Water and Features of Mode Coupling Theory

The most general feature of supercooled or glassy dynamics is the stretching of time–correlation functions and excitation spectra over intervals of time or of frequency, respectively [37]. Stretching phenomena

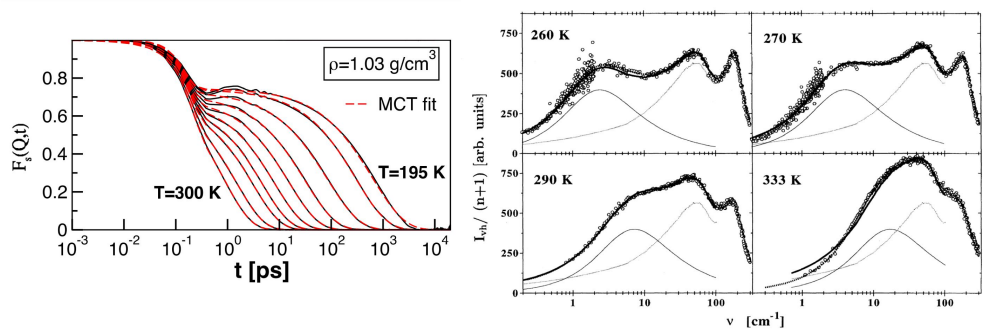

Figure 1.9: Oxygen-oxygen Self Intermediate Scattering Function (SISF) of TIP4P/2005 water showing the two step relaxation, calculated at Q = 2.25 Å^{-1}. Solid lines are calculated according to Eq. (1.16). Figure from Ref. [38]. Right panel: depolarized light scattering spectra of water at different temperatures and their approximation (thick solid line). The spectra of the α-relaxation (thin solid line) and of the fast dynamics (dotted line) are also shown. Figure from Ref. [39]

can extend over several orders of magnitude upon decreasing temperature. An example of this behavior in both time and frequency domains is given in Figure 1.9.

MCT provides a quantitative explanation for the observed behavior of correlators. The central quantity in MCT is the normalized density-density correlation function:

$$\phi_q(t) = \frac{\langle \rho_q^*(t)\rho_q \rangle}{S_q} \tag{1.5}$$

where $S_q = \langle |\rho_q|^2 \rangle$ denotes the static structure factor, but the theory adapts to any other correlator that has a nonzero overlap with density, like the self part of (1.5), i.e. the Self Intermediate Scattering Function (SISF), the Mean Squared Displacement (MSD) and so on. The same it is true for their Fourier and Laplace transforms.

The basic idea of the MCT is the transient trapping of a particle by its nearest neighbors. This is known as the *cage effect*. As the temperature of the system is lowered at constant pressure, the trapping occurs for an increasing lapse of time and eventually, in the idealized version of the theory, it leads to structural arrest at the MCT temperature $T_{MCT}(p)$.

MCT describes the evolution of the correlator $\phi_q(t)$, which is controlled by a non linear feedback mechanism, formalized by a retarded memory function entering in the generalized Langevin equation for $\phi_q(t)$ [37]. Let's see some keys points of the formalism.

$\phi_q(t)$ obeys to the generalized oscillator equation:

$$\ddot{\phi}_q(t) + \Omega_q^2 \phi_q(t) + \Omega_q^2 \int_0^t M_q(t-t')\dot{\phi}_q(t')dt' = 0 \tag{1.6}$$

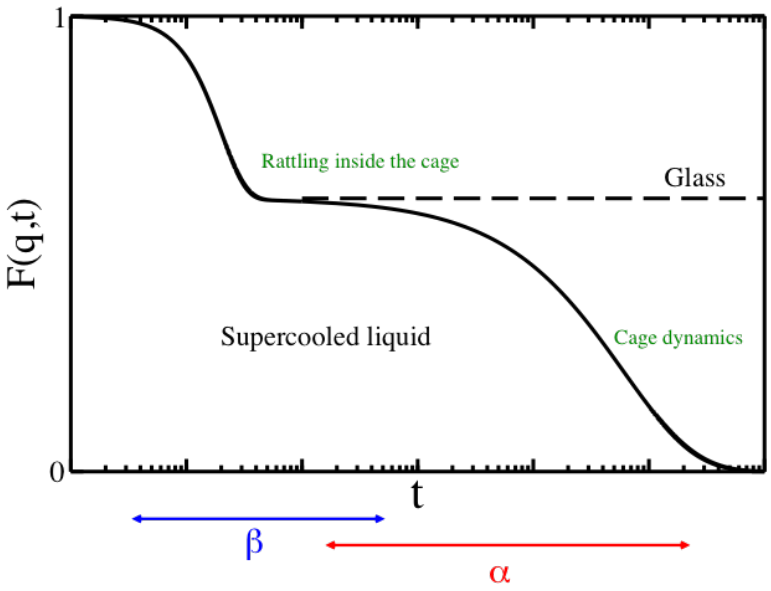

Figure 1.10: Behavior of the generic correlator ϕ_q with non-zero overlap with density, described by the MCT.

where $\Omega_q = (v^2q^2/S_q)^{1/2}$ is the microscopic frequency, and $v = (k_bT/m)^{1/2}$ is the thermal velocity of the particle. The memory function $M_q(t)$ is expressed as a sum of a constant friction γ_q representing the fast dynamics (high frequency) processes in the liquid and a time-dependent friction coefficient $m_q(t)$ reflecting relaxational processes:

$$M_q(t) = \gamma_q\delta(t) + m_q(t) \quad . \tag{1.7}$$

In the frame of the idealized version of the theory, $m_q(t)$ is the decisive term, and it is described by contributions stemming from interactions between pairs of density fluctuations:

$$m_q(t) = \frac{1}{2}\sum_k V_{k,q-k}\phi_k(t)\phi_{q-k}(t) \tag{1.8}$$

In this way Eq. (1.6) becomes mathematically closed and can be solved, numerically, once provided the coefficients $V_{k,q-k}$ that couple the modes. These are expressed in terms of static correlation functions, like the structure factor $S(q)$. The temperature enters the theory via the temperature dependence of $S(q)$.

MCT predicts that above the $T_{MCT}(p)$, $\phi_q(t)$ decays through a two step relaxation, displaying a fast and a slow decay to zero. With the fast relaxation $\phi_q(t)$ reaches a plateaux value f_q, called nonergodicity parameter. Then $\phi_q(t)$ is allowed to decay to zero only when the slow relaxation

is completed. Besides, upon approaching $T_{MCT}(p)$ from above the slow relaxation greatly separates on the time scale from the fast relaxation which is approximately constant in temperature. The region where $\phi_q(t)$ approaches f_q is called β-relaxation regime, see Fig. 1.10, while the long time decay it is called α-relaxation regime. MCT predicts that the time scale of the β-relaxation, t_ϵ, has the form:

$$t_\epsilon = t_0|\epsilon|^{\frac{1}{2a}} \tag{1.9}$$

where t_0 is a microscopic time and $\epsilon = \frac{T-T_{MCT}(P)}{T_{MCT}}$ the distance parameter.

In the early β-regime, i.e. the initial part of the plateaux, $\phi_q(t)$ has the power law behavior:

$$\phi_q(t) - f_q \propto t^{-a} \tag{1.10}$$

and that on the late-β/early-α regime, i.e. when $\phi_q(t)$ departs from the plateaux region, $\phi_q(t)$ has the power law behavior:

$$f_q - \phi_q(t) \propto t^b \tag{1.11}$$

Also the relevant scale time of the α-relaxation follows a power law, being its form given by:

$$\tau_\alpha = t_0|\epsilon|^{-\gamma} \tag{1.12}$$

a, b and γ are parameters of theory, typically dependent on pressure [40], related by the transcendental equation:

$$\frac{\Gamma^2(1+b)}{\Gamma(1+2b)} = \frac{\Gamma^2(1-a)}{\Gamma(1-2a)} \tag{1.13}$$

where Γ is the gamma function and $0 < a < 0.5$ and $0 < b < 1$ and the relation:

$$\gamma = \frac{1}{2a} + \frac{1}{2b} \tag{1.14}$$

The parameter b is also called the von Schweidler exponent.

MCT also predicts the time-temperature superposition principle, i.e. the fact the that correlators rescaled by the relevant temperature dependent time scale $\tau_\alpha(T)$ collapse in to a master curve Ψ in the α-relaxation regime (slow part of correlators):

$$\Psi(t) = \phi(t/\tau_\alpha) \tag{1.15}$$

Upon approaching T_C from above, the dynamics become more and more slow until the α-relaxation time in Eq. (1.12) diverges and the transition to a non-ergodic phase takes place. Correspondently $\phi_q(t)$ settles on the value of the plateau value f_q ceasing to decay. Generally speaking, this non-ergodic phase, characterized by structural arrest, is what we call a glass. In most liquids few degrees above T_{MCT} new relaxational

mechanisms, called hopping phenomena, set on and particles can escape the cage of nearest neighbors by jumping towards outer coordination shells. Those temperature-activated hopping phenomena, included in the extended MCT and described also by Goldstein [41], smear out the divergence of the α-relaxation time and dominate the dynamics under T_{MCT}, allowing the correlator $\phi_q(t)$ to relax to zero also below T_{MCT}. As a consequence, the predictions of the idealized MCT are expected to be valid on approaching T_{MCT} only from above for those system for which hopping phenomena restore ergodicity, like, we will see, water. When also hopping is frozen, ergodicity is lost and the system become a glass.

The success of the theory was based on clear prediction of scaling laws that could be verified on both experiments and simulations.

In summary, MCT predicts that density fluctuations decays via a *two step* relaxation process, and the blocking of the motion of any particle by its surrounding particles is the microscopic origin of the slowing down of the structural α-relaxation. The behavior *à la MCT* has been firstly observed in hard and soft spheres, Lennard-Jones spheres and binary mixtures of soft spheres and of Lennard-Jones particles [37], then in water by Gallo et al. [42].

In Figure 1.11 we show a example of the oxygen-oxygen SISF of water showin the *two step* relaxation process and the *cage effect* upon cooling. The curves are calculated at different temperatures on SPC/E [42]. The shape of the SISF of supercooled bulk water was modeled according to MCT by Gallo et al. [42] and Sciortino et al. [43]. To take into account both the fast sub-picosecond relaxation and the α-relaxation and thus reproducing the two-step behavior of the SISF, they used the following functional form:

$$F_s(q,t) = (1 - f_\alpha)e^{-(t/\tau_s)^2} + f_\alpha e^{-(t/\tau_\alpha)^{\beta\alpha}} \tag{1.16}$$

The Gaussian function with time constant τ_s takes into account the initial ballistic motion inside the cage, the stretched exponential function, known as the Kohlrausch-Williams-Watts function, takes into account the structural α-relaxation, with time constant τ_α and the stretching parameter β_α. As seen from the inset, $\beta_\alpha < 1$ indicates stretched dynamics. In the case of SISF, the ergodicity parameter f_α is the Lamb-Mössbauer factor, the analogous of the Debye-Waller factor for single particle dynamics.

Length scale for probing dynamics

According to [37, 44], the most important contribution to Eq. (1.8) comes from fluctuations with wavevectors of microscopic size, with q close to the first peak of the structure factor. This is because the microscopic mechanism of structural relaxation proposed by the MCT is

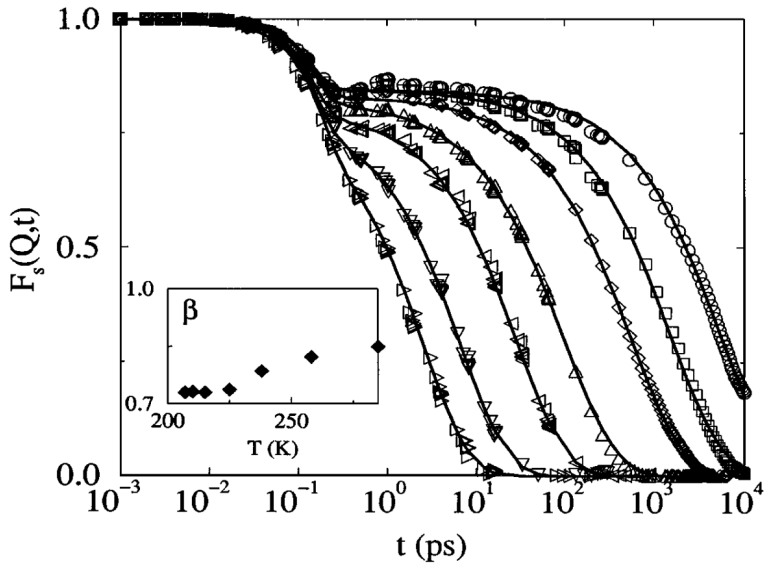

Figure 1.11: Oxygen-oxygen SISF of SPC/E water showing the two step relaxation, calculated at Q = 2.25 Å^{-1}. Solid lines are calculated according to Eq. (1.16). The inset shows the $T-$dependence of the exponent β associated with the slow α-relaxation. Figure from Ref. [42].

based basically on the interaction with first nearest molecules, so that fluctuation of density on particle distances of the order of the nearest and next-nearest neighbor shells are the most relevant ones for possible structural arrest. In that respect, water is typically probed at $q_{max} = 2.25$ Å^{-1}, which approximately corresponds to the first peak of the structure factor. The fact that this particular wavevector contributes the most in the slow dynamics also influences light scattering experiments, that, although probing very low q values, can extract correct $\tau_\alpha(q_{max})$ because the experimental spectra are due to the second-order scattering described by the self-convolution over frequency of the structure factor $S(q_{max}, \omega)$ [45].

1.2.2. Strong and Fragile liquids

Supercooled liquids appear to fall into two broad classes proposed by Angell [46]. The difference is based on the behavior of the viscosity or of the relaxation time of the liquid upon cooling toward the glass transition temperature. This difference is evident when these quantity are plotted in a Arrhenius fashion shown in Figure 1.12. The temperature axis is scaled by the glass transition temperature, typically is chosen to be that at which the viscosity reaches 10^{13} Poise, the relaxation time reaches $10^{2,3}$ s or the calorimetrically determined one. From both the Figures,

two patterns are seen: liquids exhibiting Arrhenius behavior over the entire temperature range are named strong, liquids exhibiting deviation from the Arrhenius behavior are termed fragile.

Strong glass formers, such as SiO_2 and GeO_2, are covalently bonded, network-forming liquids with tetrahedrally coordinated structures that persist across the glass transition. Arrhenius plots are essentially linear for these liquids, implying that transport in the liquid is largely governed by thermally activated processes or "barrier hopping" [26]. The structural relaxation time of strong liquids, as well as their viscosity, can be therefore describe by the following Arrhenius law:

$$\tau_\alpha = \tau_0 \exp\left[\frac{E_A}{k_B T}\right]. \tag{1.17}$$

In fragile liquids, at strict variance to strong liquids, any remnants of the structure in which a fragile liquid has vitrified, disappear upon heating. Fragile liquids can be described by relaxation times that follows the Vogel-Fulcher-Tamman (VFT) law, given by:

$$\tau_\alpha = \tau_0 \exp\left[\frac{DT_0}{T - T_0}\right], \tag{1.18}$$

where τ_0, D and T_0 are constants. T_0 is often referred as the temperature of *ideal* glass transitions, but its relation with the real glass transition temperature is highly debated [2] and in general this doesn't coincide with the real glass transition of the system, typically it is lower. D is the fragility parameter whose variations between 5 and 100 can described supercooled liquids from fragile to strong extremes in the Angel plot [46].

Equivalently, relaxation times (and viscosities) of fragile liquids can be described via the MCT power law:

$$\tau_\alpha = \tau_0 (T - T_{MCT})^{-\gamma} \tag{1.19}$$

It is to be underlined that, generally speaking, the *ideal* glass transitions temperature, T_0, and the mode coupling temperature, T_{MCT}, do not coincide. Their typical ordering, with respect to the glass transition and the melting temperature of a glass forming liquid, is shown in Figure 1.13.

1.2.3. Connection with the thermodynamics: Widom Line and Fragile to Strong Crossover

Water is anomalous also in respect to the classification introduced by Angell. As seen from the Figure 1.12, the curvature of viscosity of water effectively seems to be more pronounced with respect to other liquids. The experimental investigation at lower temperature is indeed hampered

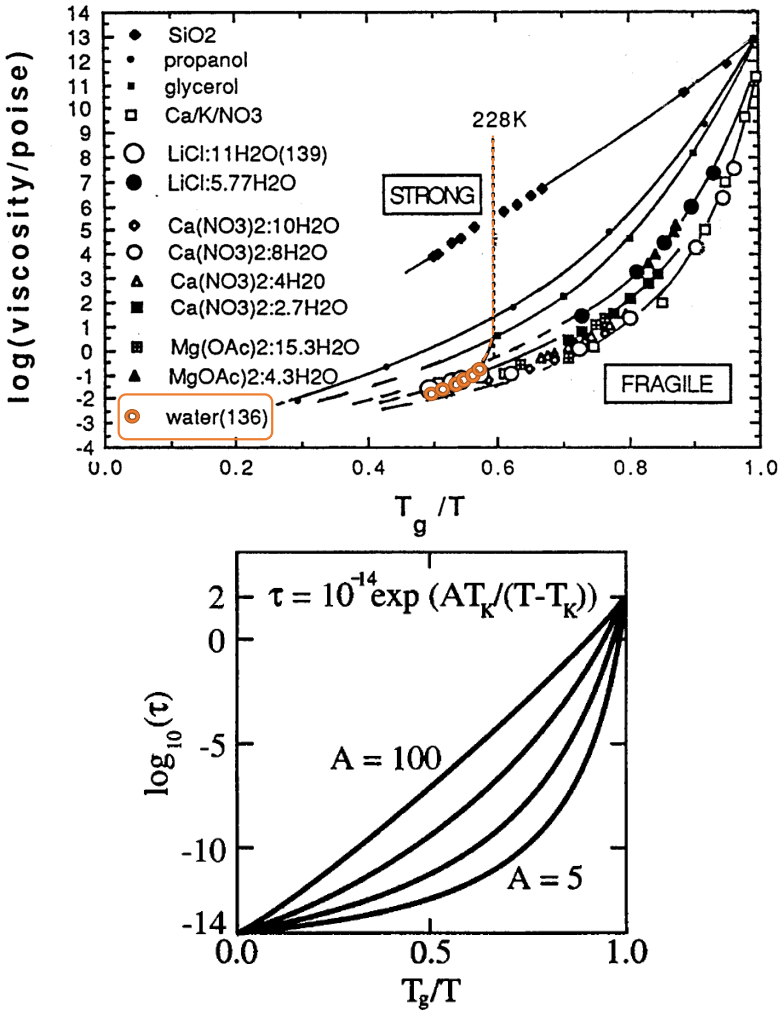

Figure 1.12: Angell plots of viscosity (upper panel) and structural relaxation time (bottom panel) of glass-forming liquids. Figures from Ref. [46] (upper) and from Ref. [26] (lower).

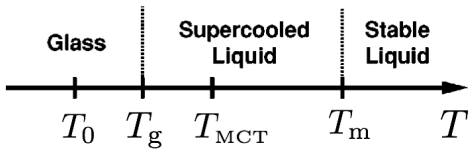

Figure 1.13: Relative values for glass-forming liquids of the melting temperature T_m, the temperature T_{MCT} of structural arrest in MCT appearing in Eq. 1.19, the experimentally defined value of the glass transition temperature T_g and the temperature T_0 appearing in the VFT form of Eq. 1.18. Figure adapted from Ref. [40].

in bulk water by the homogeneous nucleation. Therefore it has been shown by computer simulations [42, 47], that water behaves in the mild supercooled region as a fragile liquid (in accordance with experiments), but also that actually exhibits a Fragile to Strong Crossover (FSC) depending on the pressure or density of the isothermal path followed upon supercooling.

As mentioned in the Section 1.2.1, MCT neglects, in its ideal version, hopping phenomena that restores ergodicity under T_{MCT}. These phenomena cause the deviation, before approaching the T_{MCT} from above, of the structural relaxation time τ_α behavior from the MCT power law or the VFT, in favor to the strong Arrhenius law.

As seen in Figure 1.14, depending on the path water can or not show the FSC. This is because it occurs only if the path followed upon cooling intersects the LLCP Widom line. This coincidence has been demonstrated to hold in several models of water [32, 38, 42, 47], and experimentally it was confirmed in confined water [48, 49].

We recall that the Widom line is defined by the maxima of thermodynamic response functions toward the LLCP. The coincidence of the occurrence of the FSC with the Widom line establishes the non-trivial connection between the dynamics and the thermodynamics of bulk supercooled water.

1.3. Supercooled Water in Biological Systems

Water plays a paramount role in biological systems. Water is in fact essential for life [11]. Water permeates the biophysics at every level, from the water contained in living cells to single water molecules directly bounded to polymer chains, water is also present. Water is indeed the natural ambient of almost all bio-systems. In this Section two case where liquid water at low temperature is important for biological systems, are outlined.

1.3.1. Supercooled Hydration Water Drives the Protein Dynamical Transition

One of the most striking example of the biological role of supercooled water is the low-temperature activation of hydrated proteins.

In fact all the functions of a protein are inhibited if a minimum critical level of hydration is not secured. Without hydration water proteins can not access nor switch between different conformations and therefore fulfill their roles in biological environment. From the dynamical point of view, these importance is embedded in the dynamical coupling between the protein internal motion and its hydration water. Many studies using a variety of techniques have been carried out on biological macromolecules from the stable liquid phase to the supercooled regime aimed

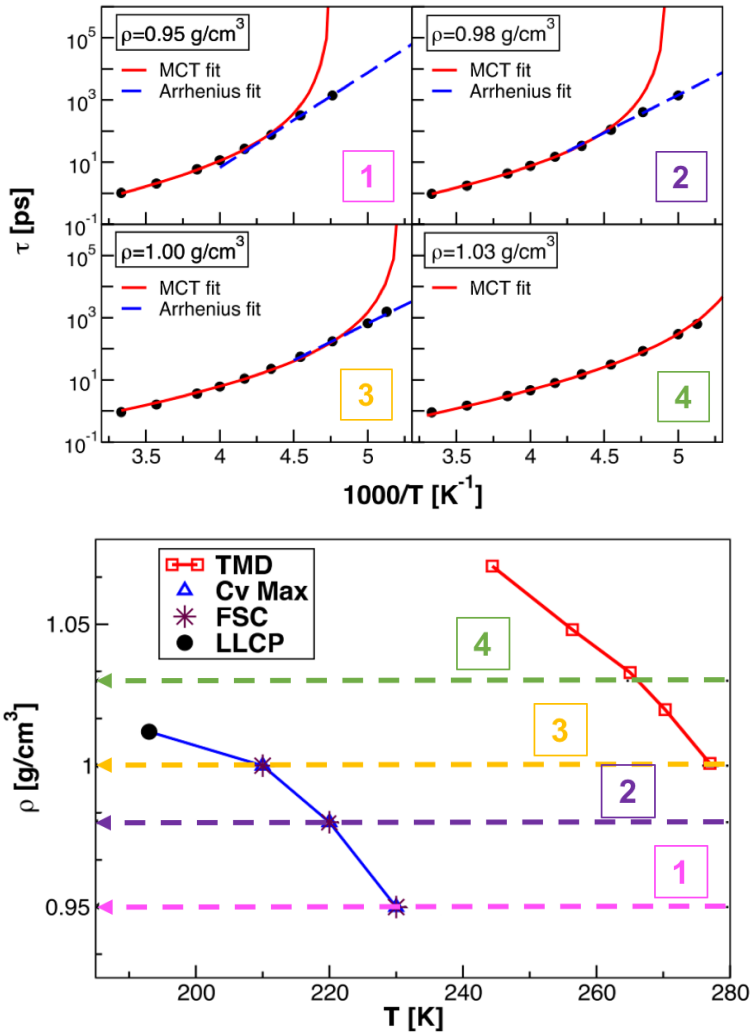

Figure 1.14: Occurrence of FSC in bulk TIP4P/2005 model of water. The Widom line is defined through the c_v maxima connected to the LLCP by the blue line. Figures adapted from Ref. [38].

in the understanding of this coupling [50–52].

In addition to being important for protein stability, and in the energetics and specificity of ligand binding, surface waters also have a profound influence on the dynamics of a protein molecule as a whole.

Assessed the role of hydration water in protein functioning and the connection of this last with protein flexibility, one of the most striking example of the biological role of supercooled hydration water is that the flexibility of a protein, strongly suppressed at very low temperature, suddenly enhances, upon heating, inside the no-man's land of the phase diagram of water. This dynamical feature, that only hydrated proteins undergo, is called Protein Dynamical Transition (PDT) and it is completely driven by the hydration water because dry protein samples do not experience this flexibility increase.

Changes in the flexibility of a protein can be monitored by looking at the temperature dependences of mean square fluctuation of protein structure, i.e. the atomic mean square displacement of protein atoms, $\langle x^2(T)\rangle$. For large macromolecules like proteins, this can be written as a sum of a vibrational component and a conformational component [53]:, thus giving:

$$\langle x^2(T)\rangle = \langle x^2(T)\rangle_v + \langle x^2(T)\rangle_c \tag{1.20}$$

Below the PDT, $\langle x^2(T)\rangle$ is dominated by vibrations, and thus, apart from the zero-point constant value, is linear with the temperature. This is also the normal behavior of $\langle x^2(T)\rangle$ for small organic molecules and harmonic solids [13]. If the protein is hydrated, the behavior of $\langle x^2(T)\rangle$ deviates from this linear behavior and the additional conformation contribution is observed. The onset of this last define the PDT itself. The conformational contribute is due to the activated surface motion of protein domains and gives the extra mobility to hydrated proteins at strictly variance of dry samples. Thus above the PDT, the $\langle x^2(T)\rangle$ results to be dominated by anharmonic collective motion of protein atoms [12]. This phenomenon is shown in Figure 1.15 for protein ribonuclease A, where if the low and high temperature regimes are extrapolated, the PDT can be located near 220 K.

Importantly, in coincidence with the PDT, as detected in this way, biochemical activity of many proteins is restored upon increasing temperature. For instance, enzymes have been observed to rapidly bind substrates or inhibitor above the dynamical transition, probably because without collective motions of protein atoms the enzymes are too "frozen" to accomodate them [12].

This transition has been observed in neutron scattering experiments [54–56], as well as in simulation works [55, 57–60] and terahertz dielectric response experiment [61]. It is found actually not only in proteins, but in a variety of biological macromolecules like RNA, DNA and mem-

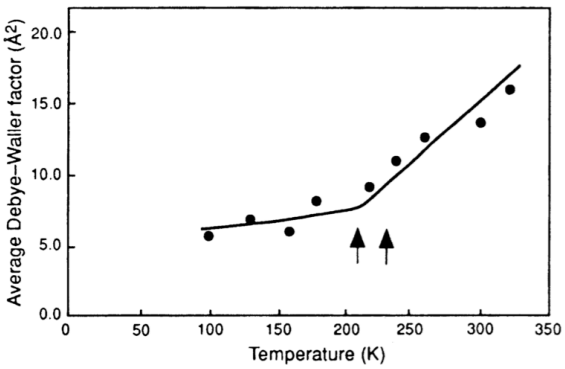

Figure 1.15: Dependence with temperature of the average atomic MSF calculated in the protein ribonuclease A. The transition is broad.

branes [60, 62]. For all these different system, PDT occurs in a universal interval, between 200 K and 240 K. It is therefore in the supercooled region that hydration water most influences the internal dynamics of hydrated biosystems.

1.3.2. The Problem of Cryopreservation

The physics of supercooled water also deals with more practical fields like long term storage and cryopreservation. Cryoprotectors are molecules which can prevent the ice formation and therefore the damage of biomolecules at low temperature.

Disaccharides are in general widely used as excipients because they favors the stabilization in water solution of biological material as proteins and cells [63, 64]. This behavior becomes most valuable to case of stability during freezing and dehydration [65]. Thus today are widely employed in preparing cryoprotectant solutions because of their biocompatibility.

Between sugars, trehalose is today believed to be the more effective for this purpose. Trehalose is a non reducing-sugar formed from two glucose units joined by a 1-1 α-bond. Its structure is shown in Figure 1.16.

Many have been the attempts to explain its effectiveness as cryoprotectant [66–70] especially as in relation to other disaccharides [71–77] in water. Trehalose is able to destroy the water hydrogen-bond network more than other sugars, which should prevent ice-compatible hydrogen bonding networks upon cooling. Trehalose also slow down more consistently the water dynamics.

The cryoprotectant properties of trehalose and other sugars have been also extensively investigated in ternary systems where different proteins are included in sugar-water solutions or glassy matrix [78–82]. Historically three main scenarios have been proposed for explaining the bio-

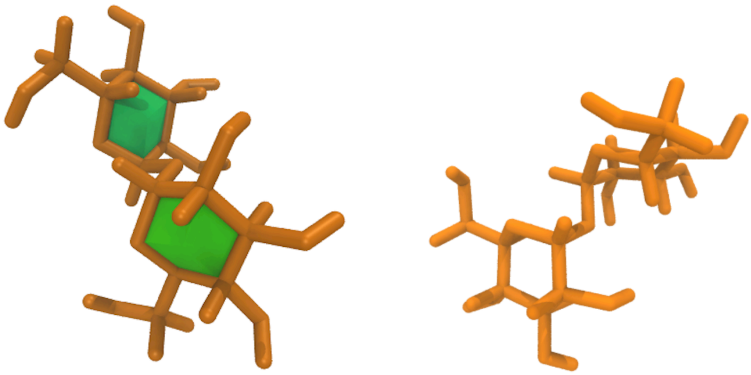

Figure 1.16: Three-dimensional structure of the disaccharide trehalose.

protection mechanism of carbohydrates. Within the *water replacement scenario* by Crowe et al. [83], the source of their bio-preserving power is their ability in establishing strong hydrogen-bond interactions with the polar groups of biomaterials, thus excluding water molecules from the direct interaction with the latter. In the *vitrification scenario* by Green and Angell [84] the mobility of the biomolecule is hindered because of the vitrification of the entire trehalose-water solution upon cooling. According to the *water entrapment scenario* by Belton and Gil [85], trehalose is capable of forming a cage around the protected biostructure, that contains slow water molecules.

Some works point in general to a certain scenario, but in literature results are in general compatible with more than one scenario at the same time, basically because all these hypothesis are not mutually exclusive. This last point motivated the work of Fedorov et al. [86], that with the attempt to include previous findings proposed the fourth hypothesis for explaining bioprotection, the *broken glass scenario* scenario, in which the mobility of the protein is reduced by the formation of trehalose non-uniform cluster interacting with the protein but leaving the protein hydrated.

The role of trehalose in bioprotection along with the crucial controversial points in its current research field has been last year deeply reviewed by Cordone et al. [14].

2

Methods

In this Chapter the methodology used to study water, biological solutions and lithium-chloride water solutions are introduced. All Atom Molecular Dynamics is a computer simulation method for studying the physical evolution of a system. This N-body simulation method is firstly outlined in Section 2.1. Interactions potentials as handled in Molecular Dynamics and the force fields used in the simulations of this work are presented in Section 2.2. Finally, in Section 2.3 observables used to probe the structural and dynamical properties of the simulated systems are described. In this last section, details of the technical methods used for the calculation of observables are also given.

2.1. All Atom Molecular Dynamics Simulation

In Molecular Dynamics (MD), successive configurations of the system are generated by integrating Newton's laws of motion [87]. The result is a set of trajectories that describes how the positions and velocities of the particles in the system vary with time in a deterministic fashion.

In the liquid state the motion is often very difficult to describe analytically due to the coupled nature of the motion of particles. The more realistic models of intermolecular interactions are continuous potentials, where the force on the particle changes whenever the particle changes its position or any other particles interacting with it changes position [88].

A continuous potential was employed in a MD simulation for the first time in 1964, when Rahman [89] used the Lennard Jones potential in the simulation of liquid argon. Rahman together with Stillinger also performed in 1971 the first MD simulations on liquid water [90]. From that time, many important contributions in MD have been done, both from the side of the modeling of interaction potentials that could better reproduce real dynamics of systems, and from the computational methods

side, that much have evolved this techniques also following the progressive increased availability of computing power.

Nowadays MD simulations are widely used by theoretical physicists and chemists working in condensed matter physics and, in particular, in soft matter where often many-body problems cannot be solved analytically. Besides, in the field of supercooled water MD simulations played, as seen in the Introduction, and plays even now a paramount role.

2.1.1. The MD technique

The Hamiltonian of the simulated system which contains a fixed number of particles N is in general given by:

$$H(\mathbf{r}^N, \mathbf{p}^N) = K(\mathbf{p}_1, \mathbf{p}_2, ..., \mathbf{p}_N) + U(\mathbf{r}_1, \mathbf{r}_2, ..., \mathbf{r}_N) = \sum_{i=1}^{N} \frac{p_i^2}{2m} + \sum_{i=1}^{N} \sum_{j>i}^{N} u(\mathbf{r}_i - \mathbf{r}_j) \quad (2.1)$$

where K is kinetic energy and U is the many-body interaction potential. Typically the latter is assumed to be a pairwise potential and in this case, the right equality of Eq. (2.1) holds.

As already said, the trajectory of the particle is obtained by solving the differential equations embodied in Newton's second law:

$$m_i \frac{d^2\mathbf{r}_i}{dt} = \frac{d\mathbf{p}_i}{dt} = \mathbf{F}_i = -\nabla_{\mathbf{r}_i} U \quad (2.2)$$

$$\mathbf{v}_i = \frac{d\mathbf{r}_i}{dt} = \frac{\mathbf{p}_i}{m_i} \quad (2.3)$$

These equations are integrated using a *finite difference method*. This introduces a discretization δt of the temporal axis, and given the positions and the velocities of the particles at time t, the positions and the velocities of the particles at time $t + \delta t$ can be computed. Thus positions and velocities of particles are calculated in a deterministic way. Details about integration algorithms are given in Sec. 2.1.2.

In order to setting up the MD simulation, it is necessary to produce an initial configuration of particles. Suitable initial space configurations are usually assembled by placing the particle at the vertices of standard lattices. In more complex solute-solvent systems, realistic conformations of molecules are taken from crystallographic data. The structure of large macromolecules like proteins and amino-acids can be obtained from the Protein Data Bank, a database where data obtained by X-ray crystallography, NMR spectroscopy, and cryo-electron microscopy, are freely accessible on the Internet via the websites http://www.wwpdb.org/. Nowadays simulation packages like GROMACS [91] include the topology of many common solvents and make available proper tool to add the solvent molecules around a solute. For solute-solvent systems for which it

is not available a proper topology inside the simulation package, the generation of the spatial configuration of molecules is task of the simulator. This is done by creating a box of solvent molecules, placing the solute inside and by discarding those solvent molecules *too* close to the solute.

Velocity configurations are created according to random values. It is common way to generate velocities from the Maxwell-Boltzmann distribution centered at the temperature of interest:

$$p(v_{ix}) = \left(\frac{m_i}{2\pi k_B T}\right)^{1/2} \exp\left[-\frac{1}{2}\frac{m_i v_{xi}^2}{k_B T}\right] \tag{2.4}$$

which provides the probability that at the temperature T, the particle i of mass m_i has a velocity v_{ix} along the $\hat{x}$ axis.

The first stage of the MD simulation is the equilibration of the system which is aimed to reach the equilibrium. Starting from the initial configuration, the system is then allowed to run for periods of time long enough to fully relax. When the simulation involves conformationally flexible macromolecules, as proteins in water, the solvent is allowed to relax first with any counter-ions while the macromolecules is kept fixed. Then the entire system is allowed to relax without any constraint. In the equilibration stage it is typical to monitor the convergence towards a time-independent value of the energy of the system. Once the energy is minimized, all counters are set to zero and the system is allowed to evolve. This last stage is commonly named production run.

MD simulations generate therefore the microscopic evolution of a system, that is positions and velocities. This corresponds to a sequence of points in the phase space as a function of time, these points belong to same ensemble and thus satisfy the conditions of a particular thermodynamic state. Especially to face off experimental data, macroscopic properties as energy or other thermodynamic functions of the system must be evaluated from the information at microscopical level. Therefore a conversion from microscopic to macroscopic properties is to be done. This requires statistical mechanics.

In statistical mechanics, average values are defined as ensemble averages. The ensemble average of the observable of interest $A = A(\mathbf{r}^N, \mathbf{p}^N)$ is given by:

$$\langle A \rangle = \int\int d\mathbf{r}^N d\mathbf{p}^N \; A(\mathbf{r}^N, \mathbf{p}^N)\rho(\mathbf{r}^N, \mathbf{p}^N) \tag{2.5}$$

where integrations are over all possible variables of r and p of the phase space and $\rho(\mathbf{r}^N, \mathbf{p}^N)$ is the probability density of the ensemble. This can be written through the the partition function Z of the ensemble as:

$$\rho(\mathbf{r}^N, \mathbf{p}^N) = \frac{1}{Z} \exp\left[-H(\mathbf{r}^N, \mathbf{p}^N)/(k_B T)\right] \tag{2.6}$$

where H is the Hamiltonian, k_B the Boltzmann constant and T the temperature.

In the MD technique the *ergodic hypothesis* is implied. Then the ensemble average is equal to time average:

$$\langle A \rangle = \langle A \rangle_{time} \tag{2.7}$$

and the ensemble average of the quantity A can be therefore written as:

$$\langle A \rangle = \langle A \rangle_{time} = \lim_{t \to +\infty} \frac{1}{t} \int_0^t A(\mathbf{r}^N, \mathbf{p}^N) dt' \simeq \frac{1}{M} \sum_{t=1}^{M} A(\mathbf{r}^N, \mathbf{p}^N) \tag{2.8}$$

where t is the simulation time, M is the number of time steps in the simulation and $A(\mathbf{r}^N, \mathbf{p}^N)$ is the instantaneous value of A.

The validity of the *ergodic hypothesis* in MD simulations is strictly related to the generation of enough representative conformations of the phase space. If this is the case, the equality (2.7) is satisfied and the significant observables regarding structure, dynamics and thermodynamics can be calculated via Eq. (2.8).

The sampling of *enough* phase space during a MD simulation requires that the simulation time exceeds by far the characteristic time of molecular motion. For this reason the MD simulation of a given state point is divided in two part previously discussed, i.e. the equilibration runs during which trajectories are evolved until the equilibrium is reached (typically with algorithms that rescale velocities), and production runs during which equilibrated trajectories are stored.

There exist different ensembles with different characteristics depending on the thermodynamic state of the collection of configuration. These comprehend:

- The Microcanonical Ensemble (NVE), when the thermodynamic state is characterized by a fixed number of atoms N, a fixed volume V, and a fixed total energy E.
- The Canonical Ensemble (NVT), when the thermodynamic state is characterized by a fixed number of atoms N, a fixed volume V and a fixed temperature, T.
- The Isobaric-Isothermal Ensemble (NPT), when the thermodynamic state is characterized by a fixed number of atoms N, a fixed pressure P and a fixed temperature T.
- The Grand canonical Ensemble (μVT): when the thermodynamic state is characterized by a fixed chemical potential μ, a fixed volume V and a fixed temperature T.

Since in the Microcanonical Ensemble the total energy of the system $E = K + V$ is conserved, this corresponds to the natural ensemble of MD when no rescaling of velocity is performed. There, for example, the temperature of the system is a calculated property. This can be accomplished via the equipartition theorem by:

$$T = \frac{2\langle K \rangle}{(3N - N_c)k_B} \tag{2.9}$$

where N_c is the number of constraints (for example $N_c = 3$ if the the system center of mass motion is removed). The pressure can be calculated using the virial theorem:

$$P = \frac{Nk_BT - \langle \mathcal{V} \rangle}{V} \tag{2.10}$$

where $\mathcal{V} = \frac{1}{3}\sum_{i=1}^{N} \mathbf{r}_i \cdot \mathbf{F}_i$ is the virial.

MD simulations run under the (NPT) and (NVT) constant conditions will be discussed in Subsec. 2.1.3.

Relevant to MD simulations is the suitable treatment of boundaries. Periodic boundary conditions (PBC) are usually applied to calculate bulk gasses, liquids and crystals. This has indeed a twofold importance, because it avoids artifacts due to the boundaries of the finite simulation box (that can act as an external field) and, from the computational point of view, it enables to perform MD simulations with a relatively small number of molecules. Figure 2.1 shows the common form of PBC applied for particle balance in a 2D system. The central simulation box is replicated in all directions to construct image boxes, which give rise to a periodic lattice. Consequently, to each particle leaving the central box always corresponds one of its image entering the box from the opposite side. This preserves the number of particles in box.

2.1.2. MD integration methods

There are many algorithms of *finite difference method* for integrating the equation of motion used in MD simulations. All of these assume that positions velocities and accelerations can be approximated as Taylor series expansions [88]:

$$\begin{aligned}
\mathbf{r}(t + \delta t) &= \mathbf{r}(t) + \mathbf{v}(t)\delta t + \tfrac{1}{2}\mathbf{a}(t)\delta t^2 + \tfrac{1}{6}\mathbf{b}(t)\delta t^3 + \cdots \\
\mathbf{v}(t + \delta t) &= \mathbf{v}(t) + \mathbf{a}(t)\delta t + \tfrac{1}{2}\mathbf{b}(t)\delta t^2 + \cdots \\
\mathbf{a}(t + \delta t) &= \mathbf{a}(t) + \mathbf{b}(t)\delta t + \cdots
\end{aligned} \tag{2.11}$$

The *Verlet algorithm* [92] is frequently used in MD. This algorithm uses the position $\mathbf{r}(t)$ and the acceleration $\mathbf{a}(t)$ at time t and the position at

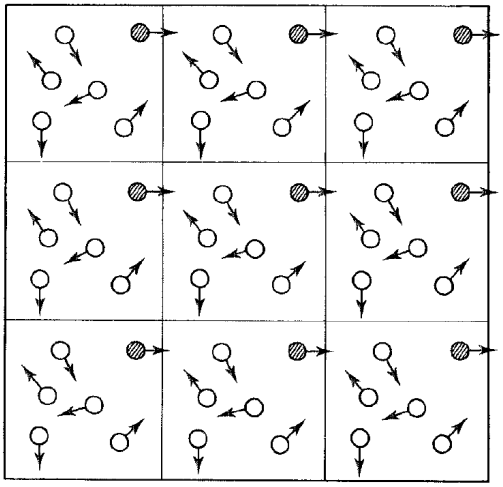

Figure 2.1: Illustration of PBC in MD simulations. Figure from ref [88].

the previous step $\mathbf{r}(t-\delta t)$ to calculate the position at time $t+\delta t$ and the velocity at time t:

$$\begin{aligned}\mathbf{r}(t+\delta t) &= \mathbf{r}(t) + \mathbf{v}(t)\delta t + \tfrac{1}{2}\mathbf{a}(t)\delta t^2 + \cdots \\ \mathbf{r}(t-\delta t) &= \mathbf{r}(t) - \mathbf{v}(t)\delta t + \tfrac{1}{2}\mathbf{a}(t)\delta t^2 - \cdots\end{aligned} \tag{2.12}$$

Adding and subtracting the two equations gives:

$$\begin{aligned}\mathbf{r}(t+\delta t) &= 2\mathbf{r}(t) - \mathbf{r}(t-\delta t) + \mathbf{a}(t)\delta t^2 \\ \mathbf{v}(t) &= \left[\mathbf{r}(t+\delta t) - \mathbf{r}(t-\delta t)\right]/(2\delta t)\end{aligned} \tag{2.13}$$

This algorithm is fast and has some advantages, as for example the modesty of the storage requirements, but it also shows drawbacks: for example the position $\mathbf{r}(t+\delta t)$ is obtained by adding a small term ($\sim \delta t^2$) to the difference of two much larger terms which can lead to a loss of precision. Besides velocities are generated at the same time of the position, but are one time step behind.

Several variants of the Verlet algorithm have been developed which in general enhance the velocity of execution or the precision. One of them is the *leap-frog* algorithm, that makes use of the velocity at half time intervals. This is done in two steps. First, the velocity at time $(t+\frac{1}{2}\delta t)$ is computed from $\mathbf{a}(t)$ and $\mathbf{v}(t-\frac{1}{2}\delta t)$:

$$\mathbf{v}(t+\tfrac{1}{2}\delta t) = \mathbf{v}(t-\tfrac{1}{2}\delta t) + \mathbf{a}(t)\delta t \tag{2.14}$$

then the position at time $(t+\frac{1}{2}\delta t)$ is obtained via:

$$\mathbf{r}(t+\tfrac{1}{2}\delta t) = \mathbf{v}(t) + \mathbf{v}(t+\tfrac{1}{2}\delta t)\delta t \tag{2.15}$$

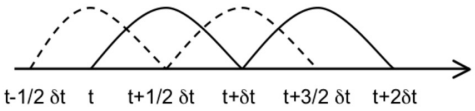

Figure 2.2: A diagram of the leap-frog iteration algorithm. Continuos line indicates the storage of position. Dashed line indicates the storage of velocities. From ref. [88].

This algorithm yields more accurate positions because they are calculated using velocity at a closer time. The velocity at time t can be finally calculated with:

$$\mathbf{v}(t) = \frac{\mathbf{v}(t + \frac{1}{2}\delta t) - \mathbf{v}(t - \frac{1}{2}\delta t)}{2} \tag{2.16}$$

which, again, is not directly generated at the same time of the position, but it is half time step behind. In this algorithm the velocity and the position of a particle are thus stored in such a way they *leapfrog* over each other. This is graphically shown in Figure 2.2.

2.1.3. Constant temperature and constant pressure MD

As seen in Sec. 2.1, the natural ensemble of basic MD is the NVE ensemble. Even in the constant NVE simulation, it is however common to regulate the temperature during the equilibration phase. Besides, sometimes it can be necessary to perform MD simulations under conditions of constant temperature and/or constant pressure, with the purpose, e.g., to mimic real thermodynamic condition of an experiment. Nowadays a variety of thermostats and barostats are actually available to accomplished this need.

The temperature of the system is related to the time average of the kinetic energy by equation (2.9). This prompts to the easiest way to alter the temperature of the system: rescaling the velocities. If the velocities are multiplied by a factor λ at time t, the variation of the temperature in the unconstrained system is given by:

$$\Delta T = \frac{1}{2}\sum_{i=1}^{N}\frac{2}{3}\frac{m_i(\lambda v_i)^2}{Nk_B} - \frac{1}{2}\sum_{i=1}^{N}\frac{2}{3}\frac{m_i v_i^2}{Nk_B} = (\lambda^2 - 1)T(t) \tag{2.17}$$

Thus in order to drive the current temperature of the system $T(t)$ to the desired value T^*, velocities must be multiplied at each time step by a factor λ given by:

$$\lambda = \sqrt{\frac{T^*}{T(t)}} \tag{2.18}$$

An alternative way to control the temperature of the system is to couple it to an external heat bath that fixed the desired temperature by supplying or removing heat from the system. This method, introduced by Berendsen et al. [93] in 1984 gives exponential decay of the temperature of the system towards the desired temperature value. The change in temperature between two successive time step is given by:

$$\frac{dT(t)}{dt} = \frac{1}{\tau}(T_{bath} - T(t)) \qquad \rightarrow \qquad \Delta T = \frac{\delta t}{\tau}(T_{bath} - T(t)) \tag{2.19}$$

where τ is the coupling parameter between the bath and the system and T_{bath} the temperature of the external bath. The velocities are then scaled at each time step by a quantity proportional to the difference of the temperature between the bath and the system:

$$\lambda = \left[1 + \frac{\delta t}{\tau}\left(\frac{T_{bath}}{T(t)} - 1\right)\right]^{1/2} \tag{2.20}$$

Berendsen method does not generate rigorous canonical averages, but they differ from the values of canonical ensemble typically of $\mathcal{O}(1/N)$ [87]. In most cases this accuracy is enough and the Berendsen method is indeed common used in MD simulations.

As it is desired to control the temperature, so it is to control the pressure of the system. A macroscopic system maintains constant pressure by changing its volume. The same can be done during the simulation. Many methods used for controlling the pressure are similar to those used for temperature control. Thus the pressure can be maintained at a constant value by scaling the volume by a factor λ as follows:

$$\mathbf{r}_i' = \lambda^{1/3}\mathbf{r}_i \tag{2.21}$$

In the Berendsen method the system is coupled to a "pressure bath", analogous to the temperature bath, thus the change of pressure can be obtained as follows:

$$\frac{dP(t)}{dt} = \frac{1}{\tau_P}(P_{bath} - P(t)) \qquad \rightarrow \qquad \Delta P = \frac{\delta t}{\tau_P}(P_{bath} - P(t)) \tag{2.22}$$

where τ_P is the coupling pressure constant, P_{bath} the pressure of the bath and $P(t)$ the instantaneous value of the pressure in the system. Volume is then rescaled by:

$$\lambda = 1 - \kappa_T \frac{\delta t}{\tau_P}(P - P_{bath}) \tag{2.23}$$

where κ_T is the isothermal compressibility describing the change of volume as response to the pressure.

$$\kappa = -\frac{1}{V}\left(\frac{\partial V}{\partial P}\right)_T \tag{2.24}$$

2.2. MD Forcefields

Potential energy terms can be split in the two term relative to the intramolecular interactions (bonded interactions) and the intermolecular interactions (non-bonded interactions):

$$\mathcal{U} = \mathcal{U}_{bonded} + \mathcal{U}_{non-bonded} \tag{2.25}$$

The general form of the intramolecular part is:

$$\mathcal{U}_{bonded} = \mathcal{U}_{stretch} + \mathcal{U}_{bend} + \mathcal{U}_{torsion} \tag{2.26}$$

where $\mathcal{U}_{stretch}$ describes oscillations about the equilibrium bond length, $\mathcal{U}_{bend}$ describes oscillations of three atoms about an equilibrium bond angle, and $\mathcal{U}_{torsion}$ describes the torsional rotation of four atoms about a central bond. Rigid potential, like the SPC/E or the TIP4P, constrain the internal motions of particles.

The intermolecular part of the potential is typically written as:

$$\mathcal{U}_{non-bonded} = \mathcal{U}_{LJ} + \mathcal{U}_{Coulomb} \tag{2.27}$$

where $\mathcal{U}_{LJ}$ is the Lennard-Jones (LJ) potential:

$$\mathcal{U}_{LJ} = 4\epsilon\left[\left(\frac{\sigma}{r}\right)^{12} - \left(\frac{\sigma}{r}\right)^{6}\right] \tag{2.28}$$

and $\mathcal{U}_{Coulomb}$ is the electrostatic potential:

$$\mathcal{U}_{Coulomb} = \frac{q_i q_j}{r} \tag{2.29}$$

The most consuming part of the MD simulation is the calculation of non-bonded interactions, which, in the most cases have a pairwise form. Typically, non-bonded interaction are handled with a *non-bonded cutoff* and with the *minimum image convention*. According to this convention each particle in the simulation box interacts only with the closest image of the remaining particles in the system. When the non-bonded cutoff is employed, the interaction between pairs at distance major than the cutoff value are set to zero and are therefore calculated only for distance $r_{ij} = |\mathbf{r}_i - \mathbf{r}_j| \leq r_{cut} < L/2$, where L is the linear dimension of the box and the upper limit is introduced to avoid considering the same particle twice due to the PBC. The choice of the non-bonded cutoff is more critical when PBC are set in systems which contain large macromolecules. This is shown in Figure 2.3, where the linear dimension of the cubic box must be large enough to avoid interactions of the solute with itself.

With the introduction of the cut-off scheme for non-bonded interactions, corrections must be in general introduced in the interaction potentials [87]. For short range potential, as the Lennard-Jones potential, corrections are typically performed in the real space. For long range potential, as the electrostatic interactions, corrections are often handled in the Fourier space with the Particle Mesh Ewald method (PME).

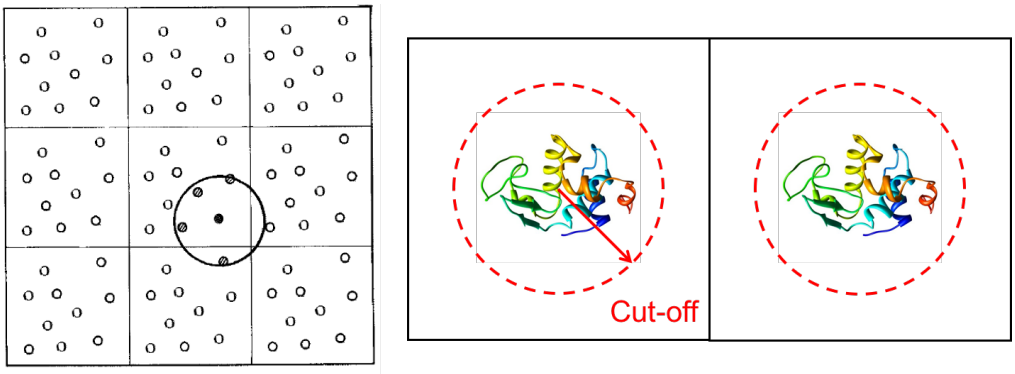

Figure 2.3: Illustration of PBC and *minimum image convention* in MD simulations. Adapted from Ref. [88].

2.2.1. The SPC/E model of water

Berendsen et al. [94] developed the *simple point charge extended* (SPC/E) model of water in 1987. This potential consists of an improvement of the existing SPC (*simple point charge*) [95] model with the inclusion of a polarization correction to the energy and the consequent reparametrization of the SPC model. This was aimed to best reproduce properties of polar liquids.

The SPC/E tetrahedral water molecule is shown in Figure 2.4(a). The three interaction sites are coplanar, the OH distance is 1 Å and the H-O-H angle is 109.5°. Point charges lie on the oxygen position with $q_O = -0.8476e$ and on the hydrogen positions with $q_H = +0.4238e$. On the oxygen position also lies the only Lennard-Jones interaction site of the molecule with $\epsilon_{OO} = 0.650$ kJ/mol and $\sigma_{OO} = 3.166$ Å.

The complete interaction potential of the i-th water molecule can thus be written as:

$$u(r_{ij}) = 4\epsilon_{ij}\left[\left(\frac{\sigma_{ij}}{r_i - r_j}\right)^{12} - \left(\frac{\sigma_{ij}}{r_i - r_j}\right)^{6}\right] + \frac{e^2}{4\pi\epsilon_0}\frac{q_i q_j}{|r_i - r_j|}. \tag{2.30}$$

2.2.2. The TIP4P/2005 model of water

The TIP4P-*series* consist of several potentials of water sharing the same water molecule geometry and differing in the parametrization. They comprehend the TIP4P [96] firstly developed in 1985, the re-parametrization TIP4P-Ice [97] aimed to better reproduce those regions of the phase diagram of water competing to the different solid phases of crystallin and amourphous water and the two re-parametrizations TIP4P/Ew [98] and TIP4P/2005 [99] that yield successive improvement exemplified by the TMD, diffusion coefficient etc. in water. Today TIP4P/2005 behaves the best between rigid potential model of water [100].

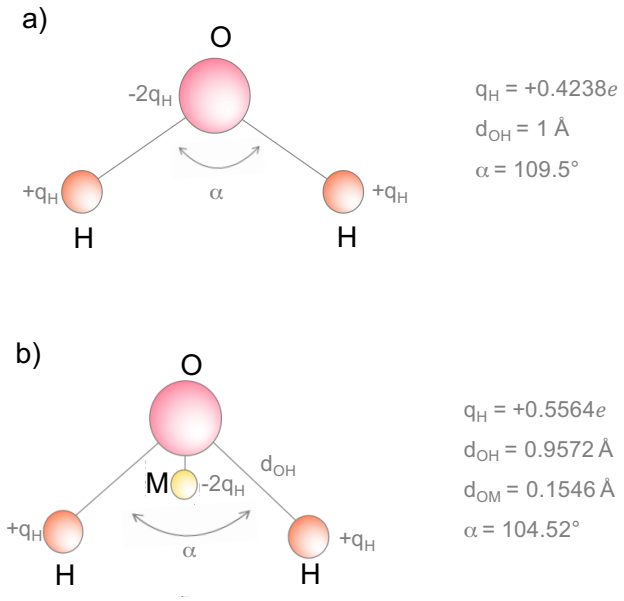

Figure 2.4: Geometry of SPC/E (a) and TIP4P/2005 (b) models of water.

The geometry of the water molecule described by any TIP4P-X model is shown in Figure (b). The water molecule is represented by four interaction sites. On both the hydrogen atoms lyes a charge site q_H. The oxygen atom is the LJ interaction site of the molecule and it is spatially separated from the charge point that described its electrostatic interaction. A negative charge site M with $q_M = -2q_H$ is thus placed along the bisector of the H-O-H angle and coplanar with the other three interaction sites.

In TIP4P/2005 the OH distance and the the H-O-H angle are fixed to the experimental values, 0.9572 Å and 104.52°, respectively. The O-M distance is 0.1546 Å. LJ interaction parameters are $\epsilon_{OO} = 0.7749$ kJ/mol and $\sigma_{OO} = 3.1589$ Å. The charge q_H is equal to $+0.5564e$.

2.2.3. The JC-TIP4P/2005 potential of LiCl-water solutions

The JC-TIP4P/2005 potential [101] describes the interaction potential between particles in LiCl-water solutions.

In this forcefield on each ion position is placed a LJ site and a point charged site. Ions LJ parameters are those from Joung and Cheatham [102] and electrostatic charges are $+e$ for the Li^+ ion and $-e$ for the Cl^- ion. The LJ interaction parameters and charge sites of water are those of the TIP4P/2005.

The potential of the ionic solution is written then as a combination of

a LJ and a Coulombic electrostatic potential in the form:

$$u(r_{ij}) = 4\epsilon_{ij}\left[\left(\frac{\sigma_{ij}}{r_{ij}}\right)^{12} - \left(\frac{\sigma_{ij}}{r_{ij}}\right)^{6}\right] + \frac{q_i q_j}{4\pi\epsilon_0 r_{ij}} \tag{2.31}$$

where r_{ij} is the distance between two interacting particles and q_i is either the charge of an ion or the charge of a water site.

Within JC-TIP4P/2005 potential, the crossed interactions are obtained with modified Lorentz-Berthelot combining rules:

$$\epsilon_{ij} = \chi \cdot \sqrt{\epsilon_{ii} \cdot \epsilon_{jj}}\,; \qquad \sigma_{ij} = \eta \cdot \frac{\sigma_{ii} + \sigma_{ij}}{2} \tag{2.32}$$

with $\chi = 1.88$ and $\eta = 0.934$ [101], against the $\chi = 1$ and $\eta = 1$ value of LB rule, that corrects the ion pairing structure.

The JC-TIP4P/2005 ion-water and ion-ion parameters for the LJ form of the potential used in this work are reported in Table 2.1.

Table 2.1: Ion-water and ion-ion LJ interaction parameters in JC-TIP4P/2005 potential [101].

Atom pair	ϵ_{ij} (kJ/mol)	σ_{ij} (Å)
O - O	0.77490	3.1589
Li^+ - Li^+	0.43509	1.4397
Cl^- - Cl^-	0.04879	4.9178
Li^+ - O	0.58065	2.2993
Li^+ - Cl^-	0.27392	2.9626
Cl^- - O	0.19444	4.0383

2.2.4. The CHARMM FF for proteins and disaccharides

CHARMM (*Chemistry at Harvard Macromolecular Mechanics*) is a set of force fields widely used for molecular dynamics of protein [103, 104], nucleic acids [105, 106], lipids [107], saccharides [108, 109] and other biochemical compounds and ions, freely accessible from the Internet at the website `http://mackerell.umaryland.edu/charmm_ff.shtml`.

Interaction potentials of CHARMM are divided in two contribution: (i) interactions between chemically bonded nearest neighbors and (ii) interactions beyond the chemically bonded neighbors. The first group consists of the bonded energy terms that describe bond stretching, angle bending, dihedral and improper dihedral energy. The second group consists of the non-bonded energy terms described by Lennard-Jones and Coulomb potentials.

The complete interaction potential of the latest CHARMM force fields has the following form:

$$\mathcal{U} = \mathcal{U}_{bonded} + \mathcal{U}_{nonbonded} \tag{2.33}$$

where $\mathcal{U}_{bonded}$ consists of the terms:

$$\mathcal{U}_{bonded} = \mathcal{U}_{bond} + \mathcal{U}_{angle} + \mathcal{U}_{UB} + \mathcal{U}_{dihedral} + \mathcal{U}_{improper} + \mathcal{U}_{CMAP} \tag{2.34}$$

where:

$$\begin{aligned}
\mathcal{U}_{bond} &= \sum_{bonds} K_b(b - b^0)^2, \\
\mathcal{U}_{angle} &= \sum_{angles} K_\theta(\theta - \theta^0)^2, \\
\mathcal{U}_{UB} &= \sum_{Urey-Bradley} K_{UB}(b^{1-3} - b^{1-3,0})^2, \\
\mathcal{U}_{dihedral} &= \sum_{dihedrals} K_\phi((1 + cos(n\phi - \delta)), \\
\mathcal{U}_{improper} &= \sum_{impropers} K_\omega(\omega - \omega^0)^2, \\
\mathcal{U}_{CMAP} &= \sum_{residues} u_{CMAP}(\phi, \psi)
\end{aligned} \tag{2.35}$$

and $\mathcal{U}_{nonbonded}$ of the two terms:

$$\mathcal{U}_{nonbonded} = \mathcal{U}_{LJ} + \mathcal{U}_{Coul} \tag{2.36}$$

where:

$$\begin{aligned}
\mathcal{U}_{LJ} &= \sum_{non-bond.pairs} \epsilon_{ij} \left[\left(\frac{\sigma_{ij}}{r_{ij}} \right)^{12} - 2 \left(\frac{\sigma_{ij}}{r_{ij}} \right)^{6} \right] \\
\mathcal{U}_{Coul} &= \sum_{non-bond.pairs} \frac{q_i q_j}{\epsilon_0 r_{ij}}
\end{aligned} \tag{2.37}$$

CHARMM includes the values of naught terms (e.g. b^0 in $\mathcal{U}_{bond}$), force constants (K_i), other parameters (e.g. n, δ), the partial charges q_i and the LJ parameters (ϵ_{ij} and σ_{ij}). Cross interaction parameters are obtained with the Lorentz-Berthelot combining rules.

For comparison with equation (2.26), CHARMM introduces two terms, $\mathcal{U}_{UB}$ and $\mathcal{U}_{CMAP}$, that merit explanation. The Urey-Bradley term, $\mathcal{U}_{UB}$, is a harmonic term in the distance between atoms 1 and 3 that forms an angle

θ. The term has been introduced for improvement of in-plane deformations and vibrational spectra by separating symmetric and asymmetric bond stretching modes [103]. The CMAP term [104] is a cross-term for the backbone dihedral angles ϕ and ψ realized by grid based energy correction maps. This is applied in CHARMM forcefield to improve dihedral angles of only protein backbones.

2.3. MD Observables

This section gives the definition of observables which are used in this study and that can be calculated directly from the MD trajectories.

Generally speaking, observables in MD are divided between the ones probing the structure and the ones probing the dynamics of the simulated system. Conceptually they differ in the methods of evaluation. If the quantity A is static, function of the N instantaneous positions and/or velocities of the system, the mean value of A is calculated at each configuration i and then averaged over the N stored configurations:

$$\langle A \rangle = \frac{1}{N} \sum_{i=0}^{N} A_i(\mathbf{r}^N, \mathbf{p}^N) \tag{2.38}$$

If the quantity A is dynamical, i.e. it is a time-dependent properties of the system, firstly the trajectories must be expanded by removing the PBC, then the instantaneous mean value of A at time step t is obtained by averaging the value of A over all possible initial time:

$$\langle A(t) \rangle = \frac{1}{NM} \sum_{t_1} \sum_{t_2 - t_1 = t} A(t_1 - t_2) \tag{2.39}$$

2.3.1. Dynamical quantities

Self Intermediate Scattering Function

The SISF is defined as the spatial Fourier-transform of the self part of van Hove function, $G_s(\mathbf{r}, t)$:

$$F_s(\mathbf{q}, t) \equiv \int G_s(\mathbf{r}, t) \exp(-i\mathbf{q} \cdot \mathbf{r}) d\mathbf{r} \tag{2.40}$$

It can be shown that the SISF is the autocorrelation function of the Fourier components of the local density $\rho(\mathbf{r}, t)$:

$$F_s(\mathbf{q}, t) = \frac{1}{N} \langle \rho_{\mathbf{q}}(t) \rho_{-\mathbf{q}} \rangle = \langle \frac{1}{N} \sum_{i=1}^{N} e^{i\mathbf{q} \cdot (\mathbf{r}_i(t) - \mathbf{r}_i(0))} \rangle \tag{2.41}$$

Equation (2.41) can be directly computed from the atomic trajectories and it is therefore preferred from the computational point of view to the Fourier transform formulation of Eq. (2.40).

The SISF probes the single-particle translational dynamics of the system and characterizes its structural relaxation phenomena. This function can be directly compared to experiments from inelastic neutron or X-ray scattering.

I wrote a portable C code to calculate this quantity using the Message Passing Interface (MPI) paradigma, which enables the execution of the program on parallel computing architectures. In this work much computational time, often longer than the simulation time itself, is dedicated to the calculations of time-dependent correlators. The working flow for calculating time correlators and the MPI parallelization scheme are outlined in the dedicated Subsection 2.3.3.

Mean Squared Displacement

The Mean Squared Displacement (MSD) is defined as:

$$\langle \Delta r^2(t) \rangle = \langle \frac{1}{N} \sum_{i=1}^{N} [r_i(t) - r_i(0)]^2 \rangle \tag{2.42}$$

where N is the number of particles analyzed and $r_i(t)$ the particle position at time t.

Experimental methods to determine MSDs include neutron scattering and photon correlation spectroscopy.

I wrote a MPI-C code to calculate this quantity.

2.3.2. Structural quantities

Radial Distribution Function

The Radial Distribution Function (RDF) or *pair correlation function* $g(r)$ gives the probability of finding a pair of atoms (or molecules) at distance r, relative to the probability expected for a completely random distribution at the same density. Basically RDF says whether or not two particles are likely to be found with a separation distance of r.

Its definition takes an ensemble average over pairs [110]:

$$g(r) = \frac{V}{N^2} \langle \sum_i \sum_{j \neq i} \delta \left(r - r_{ij} \right) \rangle \tag{2.43}$$

where N is the particle number and V the volume of the system. The definition (2.43) is typically used in the evaluation of $g(r)$ by computer simulation where in practice the delta function is replaced by a histogram compiled with all pair spatial separations. The histogram is then normalized by the average number of atoms in the same interval in an ideal gas at the same density $\rho = N/V$.

The calculation is performed through a GROMACS tool.

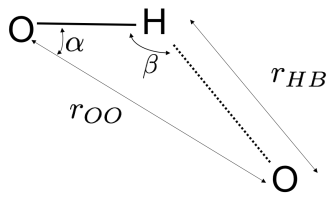

Figure 2.5: Geometry of the O−H group of the donor water molecule and the O atom of the acceptor water molecule involved in a Hydrogen Bond, for the definition of HB adopted in this work.

Trehalose number density profiles around the protein

The number density profile of trehalose molecule is obtained dividing the number of trehalose molecules found between r and $r + \Delta r$ from the center of geometry of the protein by the volume of the corresponding spherical shell $4\pi \left[(r + \Delta r)^3 - r^3\right]/3$ with $\Delta r = 0.02$ Å.

Number density profile is also obtained dividing the number of trehalose molecules found between r and $r + \Delta r$ from the closest atom of the protein, by the total number of trehalose molecules in the solution.

I wrote serial C-codes to perform these calculations.

Water Hydrogen Bonds

A Hydrogen Bond between a donor and an acceptor can be defined with different criterions regarding or the geometry or the energetics. In this work a geometrical criterion is used to define whether a hydrogen bond between two water molecules exists.

A commonly used geometrical criterion is the following. A donor oxygen atom and an acceptor oxygen atom are hydrogen bonded if (i) the distance between them, r_{OO} , is less than a cutoff distance and if (ii) the acceptor-donor-hydrogen angle, $\alpha = \mathrm{H} - \hat{\mathrm{O}} \cdots \mathrm{O}$, is less than or equal to a cutoff angle. This condition is shown in Figure 2.5. Typically the first minimum of the radial distribution function between the donor and the acceptor is used as the cutoff distance. The cutoff angle is chosen to guarantee the linearity of the HB bond inside a certain cone value.

HB between water molecules are defined in this work by the conditions used in Ref. [111], these are:

$$\begin{aligned} r_{OO} &< 3.5 \text{ Å} \\ \alpha &< 30^\circ \end{aligned} \tag{2.44}$$

The conditions of Eq. 2.44 hold to $r_{HB} < 2.7$ Å and $\beta > 140^\circ$.

I wrote a C code to count water hydrogen bonds in a bulk system. With this code the following system properties are calculated:

- mean number of hydrogen bonds of the system.

- frequency distribution of the angle between the oxygens of three nearest neighbor water molecules,
- frequency distribution of the hydrogen bond length in water,
- frequency distribution of number of hydrogen bonds per molecule as donor,
- frequency distribution of number of hydrogen bonds per molecule as acceptor,
- frequency distribution of total number of hydrogen bonds per molecule,

I adapted the code to perform a layer analysis of water hydrogen bonds around the protein. The differences between the bulk and the shell version of this program are:

- analyzed water molecules must satisfied the criterion $r_{shell,in} < r_{OO} < r_{shell,out}$ where r_{OO} is the position of the water oxygen atom and $r_{shell,out} - r_{shell,in}$ is the thickness of the hydration shell layer, calculated from the closest protein atom.
- to enhance the velocity of the code, since ~ 14000 water molecules are in the simulation box, I implemented the code using lists of nearest neighbor water molecules in every shell. The search of nearest neighbor molecules inside a given shell is extended only from the closest shells to the considered one.
- the normalization of frequency distributions at each configuration t is the number of water molecules found in the hydration shell at t.

2.3.3. Calculation of time autocorrelation functions

In general, an autocorrelation function $c_{aa}(t)$ of quantity a that is assumed by the i-th particle, $a_i(t)$, has the following form:

$$c_{aa}(t) = \frac{1}{N}\sum_{i=1}^{N}\frac{\langle a_i(t)a_i(0)\rangle}{\langle a_i(0)a_i(0)\rangle} \tag{2.45}$$

where the averaging over N atoms is performed and the normalization is chosen so that $c_{aa}(0) = 1$.

The first step for the calculation of any correlation function is to expand trajectories in time, by removing the PBC, so that values $a_i(t)$ can be evaluated at correct positions. If the duration of the simulation is significantly longer than the relaxation time, then many time differences t can be evaluated from the simulation to calculate the correlation function, in such a way the uncertainty in the calculation is reduced.

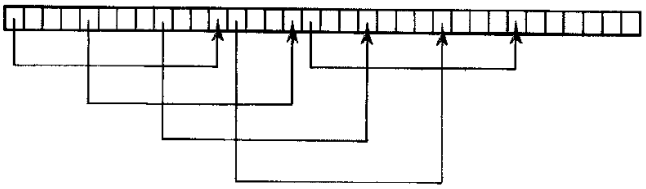

Figure 2.6: The use of different time origins improves the accuracy of the evaluation of time correlation functions. Figure from Ref. [88].

If the simulation has been run for a total of Q steps, each interme-diated stored steps can be used to calculate the correlator. To improve the accuracy of the calculation of the correlator at a particular time step P, it is common to use time origins that are separated by P step. This is shown in Figure 2.6. The first value of $c_{aa}(P)$ would be evaluated at steps 1 and P, the second at steps 2 and $P+1$ and so on. If we use M time origins t_m, then the autocorrelation function is given by:

$$c_{aa}(t) = \frac{1}{MN} \sum_{m=1}^{N} \sum_{i=1}^{N} \frac{\langle a_i(t_m + t) a_i(t_m) \rangle}{\langle a_i(t_m) a_i(t_m) \rangle} \tag{2.46}$$

For very long simulation, the calculation in Eq. (2.46) it took relatively long time in respect to the MD time, even if the system does not contain many particles.

I give an example on a small system I have worked on. Let's consider a simulation of LiCl:6H_2O solution performed at $T = 280$ K. We evolved the system for three millions steps of 1 fs. The box contains 480 water molecules, 80 Cl^- and 80 Li^+ ions. The simulation took about 3.5 hours on a 4 core machine. The correlation of 269 513 different times for all the atoms, it took about 1 day, which is of course reasonable. Typical production runs are although evolved for much longer times, especially at low temperature, so that to calculate SISFs can take weeks.

Besides for other system, like a protein immersed in water (~ 14 000 water molecules), correlators can be evaluated also in a certain region of space of the system, like in the hydration shell of the protein. In this case, where the serial-code program must also perform time exclusion of particle that don't respect the constraint to be in the shell, the calculation of the SISF takes extremely long time on a single compute core.

Part of my initial work was thus dedicated to the parallelization of the analysis code through the MPI paradigma [112].

This results in a very good speed-up of the calculations. For sake of comparison, to self-correlate 31 745 time positions stored at $T = 300$ K for the protein+water system, and to perform the calculation of the SISF averaged on only 3 000 water oxygen atoms of the system, it took 171

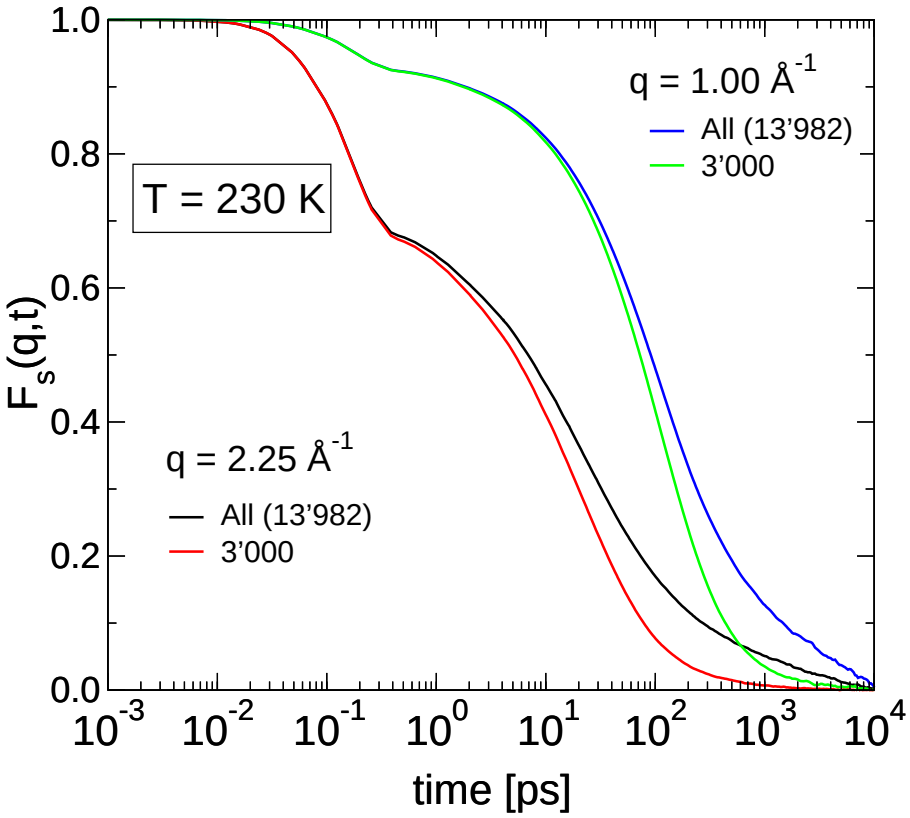

Figure 2.7: Oxygen Self Intermediate Scattering Function of the hydration shell of the lysozyme. The number of total water oxygen atoms of the simulation is 13 982. Note the lost of accuracy above 1 ps when the calculation is not performed over all the particle of the system.

hours ~ 7 days on a single core machine. With the MPI implementation that i wrote on the serial C-code, the same calculation is performed in 40 minutes on a 20 core compute node of our cluster.

The MPI version of the analysis code much increases the accuracy of the calculation of both oxygen SISFs and MSDs. In fact it has opened the possibility to select and analyzed all the oxygen water atom of the system and thus to perform these calculations with a much higher precision. In Figure 2.7 it is shown how important it is playing averages over more molecules, especially when it is of interest the extraction on reliable relaxation times from the SISF.

3

Translational Relaxations of Protein Hydration Water

In this Chapter results on the single particle translational dynamics of water at the surface of the globular protein lysozyme are presented. This Molecular Dynamics simulation was focused to the characterization of the Self Intermediate Scattering Function (SISF) of hydration water along the 1 bar isobar upon supercooling. The discussion of the results is done through a comparative study between the lysozyme hydration water and bulk water.

In Sec. 3.2, the systems and the simulation details are described. In Sec. 3.3 results on the density-density correlation functions and the relaxation times of water are presented and discussed. Sec. 3.4 is devoted to conclusions.

3.1. Introduction

Water near biological surfaces is perturbed with respect to its bulk phase both in the structure and in the dynamics [113–118].

Depolarized light scattering experiments [116, 119, 120] detected two distinct relaxations when measuring spectra of aqueous solutions of biomolecules. The first one is a bulk-like relaxation while the second one is 6-8 time slower than the first one and this second relaxation was specifically ascribed to hydration water. Simulations on aqueous solutions of water and biomolecules upon cooling [76, 121] have also detected these two kinds of relaxations with the same retardation factor. The correlators analyzed in these studies were total correlators where a part of the contribution to their shape comes from hydration water and the other part comes from the bulk-like water contained in the solution. Femtosecond resolved fluorescence experiments [122, 123] explicitly showed that at

ambient temperature, there are two relaxation times coming from the solvation shell. By using biological probes, it has also been found that at ambient temperature, the solvation process always occurs through two relaxations which can differ up to one order of magnitude [50]. The slower relaxation appears due to the coupling with the protein motions [50–52].

Therefore several experiments show that hydration water appears not only slowed down by its interaction with the biosurface but also "bimodal" in the dynamics.

In a seminal paper, Chen et al. [54] studied the single particle translational dynamics of a monolayer coverage of water close to lysozyme by quasielastic neutron scattering upon cooling. They found a single slow structural relaxation time upon cooling for low Q exchanged wavevectors, up to Q = 1.1 $Å^{-1}$, and found that this relaxation is the analogous of the α-relaxation of bulk water, the relaxation typical of glass formers. This relaxation shows a fragile to strong transition close to the Protein Dynamical Transition (PDT). These findings were confirmed by further experiments and simulations and further studies on the diffusion coefficient [55, 59, 60].

The considerable effort done by the community in this field lead to substantial progresses in the understanding of hydration water slow translational dynamics, nonetheless the picture is still not complete mainly because of the fact that experiments and simulations often access only to a part or to an average of the complete microscopic picture that we would ideally like to have.

In this work, as already mentioned, we study an aqueous solution of the globular protein lysozyme. The lysozyme is an antimicrobial enzyme consisting of 129 amino acid residues having a molecular weight of 14.4 kDa. It folds into a compact globular structure having an ellipsoidal shape with dimensions $a \times c \times c = 2.25 \times 1.3 \times 1.3$ nm. The active site of lysozyme consists of a deep crevice, which divides the protein into two domains linked by an alpha helix. One domain consists almost entirely of beta-sheet structures, while the second domain is predominantly alpha-helical [124]. A lysozyme is shown in Figure 3.1.

3.2. Systems & Simulation Details

MD all-atoms simulations have been carried out on the lysozyme globular protein immersed in water. The system is composed of 1 lysozyme protein, 13982 water molecules, and 8 Cl^- counterions to maintain electric neutrality of the system.

Protein bonded and non-bonded interactions were modeled by the CHARMM force field [103, 104] and water was modeled by the SPC/E potential [94]. Both forcefields have been presented in Section 2.2. The cutoff radius for the non-bonded van der Waals interactions was set to

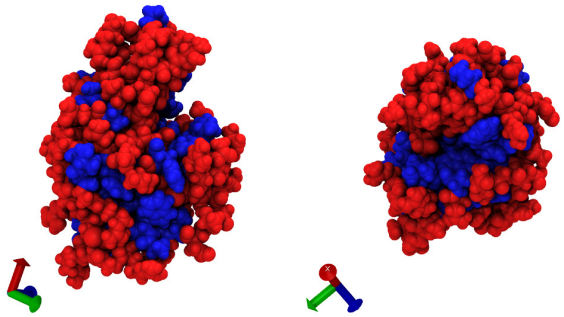

Figure 3.1: Lysozyme in the VDW representation, colored according to the hydrophobicity of its residues.

10 Å. Particle Mesh Ewald (PME) method was used to handle the electrostatic interactions. Verlet leap-frog algorithm, with a time step of 1 fs, was used to integrate the equations of motion. GROMACS 4.5.5 [91, 125] package was employed to perform MD simulation. Simulations were conducted on the INFN-Grid Roma Tre cluster.

The system have been simulated at constant pressure $p = 1$ bar and at ten different temperatures spanning the interval (300-200) K. Both temperature and pressure were handled with the Berendsen method [93].

The length of the equilibration runs depends on the temperature of the system. It ranges from a minimum of 30 ns at high temperature to a maximum of 100 ns at low temperature. At each temperature, the equilibration run was followed by the production run of 20 ns (high temperature) or 30 ns (low temperature) used for the calculation of the Self Intermediate Scattering Functions. In Table 3.1 the details of all the simulated thermodynamic points are shown.

A reference system composed of 500 SPC/E water molecules has been also simulated at the same pressure of the water and lysozyme system, $p = 1$ bar, and for the same temperatures plus T = 195 K. The non-bonded interactions have a cutoff distance of 10 Å. Coulomb interactions have been implemented with the PME method. Details on the simulated state points are reported in same Table 3.1. Bulk results presented in this work are referring to this system.

The total computational time amounts to about 1575 ns for the two simulated isobars of the two systems. The simulations were carried out on the INFN-Grid Roma Tre cluster[1] where we achieved an average simulation times of 8 ns/day for the protein+water system on 32-core compute nodes and 90 ns/day for the bulk water systems on 12-core compute nodes. The total computational time required on a single cpu for this

[1] http://web-cluster.fis.uniroma3.it/

simulations would be ~ 5 years.

Table 3.1: Summary of simulated state points. Details shown are the temperature and the density of the systems. For each temperature the equilibration run of length t_{eq} is followed by production runs t_{prod}.

System	T (K)	ρ (kg/m^3)	t_{eq} (ns)	$t_{prod,1}$(ns)	$t_{prod,2}$ (ns)
Lyso(Aq)	300	1014.38	10	20	20
	280	1023.28	10	20	20
	260	1029.12	10	20	20
	250	1030.28	30	20	10
	240	1030.22	30	20	10
	230	1028.63	30	20	10
	220	1025.16	30	20	10
	210	1019.97	30	20	10
	205	1016.88	30	30	10
	200	1013.33	60	30	10
bulk water	300	998.68	20	20	10
	280	1007.59	20	20	10
	260	1012.87	20	20	10
	250	1013.79	20	20	10
	240	1012.61	20	20	10
	230	1010.60	25	20	10
	220	1006.02	30	20	10
	210	1000.25	60	20	10
	205	996.95	60	30	20
	200	991.70	90	30	20
	195	991.48	100	30	20

This Chapter focuses on the dynamical characterization of the protein hydration water, namely, water molecules at the protein interface. Typically hydration water can be defined in a shell of 4-6 Å [76, 113, 114, 121] around macromolecules. In this work, hydration water of lysozyme refers to water molecules at a distance minor or equal to 6 Å from any lysozyme atoms. Therefore in our study the protein is regarded as a whole as well as the hydration water surrounding it.

In Figure 3.2, we show a 20 Å slice cut projected in two dimensions of our system. Hydration water defined by the above criterion is highlighted in Figure 3.3.

To have an idea on *which* kind of water we are seeing, in figure 3.4 are shown two significant pair radial distribution functions calculated between an atom of the protein and the oxygen atom of a water molecule.

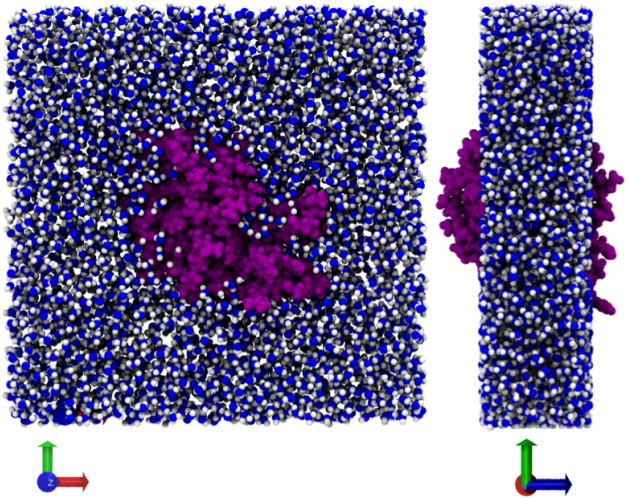

Figure 3.2: Snapshot of the simulated lysozyme in water at $T = 300$ K. The image corresponds to a 20 Å slice in the z direction projected into the xy plane of the 75 Å $\times$ 75 Å $\times$ 75 Å simulation box.

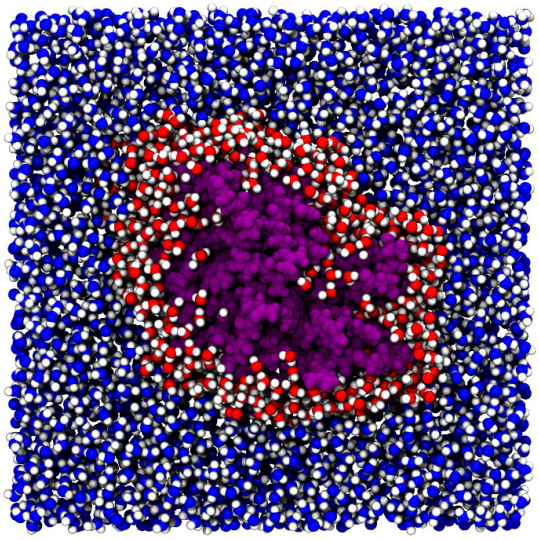

Figure 3.3: Snapshot of the simulated lysozyme in water at $T = 300$ K. The lysozyme is depicted as purple spheres. Water molecules are colored according to their distance from the lysozyme: red (oxygens) and white (hydrogens) molecules correspond to hydration water, namely water molecules within a distance up to 6 Å from the protein atoms. The rest of the water molecules are shown in blue (oxygens) and white (hydrogens).

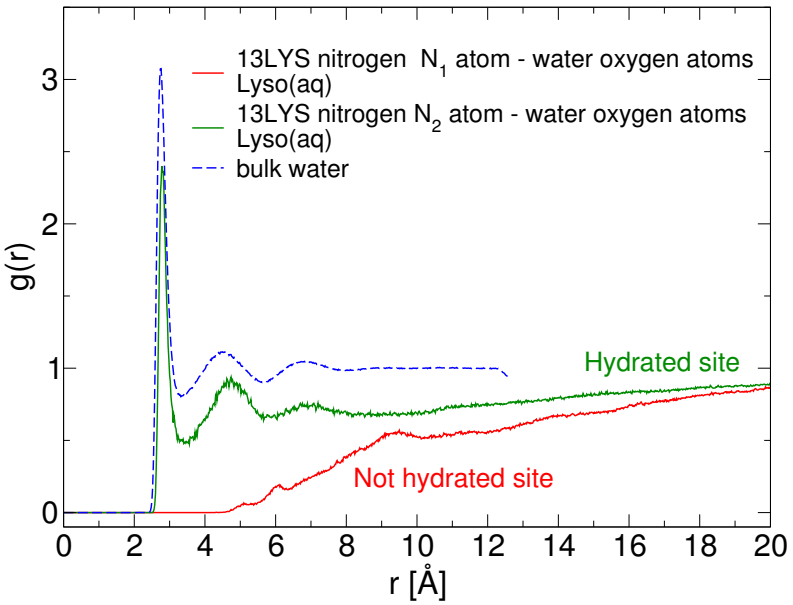

Figure 3.4: Pair correlation function between the nitrogen atom N1 (orange) or N2 (green) of 13LYS of lysozyme atom and the water oxygen. Radial distribution function of water is also reported (dashed line). Data are calculated at $T = 300$ K.

Two main behavior of RDF are in fact observed in our system. Curves that show two peak within 6 Å from the protein and curves that don't. Former curves correspond to hydrated lysozyme sites, the latter to non-hydrated sites. The analysis of the water selected with criterion corresponds to analyze water that belong on average to the conventionally defined first and second hydration shell of hydrated sites plus few water molecules correspond to the non-hydrated sites. 1140 water molecules are found, on average, inside the 6 Å shell around the lysozyme at each time step. Note that these molecules are more than twice the water molecules contained in the reference bulk water system.

3.3. Results and Discussion

3.3.1. Density-Density correlation functions

The translational dynamics of hydration water has been characterized upon cooling by calculating the oxygen Self Intermediate Scattering Function (SISF), introduced in Section 2.3. This correlation function can provide valuable information to understand the relaxation mechanism in supercooled liquids.

The SISFs of hydration water were computed for oxygen atoms of water molecules inside the 6 Å shell around the lysozyme. Some particle in general will exit from the lysozyme hydration shell and other will enter.

SISF is calculated only for time interval that water molecules reside in the shell. Practically for hydration water the summation:

$$F_{self}(q,t) = \frac{1}{N}\left\langle \sum_{i=1}^{N} e^{-i\vec{q}\cdot[\vec{r}_i(t)-\vec{r}_i(0)]} \right\rangle \tag{3.1}$$

is restricted to oxygen atoms of water molecules for wich $\vec{r}_i(t)$ belong to the 6 Å shell around the lysozyme for all the temporal interval between 0 and t.

The SISFs reported in this Section are calculated at a transferred wave-vector $q = |\vec{q}_{max}| = 2.25$ Å^{-1}, namely at the first sharp peak of the oxygen-oxygen structure factor of water. At this wave-vector the features of the slow dynamics upon cooling are best evident as it corresponds to the length scale of the cage formed by the first nearest neighbors molecules [37]. The importance of the spatial-scale length have been addressed in the first chapter.

In order to gain enough statistics for the correlation functions of particles moving in such a small space, especially at long time, the trajectories of all the 13982 water oxygen atoms contained in the systems have been analyzed to achieve the best possible statistics from the stored MD trajectories. Issues related to the averaging over less particles have been described in Sec. 2.3.

In Figure 3.5 the computed SISFs for hydration water in the water-lysozyme aqueous solution are compared at selected temperatures with the SISFs calculated for bulk water.

Both the systems develop upon cooling a two step relaxation scenario typical of glass formers liquids with the correlators that become more and more stretched as the temperature decreases.

The global slowing down of the dynamics of hydration water with respect to the bulk is clearly visible from this Figure. At a given temperature, the correlator of hydration water always decays to zero on a longer time scale with respect to bulk water. This effect becomes more pronounced at low temperatures. At 200 K, correlations of hydration water are still not decayed to zero after 20 nanoseconds, while the bulk correlator at the same temperature decays at about 3 nanoseconds.

The major diversification in the dynamics of hydration water comes however from the persistence of correlation at long time, with correlation functions exhibiting long time stretched tails. These tails are already visible at visual inspection of the curves, especially at the lowest temperature where the two curves indeed almost coincide for two decades from the beginning of the plateau region and only after circa 100 ps the hydration water correlators begin to stretch showing long tails.

The SISFs coming from hydration water have therefore a different shape at long time.

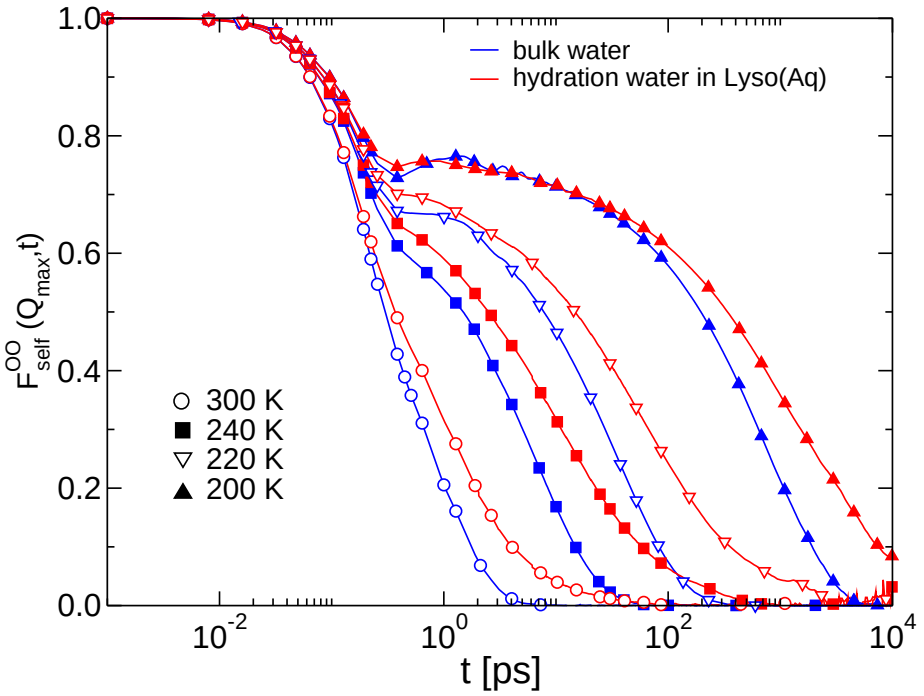

Figure 3.5: Comparison at selected temperatures of SISFs of bulk water (blue) and hydration water of the water and lysozyme system (red) calculated at the peak of the oxygen-oxygen structure factor $q = 2.25$ Å.

The shape of the SISF of supercooled bulk water was modeled according to MCT by Gallo et al. [42] and Sciortino et al. [43]. As seen in Sec. 1.2, to take into account both the fast subpicosecond relaxation and the α-relaxation and thus reproducing the two-step behavior of the SISF, the following functional form is required:

$$F_s(q,t) = (1 - f_\alpha)e^{-(t/\tau_s)^2} + f_\alpha e^{-(t/\tau_\alpha)^{\beta\alpha}} \tag{3.2}$$

Our bulk water SISFs fit eq. (3.2) (see figure 3.6) as expected.

We find instead that the SISFs of hydration water do not fit this model. In particular the onset of long time tails in hydration water cannot be taken into account by this equation.

Due to the long stretched tails the model described by Eq. (3.2) with a sum of a gaussian term and a stretched exponential function that fits bulk water fails to reproduce the long time behavior of density autocorrelation functions of hydration water.

When studying the dynamics of water in a disaccharides-water solution, Magno and Gallo [76] observed a behavior similar to that of our hydration water on the total correlator. They modified Eq. (3.2) by adding a second stretched exponential function to take into account a second

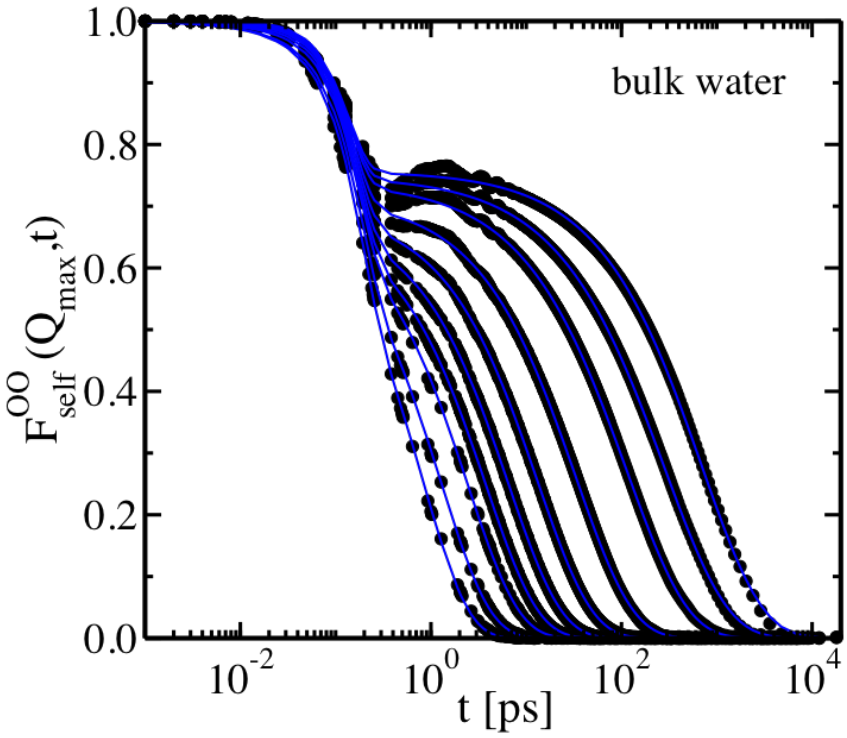

Figure 3.6: Self-intermediate scattering function (SISF) of the oxygen atoms of bulk water. SISFs (black filled circles) are calculated at the peak of the oxygen-oxygen structure factor $q = 2.25$ Å from $T = 300$ K (bottom curve) to 195 K (top curve). Continuous lines superimposed to the data are the best fit obtained using Eq. (3.2). The parameters of the fit are reported in table 3.2.

relaxation process not present in bulk water. With this modification, the SISF takes the form:

$$F_s(q,t) = (1 - f_\alpha - f_{long})e^{-(t/\tau_s)^2} + f_\alpha e^{-(t/\tau_\alpha)^{\beta\alpha}} + f_{long}e^{-(t/\tau_{long})^{\beta_{long}}} \quad (3.3)$$

Figure 3.7 shows the complete set of hydration water SISFs calculated from MD trajectories at the peak of the oxygen-oxygen structure factor of water. The temperatures range from 300 K down to 200 K. Superimposed to data points, best fits obtained via Eq. (3.3) are shown as continuos lines. This model well reproduces the long time behavior of the correlators of hydration water.

In previous studies on water and biomolecules performed in our group [76, 121] and in several experiments [68, 119] it had been impossible to distinguish whether the α-relaxation came only from those water molecules

not in direct contact with the biomolecule (bulk-like water) or also from the hydration layer, this was because they were looking at total correlator so that in the analysis both the hydration water and bulk-like water were included. Conversely, in the present analysis only water competing to the hydration shell of the protein is included in the calculation of the SISF, thus the two relaxations found compete exclusively to hydration water. With the high statistics reached in the present study, we can now assert that the translational relaxation of hydration water is not a simply bulk-like relaxation with a longer time constant. Hydration water relaxes through two distinct processes, an α-relaxation and a *long*-relaxation, occurring on two different time scales. The process labeled as *long* arises only for water close to the protein.

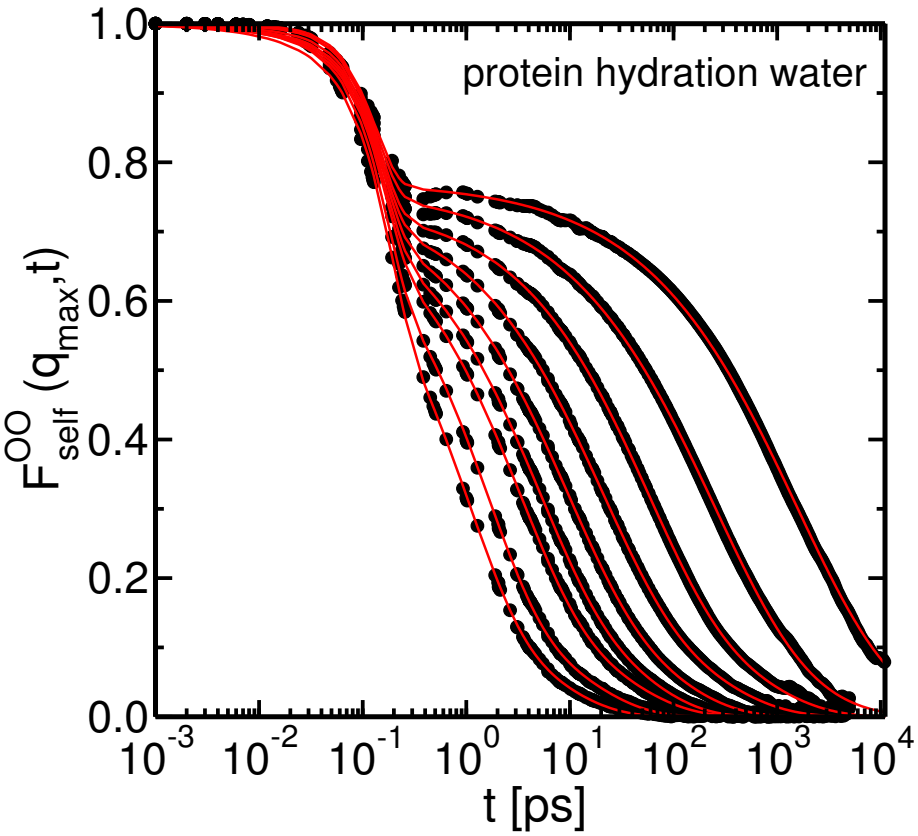

Figure 3.7: Self-intermediate scattering function (SISF) of the oxygen atoms of lysozyme hydration water. SISFs (black filled circles) are calculated at the peak of the oxygen-oxygen structure factor $q = 2.25$ Å from $T = 300$ K (bottom curve) to 200 K (top curve). Continuous lines superimposed to the data are the best fit obtained using Eq. (3.3). The parameters of the fit are reported in table 3.2.

The two relaxation times of hydration water extracted from the fit together with their respective stretching parameters are reported as a

Table 3.2: List of the fitting parameters of the SISFs the bulk water via Eq. (3.2) and of the SISFs of lysozyme hydration water via Eq. (3.3)

T (K)	System	τ_{short} (ps)	f_α	τ_α (ps)	β_α	f_{long}	τ_{long} (ps)	β_{long}
300	bulk	0.19	0.70	0.817	0.91	–	–	–
	hydration	0.19	0.51	0.960	0.80	0.20	4.72	0.62
280	bulk	0.19	0.70	1.26	0.83	–	–	–
	hydration	0.17	0.52	1.46	0.79	0.20	9.66	0.62
260	bulk	0.18	0.69	2.38	0.80	–	–	–
	hydration	0.17	0.54	2.85	0.68	0.19	24.3	0.61
250	bulk	0.18	0.68	3.75	0.79	–	–	–
	hydration	0.17	0.55	4.23	0.65	0.19	40.7	0.61
240	bulk	0.17	0.68	6.48	0.78	–	–	–
	hydration	0.16	0.53	7.58	0.61	0.22	65.2	0.59
230	bulk	0.16	0.69	13.1	0.76	–	–	–
	hydration	0.15	0.54	16.9	0.59	0.20	171	0.56
220	bulk	0.15	0.71	33.0	0.73	–	–	–
	hydration	0.15	0.54	47.3	0.59	0.20	449	0.56
210	bulk	0.14	0.74	113	0.68	–	–	–
	hydration	0.14	0.55	192	0.57	0.20	1130	0.51
205	bulk	0.14	0.75	284	0.66	–	–	–
	hydration	0.14	0.55	479	0.54	0.21	2200	0.49
200	bulk	0.14	0.76	698	0.69	–	–	–
	hydration	0.14	0.55	1390	0.52	0.22	3490	0.48
190	bulk	0.13	0.78	1960	0.64	–	–	–

function of temperature in Fig. 3.8. In the same figure, bulk water values are also reported. The structural relaxation time of hydration water, τ_α , shares the same time scale of the structural α-relaxation time of bulk water τ_α^{bulk}, i.e., tenth to hundred of picoseconds. Moreover, they display the same temperature behavior upon cooling, showing similar values apart from a slight slowing down of hydration water more evident at the lowest temperatures. The longer relaxation process, not present in bulk water, occurs over a longer time scale, from tens to thousands of picoseconds and the relaxation time τ_{long} shows a different temperature behavior.

Concerning the stretching parameters, at a given temperature, the structural relaxation of hydration water is more stretched than that of bulk water, since $\beta_\alpha < \beta_\alpha^{bulk}$, but they show the same temperature trend. In particular, upon cooling, the α-relaxation becomes more stretched, highlighting the increasing departure from an exponential decay, until

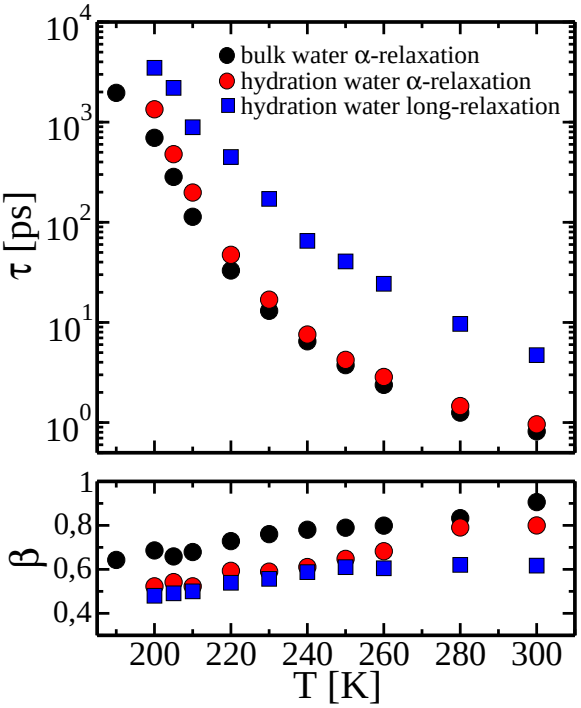

Figure 3.8: Upper panel: structural relaxation times, τ_α^{bulk} (black filled circles), τ_α (red filled circles), τ_{long} (blue filled squares). Lower panel: stretching parameters β_α^{bulk}, β_α and β_{long} (same symbols) as a function of temperature, extracted from the fit procedure as described in the text.

a constant value is reached at the lowest temperatures. The same temperature trends and similar values have been found for the stretching parameters of confined water [126, 127].

3.3.2. Temperature behavior of the α-relaxation

The structural α-relaxation times of bulk water is plotted on the Arrhenius plot of Figure 3.9. As expected for water, τ_α^{bulk} follows the MCT predictions and in the region of mild supercooling its temperature behavior is described by a power law of the form:

$$\tau_\alpha \sim (T - T_{MCT})^{-\gamma} \tag{3.4}$$

where T_{MCT} is the MCT temperature which marks the ideal transition from an ergodic to a non-ergodic phase.

As reported in Figure 3.9, the fit via MCT power law can be performed by excluding the lowest temperatures. The fit gives a MCT temperature $T_{MCT}^{bulk} = 193.8$ K and a power exponent $\gamma = 2.74$, in agreement with previous studies on the bulk phase [42, 43]. The divergency occurring at T_{MCT} is smeared out by hopping phenomena in most structural glass formers,

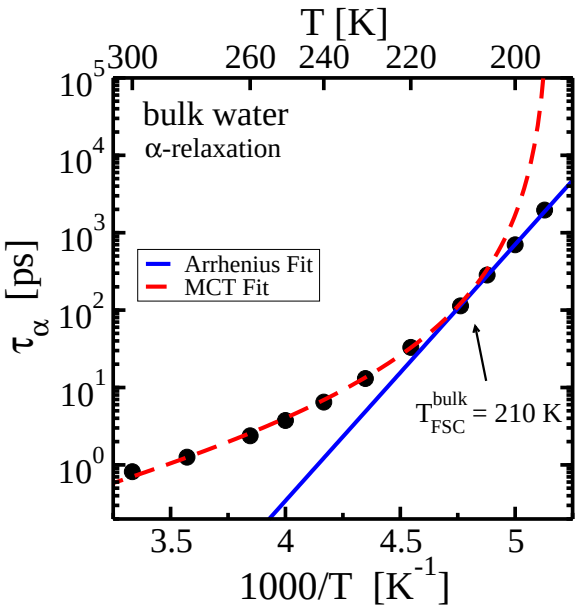

Figure 3.9: Arrhenius plot of the α-relaxation times τ_α in bulk SPC/E water along the $p = 1$ bar isobar. The points fit the MCT power law at high temperatures (red dashed line) and the Arrhenius law at low temperatures (blue continuos line). The fragile-to-strong crossover takes place at $\sim$ 210 K. See Table 3.3 for the fit parameters of the two regimes.

including water [42, 47]. The activation of hopping phenomena upon cooling changes the behavior of τ_α^{bulk} that begin to grows exponentially upon cooling following an Arrhenius law:

$$\tau_\alpha = \tau_0 e^{E_A/(k_B T)} \tag{3.5}$$

where E_A is the activation energy of hopping phenomena. The lowest temperature points behavior are indeed described by the Arrhenius law with an activation energy $E_A^{bulk} = 63.4$ kJ/mol. Therefore a crossover from a fragile, power-law, regime to a strong, hopping dominated, Arrhenius regime occurs. The fragile-to-strong crossover in SPC/E bulk water along the 1 bar isobar occurs at a $T_{FSC}^{bulk} \sim 210$ K. Same values for both the activation energy and the temperature of the FSC were reported in Ref. [128] as extracted from the FSC of the diffusion coefficient $D \sim \tau_\alpha^{-1}$.

MCT behavior have been also tested on the τ_α of protein hydration water, shown in Figure 3.10. Despite the moderate slowing-down induced by the protein, the α-relaxation time of hydration water is not dramatically influenced by the protein and retains the same phenomenology of bulk water.

In particular, it follows the MCT predicted power law with an higher MCT temperature $T_{MCT} = 199.0$ K and a power exponent $\gamma = 2.68$ similar to

the bulk. The deviation from the MCT prediction occurs at $T_{FSC} \sim 215K$, when the FSC takes place. Below this crossover temperature hydration water can be described as a strong liquid with a slightly lower activation energy with respect to the bulk, $E_A = 61.9$ kJ/mol (Figure 3.10). Fit parameters are also reported together with bulk parameters in Table 3.3.

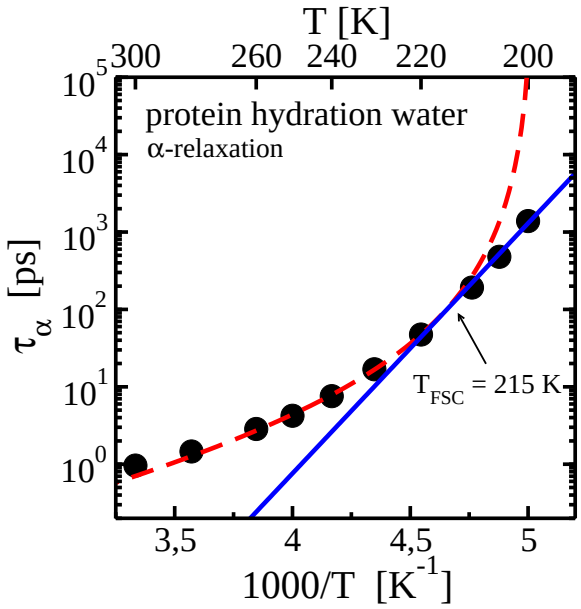

Figure 3.10: Arrhenius plot of the α-relaxation times τ_α in lysozyme hydration water. The points fit the MCT power law at high temperatures (red dashed line) and the Arrhenius law at low temperatures (blue continuos line). The fragile-to-strong crossover takes place at ~ 215 K. See Table 3.3 for fit parameters of the two regimes.

The phase diagram of bulk supercooled water is very complex, this has already been discussed in Chapter 1. The FSC of the structural α-relaxation in water has been related to the crossing of a liquid-liquid Widom line [32, 38, 47, 49, 129], the line of collapse of the maxima in response functions that converge to a liquid-liquid critical point [6, 9, 10]. Therefore the FSC that we found could be the trace of the presence of a liquid-liquid Widom line and consequently of a LLCP in the phase diagram of protein hydration water. This possibility has been discussed, for example, in Refs. [60], [130] and [131]. Besides, both the mode coupling temperature T_{MCT} and the FSC temperature T_{FSC} of protein hydration water are about five degrees higher with respect to the bulk water values. The shift of water dynamics to higher temperatures has also been observed for many systems including sugar-water solutions [76, 121], electrolytes solution [132–134] and confined water [126, 135, 136]. This indicates the possibility that exploring the phase diagram of hydration

Table 3.3: MCT temperature (T_{MCT}), γ exponent, activation energy (E_A), and FSC temperature (T_{FSC}) for the α-relaxation of bulk SPC/E water and SPC/E water of hydration of lysozyme.

	T_{MCT} (K)	γ	E_A (kJ/mol)	T_{FSC} (K)
bulk water				
τ_α	193.8	2.74	63.4	210
hydration water				
τ_α	199.0	2.68	61.9	215

water and finding a shifted LLCP may overcome experimental issues related to the crystallization of bulk water [26] .

The Widom line separates a high density liquid phase region from a low density one, where the less dense liquid favors the hopping processes and therefore the strong behavior of water. The similar value of activation energy of bulk and hydration water supports the idea that the leading dynamic process in the region below the FSC is the same. In the region where hopping phenomena occur, the translational dynamics of water is dominated by potential barriers described by Goldstein [41]. In this regime the activation energy of Arrhenius law is presumably the activation energy of the jump between these barrier. In the strong side the motion of the molecules is then realized with fluctuation in density that involves the disrupt of the hydrogen bonds with nearest neighbor molecules, in this sense the activation energy plausibly depends on the energy of hydrogen bonds [137]. Gillen, Douglass, and Hoch [138] reported experimental activation energies from the self-diffusion coefficient in water in the broad range (242-473) K. The activation energy is increasing upon cooling water. At 242 K, E_A^{bulk} is $\sim$ 46 kJ/mol, this value approximately corresponds to the energy required to break four hydrogen bonds at that temperature. Recently Dehaoui, Issenmann, and Caupin [139] reported $E_A^{bulk} \sim 53$ kJ/mol for the low temperature activation of the viscous flow, even if they also show a dynamic decoupling between viscosity and diffusion coefficient at low temperature in water. It appears however that in supercooled real water, E_A^{bulk} is increasing upon decreasing temperature toward the value reported in ice Ih ($E_A^{Ih} \sim 61$ kJ/mol [140]). We note that the ice value practically coincides with the values that we found for both SPC/E bulk and hydration water, as extracted from our low temperature ($T < 220$ K) behavior of the α-relaxation times, which cannot be probe in experiments due to the limitations of freezing. This also prompts to another observation: in the strong regime, water has been shown to be below the Widom line and therefore on the low density

side of the liquid [32, 38, 47]. The low density liquid is characterized by a more open and locally tetrahedral structure [28, 141]. We can argue that locally its structure is more close to the ice one and therefore that the energy required to rearrange is similar. This could explain the similar activation energy of bulk water, hydration water and ice Ih.

In summary, the performed MCT test on the τ_{alpha} of protein hydration water in our system establishes that the correspondent process is an α-relaxation typical of glass formers and it is analogous to that of bulk water.

The α-relaxation and the FSC in hydration water was also found on a slightly different system: a lysozyme protein with a monolayer coverage of water both in experiments and in simulations [54, 59, 142]. In these studies the FSC of hydration water is located at about $220-240$ K. It should be noted, however, that the water monolayer coverage in simulation and the water monolayer coverage in the powders of the experiments [54, 59, 142] could introduce differences in dynamics with respect to our hydration water in a solution. Besides, at the q values investigated in these works (less or equal to $q = 1.1$ Å), the two slow relaxations have different weights in the correlators with respect to the ones that we have at the first peak of the oxygen-oxygen structure factor and might not be distinguishable.

3.3.3. Temperature behavior of the long-relaxation

The second relaxation time, τ_{long}, extracted from the fit via Eq. (3.3) of the SISFs of hydration water is reported in Figure 3.11.

It is evident from the figure that two distinct dynamic regimes, both linear on the Arrhenius plot, occur. Data points can be fitted to an Arrhenius law $\tau_{long} = \tau_0 e^{E_A/(k_B T)}$ through two different activation energies: a lower one for the high temperature regime $E_A^{HT} = 26.6$ kJ/mol and a higher one for the low temperature regime $E_A^{LT} = 39.3$ kJ/mol. This strong-to-strong crossover (SSC) appears at about $T_{SSC} \sim 240$ K.

The stretching exponent β_{long} of this relaxation, see Fig. 3.8, is almost constant at the highest temperatures, and shows a slight decrease at low temperatures starting at about 240 K following the crossover of its relaxation time τ_{long}. At high temperature, the long-relaxation appears globally more stretched than the α process, while below 240 K they reach similar values.

Given also the experimental evidence discussed in the introduction, [50, 116, 119, 122, 123] we ascribe the existence of this long-relaxation time and its behavior to the coupling of hydration water with protein structure fluctuations. In particular, the long time rearrangements of water molecules dragged by the protein cause the onset of the long-relaxation of hydration water. When the protein moves, water molecules

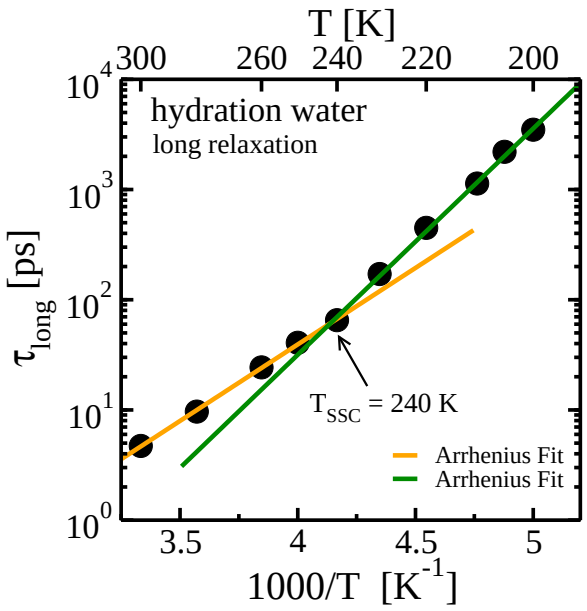

Figure 3.11: Arrhenius plot of the long-relaxation time τ_{long} of hydration water. The points fit Arrhenius laws with different activation energies at high temperature, E_{A_1}, and at low temperature, E_{A_2}. The crossing between the two regimes occurs at $T_{SSC} \sim 240$ K.

in the hydration shell have to reorganize according to the protein motion. Protein motions like rotations of side chains at surface (10-10^2 ps at room temperature) or relative motions of globular domains (10-10^5 ps) happen on long time scales, typically much longer than that of water network relaxation. The water network can thus relax for the α-process independently, which is what we observed in the present study. In other words, due to the different time scales, water molecules see the protein at fixed position on the α-timescale and can relax and diffuse as in bulk-like environment (α-relaxation and FSC to hopping), only over long times the water network follows the protein changes of shape (long-relaxation and SSC). The onset of this second, longer relaxation in hydration water should be therefore strictly connected to the fluctuations in the protein structures.

3.3.4. Coupling water-protein: the Protein Dynamical Transition

To investigate the coupling between the lysozyme and its hydration water and to test our interpretation, we calculated the mean square fluctuation (MSF) of hydrogen atoms of lysozyme. We choose hydrogen atoms because they are the lightest and the most mobile over the surface of the protein and therefore a useful probe for the mobility of the protein surface.

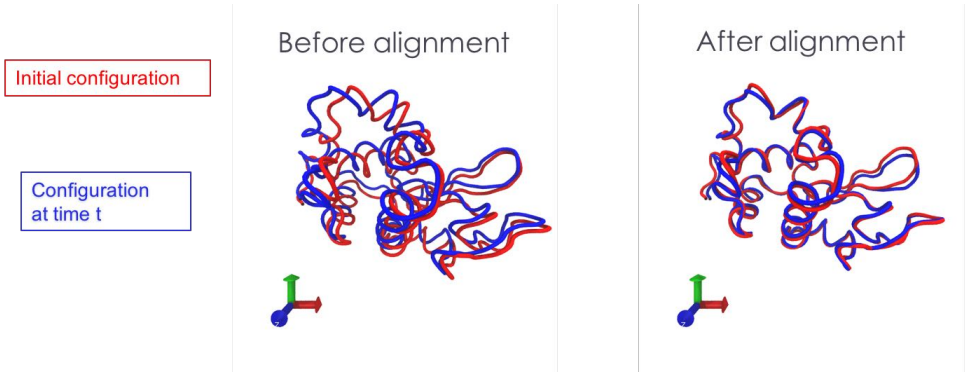

Figure 3.12: Alignment of protein structures.

Before the calculation of the MSF, an alignment of the protein structure is needed to remove the global translational and rotational motion of the protein inside the simulation box during the trajectory. Only in this case the MSF computed with:

$$MSF = \frac{1}{T}\sum_{t=1}^{T}(\mathbf{r}(t) - \mathbf{r}(0))^2 \tag{3.6}$$

can be considered as measure of fluctuations in the structure of the protein itself. This procedure is depicted in Figure 3.12. The protein structure at time t is compared to its reference initial structure. Then the alignment is performed through a least-squares fitting procedure of the two compared structures that minimize the spatial distance between the protein tertiary structures. This procedure is repeated for each stored time-step t. From the aligned structures it is possible to calculate a time dependent MSF of hydrogen protein atoms, this is then averaged over the last 1 ns of the simulation. Figure 3.13 displays the final protein MSF as a function of temperature for our system.

According to Ref. [53], the MSF of a protein is made of two contributions, a vibrational component that dominates at low temperatures and that, apart from the zero-point constant value, is linear with the temperature. The second contribution is the conformational component, which is temperature activated and absent when the protein is dry.

We clearly observe a dynamic transition in the protein MSF at about $T \sim 240$ K. The MSF is in fact weakly dependent on temperature below 240 K. At ~ 240 K its slope changes and increases. This steep increase means that the protein structure fluctuations are enhanced above 240 K and this activates the functioning of the protein. This transition is the well-known Protein Dynamical Transition (PDT) [143]. The PDT is linked to changes in the conformational states of the protein and it was

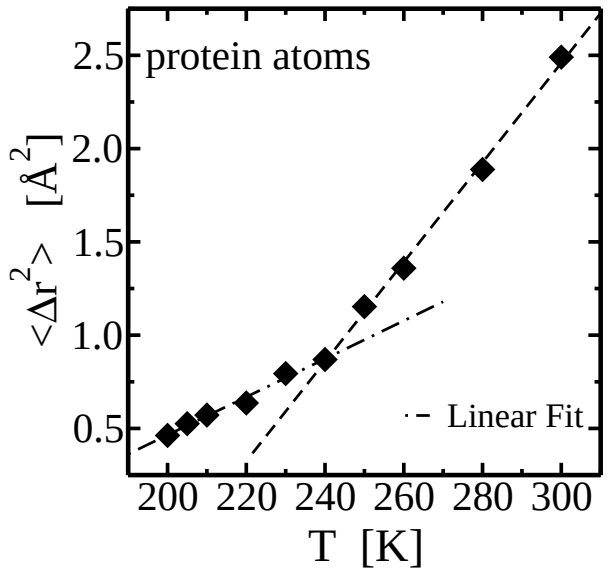

Figure 3.13: MSF of protein hydrogen atoms as a function of temperature. Each point represents the average over the last nanosecond of the collected MD trajectory. The MSF exhibits a crossover at $T = 240$ K. Dashed lines are best fit lines done to determine the crossover location.

observed both in neutron scattering experiments [54–56, 144, 145] and in simulations [55, 57–60]. Importantly, various studies showed that the PDT occurs for small globular proteins always between 220 K and 240 K quite independently of the water potential used, see for example Refs. [57] and [58] for SPC/E water, Refs. [55] and [59] for TIP4P-Ew water, Ref. [60] for TIP5P water.

We therefore located the PDT of our lysozyme protein at about $T = 240$ K, at the same temperature at which the crossover (SSC) of the long-relaxation occurs. This indicates that the two phenomena are dynamically linked.

As a final comment on the connection between the MSF and τ_{long}, it is worth noting that the more the protein fluctuates, the faster the long-relaxation of hydration water is. In that respect the crossing to a lower activation energy upon increasing temperature is a consequence for hydration water of the coupling with the faster protein fluctuations at high temperatures.

3.3.5. Boson Peak and finite size effects

We briefly resumed here, that the BP, usually observed in the terahertz region in many supercooled and glassy sistems, is a collective mode that appears as an excess density of vibrational states over the density

predicted by Debye model ($g(E) \propto E^2$). Bulk, confined and biological water all show this feature [119, 146–149].

Figure 3.14 corresponds to the magnification in the region between (0.01 - 100) ps of the SISFs of bulk water (upper panel) and hydration water (lower panel) already shown in Figure 3.7 at the simulated temperatures from $T = 250$ K to $T = 200$ K.

Starting from $T = 210$ K and below this temperature the SISFs of bulk water show a minimum at $t = 0.4$ ps, a maximum at $t = 0.8 - 0.9$ ps followed by another maximum at $t = 1.5$ ps and an oscillation between 3 and 10 ps. The first two features (minimum and first maximum) are an overshoot of the density correlator that exceeds its final value (the plateaux value is related to the Debye-Waller factor): this is the so called Boson Peak (BP). The second maximum and the following oscillations (not clear if actually part of the same feature) are finite size effects demonstrated to vanish and shift to longer time respectively as the size of the simulation box increases, see in particular Kumar et al. in [149]. The Boson Peak in our SPC/E bulk water it is about 37 cm^{-1} in accordance to what found both computationally with TIP4P/2005 [149].

The BP is also present in our hydration water, see the bottom part of Figure 3.14. The first local minimum is at the same position, $t = 0.4$ ps, whereas the maximum slightly shifts to shorter times, $t = 0.8$ ps (circa 40 cm^{-1} as found in Ref. [149]). In protein hydration water the BP arises between $T = 220$ K and $T = 210$ K as in bulk water, with an overall spread of the overshoot less pronounced. On the contrary the second maximum is missing and the oscillations start at longer time (about 4-5 ps). This is consistent with the highly increased number of water molecules contained in this simulation box (13982 vs 500 in bulk box), for which size effects are expected to be absent or anyway strongly smeared out.

The BP is an highly debated low temperature feature of supercooled water. This should be a sort of signature of the disordered amorphous state of water. Recently its onset in water has been also connected to the presence of a liquid-liquid WL both in bulk and confined water [149–153]. This was interpreted as changes in the local structure in water when crossing from the high density liquid-phase to a low density liquid phases of water. We see in fact that this also holds in protein hydration water. Approximately between the 220 K and 210 K we located the appearing of the BP in our SISFs, in coincidence with the fragile to strong crossover of the α relaxation time ($T_{FSC} \sim 215$ K).

3.4. Conclusions

In summary, we have shown that the translational dynamics of water proximal to protein shows two well distinct slow relaxation processes.

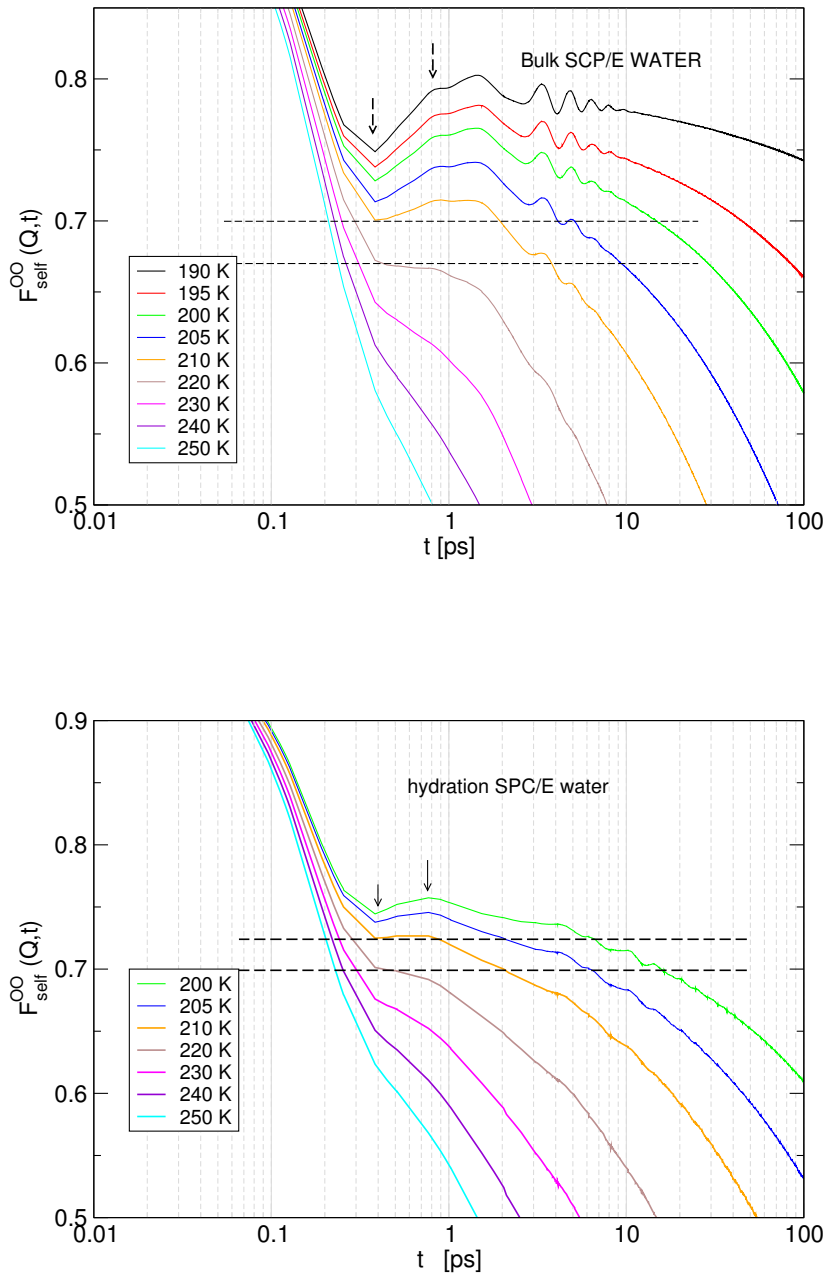

Figure 3.14: Enlargement of the Boson Peak area for bulk water (upper panel) and lysozyme hydration water (bottom panel). Dashed lines are guide for eyes indicating the position of the first local minimum in the region $t < 1$ ps of the respective top curve. In both systems the SISFs develop a local maximum between $T = 220$ K and $T = 210$ K upon cooling the systems. This matches the Fragile to Strong crossover we observed in the α-relaxation times.

The first one, happening on the faster time scale between the two, is the α-structural relaxation typical of glass formers and in particular of bulk water. This relaxation in water is due to the continuous breaking and reforming of hydrogen bonds. The structural relaxation time of the α process exhibits a fragile to strong crossover upon cooling, which might be associated with the crossing of the Widom line as it happens in the bulk phase.

The second relaxation, absent in bulk water, happens on a longer time scale and appears to be the macroscopic effect of the dynamic coupling between hydration water and the protein. It exhibits a change in the temperature trend at $\sim$ 240 K and this temperature corresponds to an enhancement in the mean square fluctuations of protein atoms, the PDT.

Based on our results, we conclude that the complex thermodynamics of supercooled water plays a fundamental role only in the α-relaxation, while it seems that the long-relaxation is completely driven by the protein motion.

It is worth highlighting that the dynamics that we characterized in the hydration shell of lysozyme extends on nanosecond time scale and in this lapse of time, the single particle visits both hydrophilic and hydrophobic sites of the protein. This type of analysis has the averaging character of several experimental techniques that are not sensible to site-specific interactions, like quasielastic neutron scattering. Our characterization of hydration water relaxation times can help experimentalists to interpret the information coming from total correlators in order to better characterize hydration water relaxations in different proteins and possibly biomolecules.

4

The trehalose protein system

In this Chapter results on the ternary system composed of a lysozyme protein immersed in a trehalose-water solution are presented through a comparative study of this system with the lysozyme immersed in pure water and bulk water. We characterized the relaxations of hydration water and the internal dynamics of the protein in Subsec. 4.2.1, dynamics of hydration water in terms of the mean squared displacement of hydration water in Subsec. 4.2.2. The structural analysis of water and trehalose molecules around the protein is presented in Subsec. 4.2.3 and hydrogen bonding behavior of water in the three systems is presented in Subsec. 4.2.4. Sec. 4.3 is devoted to the final discussion and conclusions.

4.1. System & Simulation Details

Our system is composed by 1 lysozyme protein, 13982 water molecules, 491 trehalose molecules and 8 Cl^- ions. The total number of atoms in the cubic simulation box is 66 009. The counterions neutralize the charged residues of lysozyme and maintain electric neutrality of the global system during simulations. The sugar-water solution has a mass fraction of 40 % in trehalose, the global system (protein+trehalose+water) is 38.7 wt % trehalose, 58 wt % water and 3.3 wt % lysozyme.

We have carried out classical molecular dynamics all-atom simulations using the GROMACS 4.5 [91, 125] package. We used the CHARMM force-field for proteins [103, 104] and for sugars [108, 109] for modeling the bonded and non-bonded interactions of lysozyme and trehalose molecules, respectively. Water is described with the SPC/E potential [94]. The system is simulated at a constant pressure $p = 1$ bar for ten different temperatures starting from $T = 300$ K down to $T = 200$ K. Both the temperature and the pressure of the system were handled during the simulations with the Berendsen method [93], described in Subsec. 2.1.3.

Table 4.1: Summary of the simulated state points at $p = 1$ bar including the temperature T, density ρ and potential energy U of the Lyso(Treha-Aq) system. At each temperature the equilibration run of length t_{eq} is followed by the data collecting for a time t_{prod}.

T (K)	ρ (g/cm^3)	U (kJ/mol)	t_{eq} (ns)	t_{prod} (ns)
300	1.175	-288531	12	20
280	1.187	-312829	15	20
260	1.197	-337058	15	20
250	1.201	-349416	30	20
240	1.204	-361738	60	20
230	1.207	-374200	70	40
220	1.209	-386309	70	40
210	1.209	-398196	70	50
205	1.210	-404481	70	50
200	1.210	-409764	70	50

In Tabel 4.1 we give a summary of the ten simulated thermodynamic states, which include the values of the density ρ, of the potential energy U of the system calculated as the mean value over the production run and the lengths of the equilibration and production runs. From those trajectories we calculated the quantity presented in this work. The total computational time amounts to more than 810 ns, which is equivalent of ten years and a half of continuous single CPU usage.

This simulation set was aimed to analyze the dynamics of water close to the protein, the hydration water and compare its dynamics to the results obtained in Chapter 3 on the dynamics of lysozyme hydration water in a system where the lysozyme was immersed in water. For sake of comparison we adopted the same criterion to select the lysozyme hydration water molecules, namely water molecules at a distance minor or equal to 6 Å from any lysozyme atoms. Approximately 710 water molecules and 38 trehalose molecules are found within 6 Å from the protein surface in our system at each time step. A trehalose molecule is considered within the hydration shell if its center of mass (linkage between the two glucose unit) matches the distance criterion. Hydration water molecules are highlighted in figure 4.1, that displays a cut through the cubic simulation box of Lyso(Treha-Aq) system at $T = 300$ K.

4.2. Results

4.2.1. Relaxations of protein hydration water

Figure 4.2 displays the Self Intermediate Scattering Functions calculated for the oxygen atoms of hydration water molecules at a transferred wave-vector $q = 2.25$ Å^{-1}. SISFs are shown at all the simulated temper-

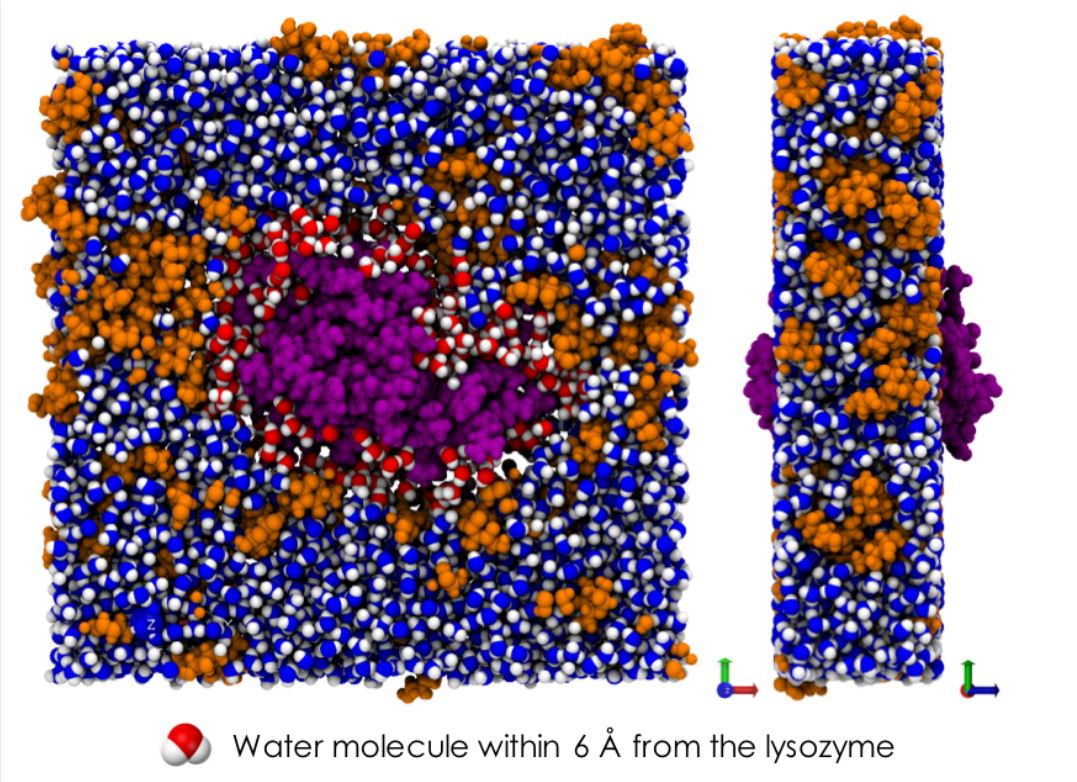

Figure 4.1: Snapshots of the Lyso(Treha-Aq) system at $T = 300$ K. The simulation box is shown at $x - y$ projection and $y - z$. The solution is shown performing a 20 Å thick cut along the z direction, the lysozyme is entire. Lysozyme in colored in purple, trehalose molecules in orange, water in blue-white and hydration water in red-white.

ature from $T = 300$ K to $T = 200$ K.

Upon cooling, we observe at short time the initial ballistic regime with the correlators showing the fast Gaussian decay. This regions is weakly dependent on the temperature and diversifications in SISFs calculated at different temperatures arise at about $0.2 - 0.4$ ps. Then, the dynamics is determined by the cage effect, as in bulk water and in the hydration water in the trehalose-free system. The tagged particle is trapped inside the cage formed by nearest-neighbor molecules for increasing time upon cooling, this corresponds to correlators that exhibit plateaux regions more and more extended in time upon decreasing temperature. Only when the cage melts, the particle can enter the diffusive regime and correspondently the plateaux region is followed by the α-decay of SISFs. This is eventually followed by the long-time decay to zero of SISFs which show stretched tails. Those tails, clearly distinguishable down to about 240 K, stretch the correlation over long time and are the hint of the presence of a second longer relaxation.

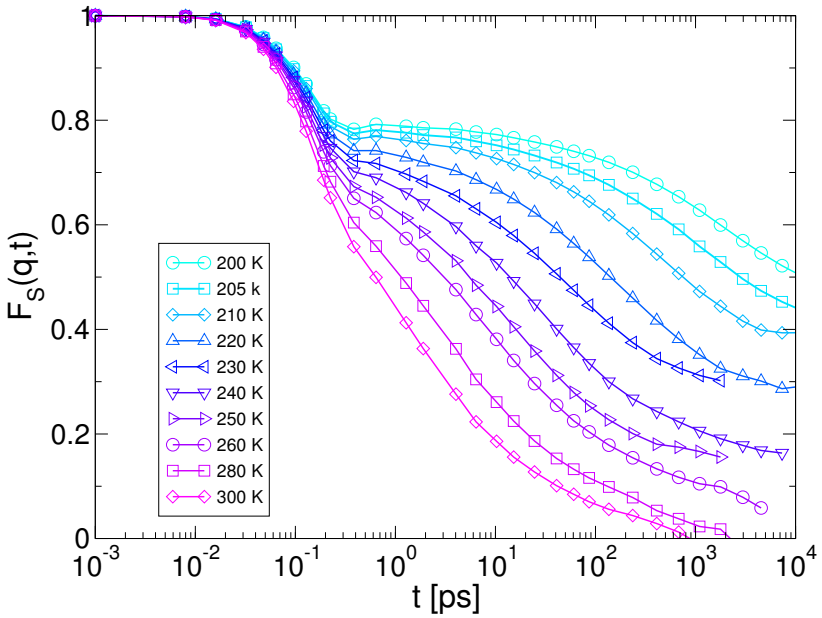

Figure 4.2: Oxygen Self intermediate scattering functions of water molecules in the hydration shell of lysozyme when immersed in the trehalose-water solution. Temperatures span from T = 300 K (bottom curve) to T = 200 K (top curve).

Trehalose strongly affects the dynamics of water at the protein interface, whose motion in the 6 Å-shell is greatly slowed down. This is better evinced by looking at Figure 4.3, where at selected temperatures we compare the SISFs of hydration water in the lysozyme+trehalose+water system (Lyso(Treha-Aq)) with the SISFs of hydration water in the lysozyme

+water system (Lyso(Aq)) and with the SISFs of bulk water.

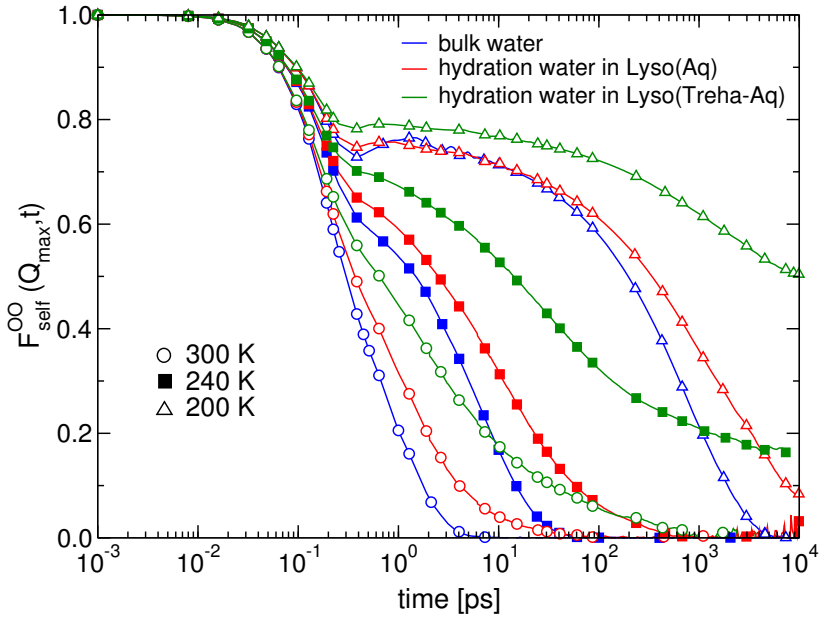

Figure 4.3: Oxygen Self intermediate scattering functions of bulk water (blue), of water in the hydration shell of lysozyme immersed in pure water (red) and of water in the hydration shell of lysozyme immersed in trehalose-water (green). SISFs are shown at three selected temperatures: $T = 300$ K (○), $T = 240$ K (■) and $T = 200$ K (△) for comparison among the three systems. The presence of trehalose greatly affects the slow dynamics of the long time tail.

At a given temperature, the correlator of hydration water in Lyso(Treha-Aq) is always higher in respect to Lyso(Aq) and bulk water. For example at the highest temperature $T = 300$ K the SISFs of bulk water, hydration water in Lyso(Aq) and hydration water in Lyso(Treha-Aq) decay to zero at 10 ps, 100 ps and 1000 ps respectively. This situation is amplified at the lowest temperature, where hydration water in Lyso(Treha-Aq) is far from the complete relaxation on the 10 ns time scales, correlation are in fact still very high (> 0.5). The corresponding process in absence of trehalose decorrelates of more than 90% during the same time.

The overall height on the plateaux $A(q)$ in the SISF plays the role of the Lamb-Mössbauer factor, which is connected to the mean square vibrational amplitude a of the particle inside the cage through the relation $A(q) = exp(-q^2a^2/3)$. The general feature that $A(q)$ increases upon cooling indicates that the particle are less mobile at low temperature. Note that inside the cage the vibrations occur over shorter distance at a fixed temperature when trehalose molecules are in the solution. At the lowest temperature $A(q)$ coincides in bulk and hydration water in Lyso(Aq) while

it is greater in the protein hydration water of sugar-water solution. This is the further evidence that hydration water in presence of trehalose is hindered in its motion.

Through the direct comparison of hydration water correlators to the bulk ones, a different long-time behavior is evidenced already at high temperature. Also coming back to Figure 4.2, it is evident that the SISFs calculated at high temperatures show the stretched tails revealing the long relaxation. SISFs calculated at low temperatures miss the full decay to zero because of the very slow dynamic of water near the lysozyme whose complete relaxation exceeds the time scale of the simulation. In this case it is difficult to infer the presence of the long relaxation at a visual inspection of the curves, and thus it is mandatory to perform a fitting procedure to determine the possibility of extracting the long relaxation. All these drawbacks made accurate estimation of the long relaxation times very difficult in general.

In Figure 4.4 the best fit to the model which takes into account the Gaussian term plus two stretched exponential functions (Eq. (3.3)), that describes density-density correlators of hydration water, is shown superimposed to the data points. In the same Figure also the best fit to the model which takes into account the Gaussian term plus only one stretched exponential function (Eq. (3.2)), that describes density-density correlators of bulk water, is reported.

It is evident that the model that takes into account two structural relaxations can reproduce the data on a more extended temporal window with respect to the model described by only one structural relaxation. Especially at long time, the model fitting bulk water SISFs fail to reproduce the long stretched tails. The deviation from the single structural relaxation behavior happens at longer time upon cooling the system and at higher correlation values, this is due to the increase of the characteristic times of the relaxational processes and to the increase of the amplitude of the longer relaxation upon decreasing temperature with respect to the α-process.

The complete set of parameters extracted from the fitting procedure via Eq. (3.3) is plotted on the graphs of Figure 4.5. We show in panel a) the characteristic time τ_s of the fast relaxation described by the gaussian term of Eq. (3.3) which is approximately constant in temperature; in panel b) the relative amplitude of the two structural relaxations, f_α and f_{long}, which cross between 230 K and 240 K; in panel c) the stretching exponents β_α and β_{long}; in panel d) the structural α-relaxation time and in panel e) the long- relaxation time of lysozyme hydration water of the ternary system. In the same plots are also reported values of protein hydration water in Lyso(Aq) and bulk water for comparison.

Trehalose molecule slow down both the structural relaxation process,

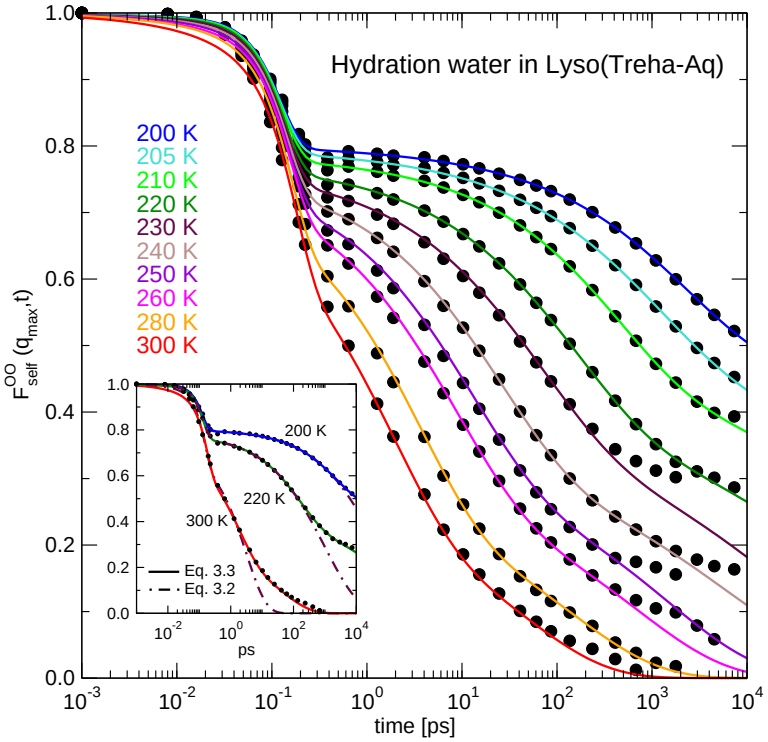

Figure 4.4: Oxygen Self Intermediate Scattering Function of water molecules in the hydration shell of lysozyme when immersed in the trehalose-water solution (symbols). Temperatures span from T = 300 K (bottom curve), to T = 200 K (top curve). Continuos line are best fit obtained using Eq. (3.3). In the inset the same curves are reported for selected temperatures together with the best fit obtained using the Eq. (3.2), which is able to fit only one relaxation.

but the extent of the slowing down depends on the relaxation type. The presence of trehalose induces a mild slowing down on the α process. The α-relaxation times lyes in fact on the same time-scale of the corresponding process of protein hydration water in Lyso(Aq) and of bulk water. The degree of slowing down is consistently greater on the long relaxation, whose retardation factor with respect to in the absence of the sugar is about one order of magnitude at $T = 300$ K and reaches three order of magnitude at lowest temperature

Trehalose has also the effect to ulteriorly stretch the dynamics of hydration water. Both β_α and β_{long} are decreased at all the temperature. β_α resembles the temperature behavior of bulk and hydration water in Lyso(Aq), i.e. a slight decrease upon decreasing temperature toward constant value. Also the behavior of β_{long} is similar to that of protein hydration water in Lyso(Aq), but it shows a more sharp transition to the low temperature regime where it decreases upon cooling. This occurs be-

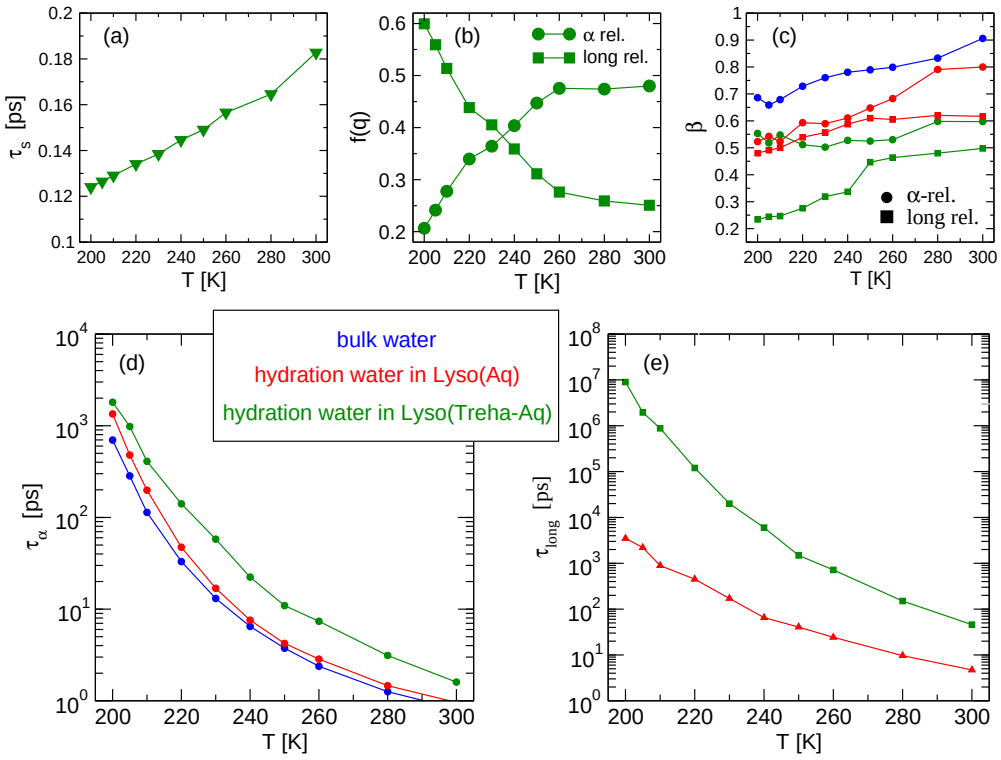

Figure 4.5: Results of the fitting procedure via Eq. (3.3) of SISF shown in Fig. 4.4. The panels show τ_s (a), the amplitude f_α and f_{long} (b) and the stretching parameters β_α and β_{long} (c) of the two structural relaxations of hydration water. The α-relaxation times is compared with the corresponding relaxation in the Lys(Aq) and bulk water systems in panel (d). The long relaxation time is compared with the corresponding long relaxation in the Lys(Aq) in panel (e).

tween 250 K and 240 K.

To investigate more deeply to what extent the two structural relaxations of hydration water are modified when a cryoprotector is added, we study the temperature behavior of the both τ_α and τ_{long} in this system. In particular it is important to study if the cryoprotector modify the temperature behavior of the relaxations found in Chapter 3.

In figure 4.6 we show on an Arrhenius plot the α-relaxation time of hydration water extracted from the fit of SISFs, same data on Figure 4.5(d).

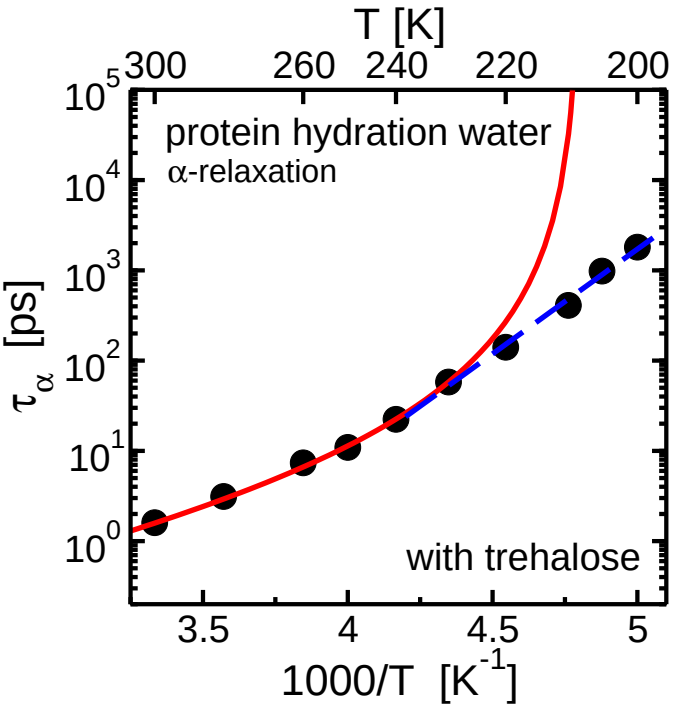

Figure 4.6: Arrhenius plot of the α-relaxation times τ_α of hydration water in Lyso(Treha-Aq). Data points fit the MCT power law at high temperatures and the Arrhenius law at low temperatures. See table 4.2 for the fitting parameters of the two regimes.

We showed that the α-relaxation time of protein hydration water in Lyso(Aq), along the 1 bar isobar, can be described by the MCT power-law upon cooling then a FSC occurs. The MCT power law well describes also the temperature behavior of τ_α in hydration water in presence of trehalose. This is true from the highest temperature down to about T = 220 K. At this temperature the data points deviate from the MCT power-law towards the Arrhenius law. The MCT behavior is characterized by a MCT temperature T_{MCT} = 203 K and a power exponent γ = 2.48, the activation energy in the Arrhenius side is E_A = 47.1 kJ/mol. These values

Table 4.2: MCT temperature (T_C), MCT γ exponent, low temperature activation energy E_A and FSC temperature (T_{FSC}) for the α-relaxation and activation energies at high (E_A^{HT}) and low (E_A^{LT}) temperature of the long-relaxation of hydration water in the Lyso(Treha-Aq) extracted in the present work. Corresponding values of hydration water in the Lyso(Aq) and bulk water are also reported for comparison. Note that the long relaxation is missing in bulk water.

	α-relaxation				long-relaxation		
Sys.	T_C (K)	γ	E_A (kJ/mol)	T_{FSC} (K)	E_A^{HT} (kJ/mol)	E_A^{LT} (kJ/mol)	T_{SSC} (K)
lysozyme hydration water in Lys(Treha-Aq)							
	208.6	2.50	44.4	230	43.9	76.0	240
lysozyme hydration water in Lys(Aq)							
	199.0	2.68	61.9	215	26.6	39.3	240
bulk water[1]							
	193.8	2.74	63.4	210	-	-	-

are also reported in table 4.2 together with the values of hydration water in the Lys(Aq) system and bulk water.

The addition of trehalose molecules in water further increase the T_C and decrease the power exponent γ values of hydration water of lysosyme in respect to the bulk. This also causes the crossing between the fragile regime to the strong regime to occur approximately at $T_{FSC} = 230$ K, about 10 degree higher than in bulk water and 5 degrees higher with respect to the Lyso(Aq). This shift is evidently consistent with the one of the MCT temperature. This fact may have cryopreservation implications.

Below the temperature of the fragile to strong crossover, hydration water in both system behaves as a strong liquid but with different activation energies. With trehalose the activation energy decreases with respect to in Lyso(Aq) and bulk water. It has been shown [154] that in pure water hopping phenomena are more pronounced when water is more structured and less mobile. It is reasonable that this situation is accompanied by the decrease of the activation energy of the Arrhenius regime, in this way the hopping of a water molecule is favored because of the less high energy barrier. We have shown that water at the protein interface is less mobile when trehalose in the solution from Lamb-Mössbauer factor. Beside it has been shown that trehalose induces a structuring of water molecules [155, 156]. We can comment the minor value of E_A that we found in Lyso(Treha-Aq) in respect to Lyso(Aq) by arguing that this is linked to a further ordering of water at the protein interface in presence of trehalose.

To conclude the discussion on the α-relaxation, it must be mentioned again the connection within the FSC phenomenon of this relaxation to crossing of the liquid-liquid Widom line upon cooling. The FSC in pro-

tein hydration water and the connection with the Widom line has been deeply investigated in protein-water systems, not in ternary systems to the best of our knowledge. Since trehalose seems to not affect the phenomenology of this relaxation (i.e. the FSC), but only to shift it to higher temperature, we do not exclude the possibility of a liquid-liquid Widom line in the phase diagram of the water contained in the solution at the protein interface.

In summary, the α-relaxation keeps its phenomenology unchanged in presence of trehalose molecules, the relaxation time τ_α shows a FSC upon cooling, being its behavior described by the MCT at high temperature and by Arrhenius law at low temperatures. The effect of trehalose in this solution is to further shift the dynamics at higher temperature.

Now we discuss the temperature behavior of the long process and its connection to protein atomic mean fluctuations.

Figure 4.7 displays the Arrhenius plot of the long-structural relaxation time τ_{long} extracted from the fit of density-density correlators via Eq. (3.3). In this plot two different behaviors emerge at high and low

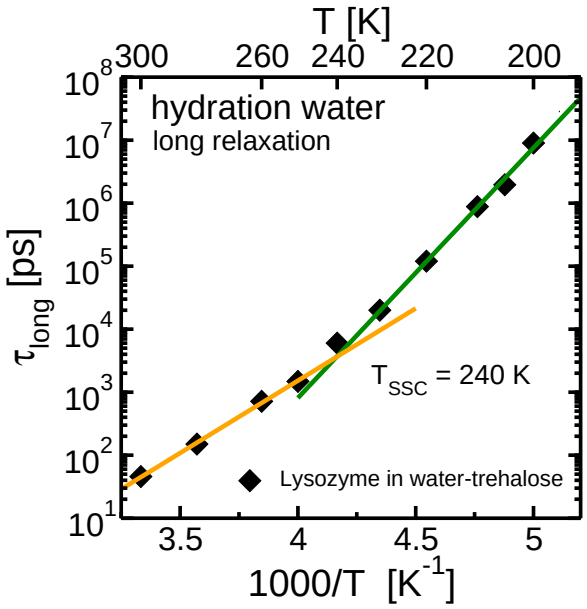

Figure 4.7: Arrhenius plot of the long-relaxation times τ_{long} of hydration water in Lyso(Treha-Aq). Data points fit two Arrhenius laws with different activation energies at high and low temperatures. See table 4.2 for the fitting parameters of the two regimes.

temperatures, similar to what found for the long relaxation of protein hydration water in the Lyso(Aq) system. This two regimes are both linear in this plot, so they can be modeled with an Arrhenius law. We extracted two different values for the activation energy, the high temperature one

is E_A^{HT} = 43.9 kJ/mol and the low temperature is E_A^{LT} = 76.0 kJ/mol. The crossing between this two strong-regimes occur approximately at T_{SSC} = 240 K.

The fitting parameter and the temperature of the strong-strong crossover (SSC) of the long relaxation time are reported also in table 4.2 together with the respective values for the Lyso(Aq) system to better compare them.

The long relaxation time of lysozyme hydration water in the present system has therefore a very similar behavior to that in the Lyso(Aq) system, showing a strong-to-strong crossover whose temperature is unaffected by the presence of trehalose, different to the α-process that retains the phenomenology of the fragile-strong regime but with a shifted temperature crossover T_{FSC}.

We note that upon cooling the system, hydration water in both Lyso (Treha-Aq) and Lyso(Aq) systems crosses from a regime characterized by a lower activation energy to a regime characterized by a higher activation energy. This suggest that the nature of the long relaxation is the same. Besides the absolute value of activation energies are increased by trehalose both above and below the SSC. This fact is plausibly connected to the lower mobility of the protein trapped in the cage of trehalose and consequently of its hydration water.

According to our interpretation in Lyso(Aq), the long process that is peculiar of hydration water only arises from the dynamical coupling between the protein and its hydration layers. In that system we succeeded to link this process to the dynamic transition that hydrated proteins undergo in the supercooled regime through the observation that it occurs in coincidence with the SSC.

Consequently the next step was to look for the PDT of the lysozyme immersed in the cryoprotectant solution. We therefore calculated the mean square fluctuation of hydrogen atoms of lysozyme in the Lyso (Treha-Aq) system and plot the results as a function of temperature in Figure 4.8. In the same figure are also reported the MSF of lysozyme in the Lyso(Aq) system.

Trehalose strongly suppresses the fluctuation of proteins and this plausibly protects the protein from low temperature damage [130]. Nevertheless we also note that also in presence of trehalose, the lysozyme MSF changes the linear slope. The linear fit to the low temperature points and the linear fit to the high temperature points cross at about T_{PDT} = 240 K. The PDT of the lysozyme protein seems to occur at the same temperature in the two systems not depending on the presence of trehalose.

In summary, neither the location of the dynamic transition of τ_{long} (T_{SSC}) nor the protein dynamical transition of lysozyme (T_{PDT}) is significantly affected by trehalose, at lest at our concentration, 40 % wt. To

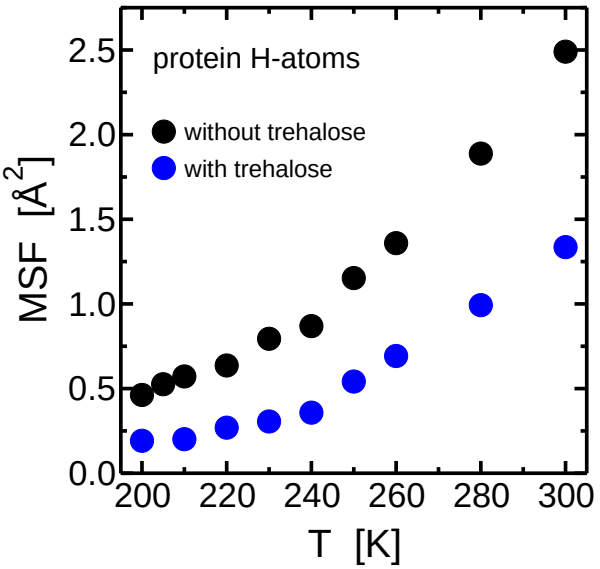

Figure 4.8: Protein dynamical transition of lysozyme in trehalose-water solution as detected from the mean square fluctuation of lysozyme hydrogen atoms.

this it also follows that SSC of the long process of hydration water in Lyso(Treha-Aq) occurs in coincidence with the dynamical crossover of the dynamics of the protein: $T_{SSC} \sim T_{PDT}$. We can therefore conclude that the internal dynamics of the protein and the hydration water remain coupled through the long process also in presence of trehalose.

4.2.2. Water mean square displacement inside the protein hydration shell

For better comprehension of water particle evolution inside the hydration shell of lysozyme, an analysis of the Mean Squared Displacement (MSD) has been done. This is somehow complementary to the information obtained through the single-particle density auto-correlation functions because it provides information also on the length-scale typical of the motion.

We first calculated the MSD defined in Eq. 2.42 for the oxygen atom of water molecules in the bulk system. Figure 4.9(a) shows the resulting $< \Delta r^2(t) >$ for different temperatures in the range of the simulated temperatures 300−195 K in a log-log plot.

It is evident also from this quantity that the dynamics of supercooled water is dominated by the cage effect. At very short times, the MSD of water displays the initial ballistic regime, proportional to t^2, inside the cage formed by water first neighbors molecules. This motion corresponds

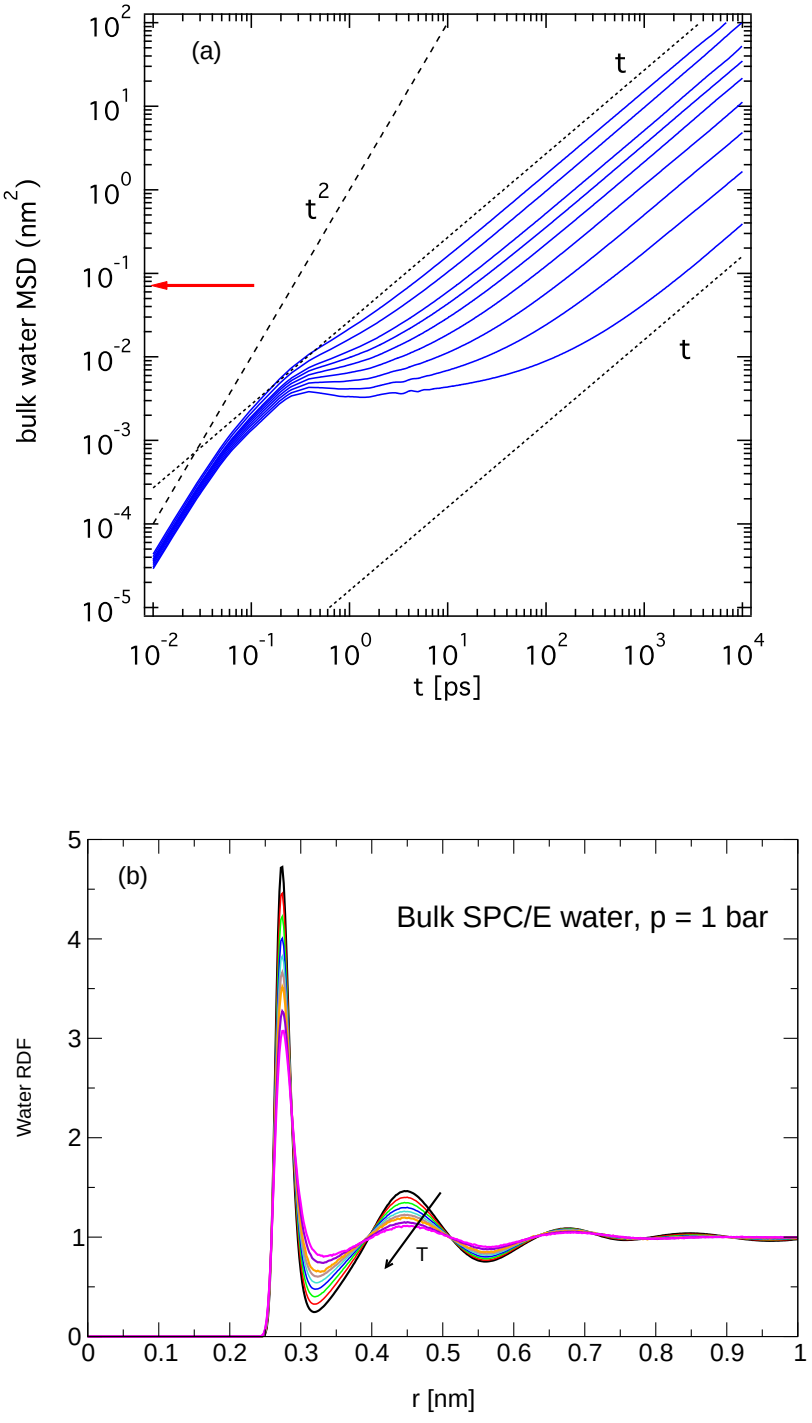

Figure 4.9: Panel (a): MSD of bulk water oxygen atoms as a function of time. Temperature from top are $T = 300$, 280, 260, 250, 240, 230, 220, 210 and 200 K. Dashed and dotted lines are guides for eyes which evidence the short time and long time behavior of the MSD. Panel (b): water oxygen-oxygen RDF of water shown at the same temperatures of panel (a).

to the fast Gaussian relaxation of SISFs. At the lowest temperatures, before entering the diffusion Brownian regime proportional to t, the curves develop a plateau region at about $t = 0.25$ ps. The extension in time of this intermediate regime, which matches the correspondent intermediate plateau region of the SISFs, strongly depends on temperature. This behavior indicates that the particle dynamics is essentially frozen during this lapse of time. To realize what characteristic spatial scale is the one of the plateau, it is helpful to look at the Radial Distribution Function (RDF) of bulk water shown in Figure 4.9(b). The first peak of the oxygen-oxygen RDF, which indicates the mean distance of the first neighbor, is located at about $r_{nn} = 0.275$ nm for all the temperatures investigated. The correspondent square value is indicated in the MSD plot (panel (a)) with an arrow. The water molecules is thus frozen, trapped in a region of space delimited by its first neighbor water molecules, i.e. the particle is within the cage.

We calculated the MSD of lysozyme hydration water both in Lyso(Aq) and in Lyso(Treha-Aq). In Figure 4.10 the MSD of water around the protein is shown for the simulated temperatures in the 200−300 K range.

The curves calculated for hydration water show the cage effect, analogously to bulk water: the t^2 trend at short time is followed by a temporal window where high temperature MSD curves display a linear trend in the log-log plot, while lower temperature curves display a plateau. The latter curves eventually reach the linear trend at times longer and longer upon decreasing temperature. The linear trend at long time differs from that of bulk water. We performed a fit via the functional form:

$$< \Delta r^2(t) > \sim t^n \tag{4.1}$$

on the highest temperature ($T = 300$ K) MSD curves of protein hydration. For $n = 1$, Eq. (4.1) becomes the usual Brownian dependence $r \sim t$. We found $n = 0.73$ for the protein hydration water in Lyso(Aq) system and $n = 0.61$ for the protein hydration water in Lyso(Treha-Aq). The found power behavior are reported in Figure 4.10 as guides for eyes.

The mean-square displacement of the interfacial water shows therefore sub-diffusivity for all the temperatures investigated. This can be due to hydrogen bonding with the protein and also with the trehalose in the hydration shell of the protein, that can hinder water motion. Sub-diffusivity has been observed by Bizzarri et al. [147] in the hydration water of plastocyanin, a copper-containing protein involved in electron-transfer, and, more in general, in hydration water of other bio-macromolecules, like lipid and cell membranes [157, 158].

Finally in Figure 4.11 we report the MSD of bulk water and hydration water at the lowest temperatures. This Figure resembles the Lamb-Mössbauer factor $A(q)$ of the SISFs (see the plateau values in Figure 4.3).

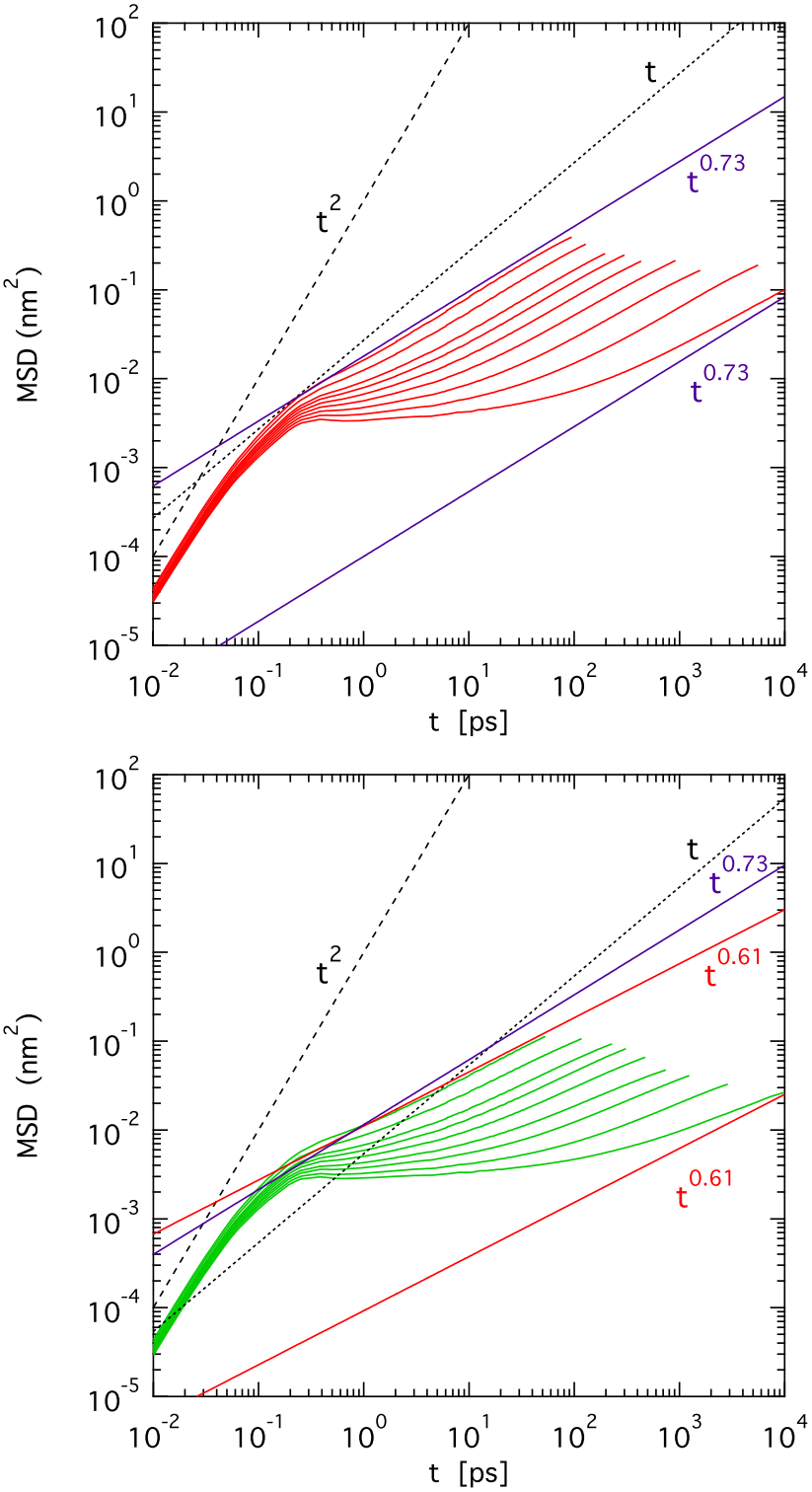

Figure 4.10: MSD of protein hydration water in Lyso(Aq) (upper panel) and Lyso(Treha-Aq) (lower panel). In each panel temperatures span from T = 300 K (top curve) to T = 200 K (bottom curve).

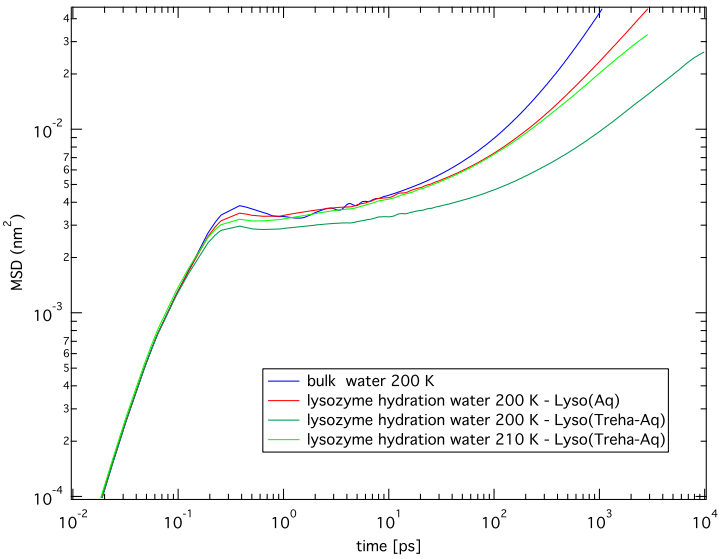

Figure 4.11: MSD of bulk water and hydration water is compared at low temperature.

At 200 K the plateau of SISF and MSD coincides in bulk and hydration water of Lyso.

4.2.3. Structural characterization of the cryoprotectant solution

The structure of a cryoprotectant solution, to be intended how the water and disaccharide molecules organize around the biomolecules, seems to be intimately related to the bio-protection ability of disaccharides. As a matter of fact, the first hypothesis on the mechanism of bio-protection were based on different spatial organization of those solvent molecules around the macromolecule to be cryo-protected.

In a previous work of our research group [121], the structural characterization of the system Lyso(Treha-Aq) was done by looking at the RDF of the water around the lysozyme. In the narrow range of temperature studied in that work, 300–260 K, a progressive depletion of trehalose upon decreasing temperature was observed near the protein surface. We now have investigated what happens when the temperature is ulteriorly decreased down to 200 K.

Figures 4.12 and 4.13 display the RDF of water around the lysozyme at all the temperature simulated in this work. Note that data relative to temperatures $T = 300, 280, 260$ are the same of Ref. [121].

The RDFs of water around the protein have been calculated as pair correlation functions between the oxygen atom of water molecules and the centre of mass (COM) of the lysozyme, we indicate them in text as "Lyso (COM) - OW" RDFs. In each panel of both the Figures are also

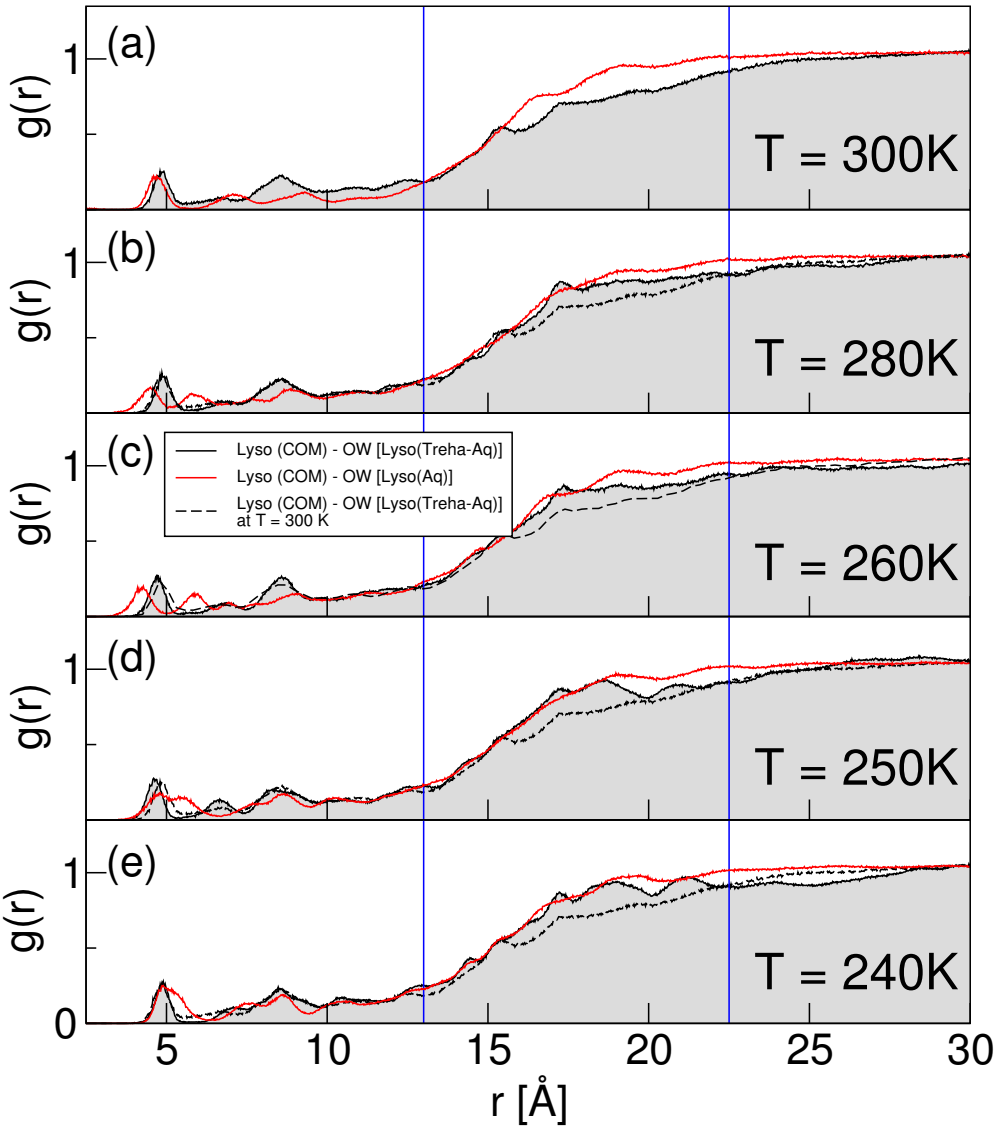

Figure 4.12: Radial Distribution Function (RDF) RDF of water around the lysozyme at different investigated temperatures. RDFs of water around the centre of mass (COM) of the lysozyme in the Lyso(Treha-Aq) system, (black lines with gray shading to baseline) and in the Lyso(Aq) system (red continuos lines). The RDF at $T = 300$ K for Lyso(Treha-Aq) is also reported in all panels (dashed black line) for comparison. The blue vertical lines mark the minor (13 Å) and major semi-axes (22.5 Å) of the lysozyme.

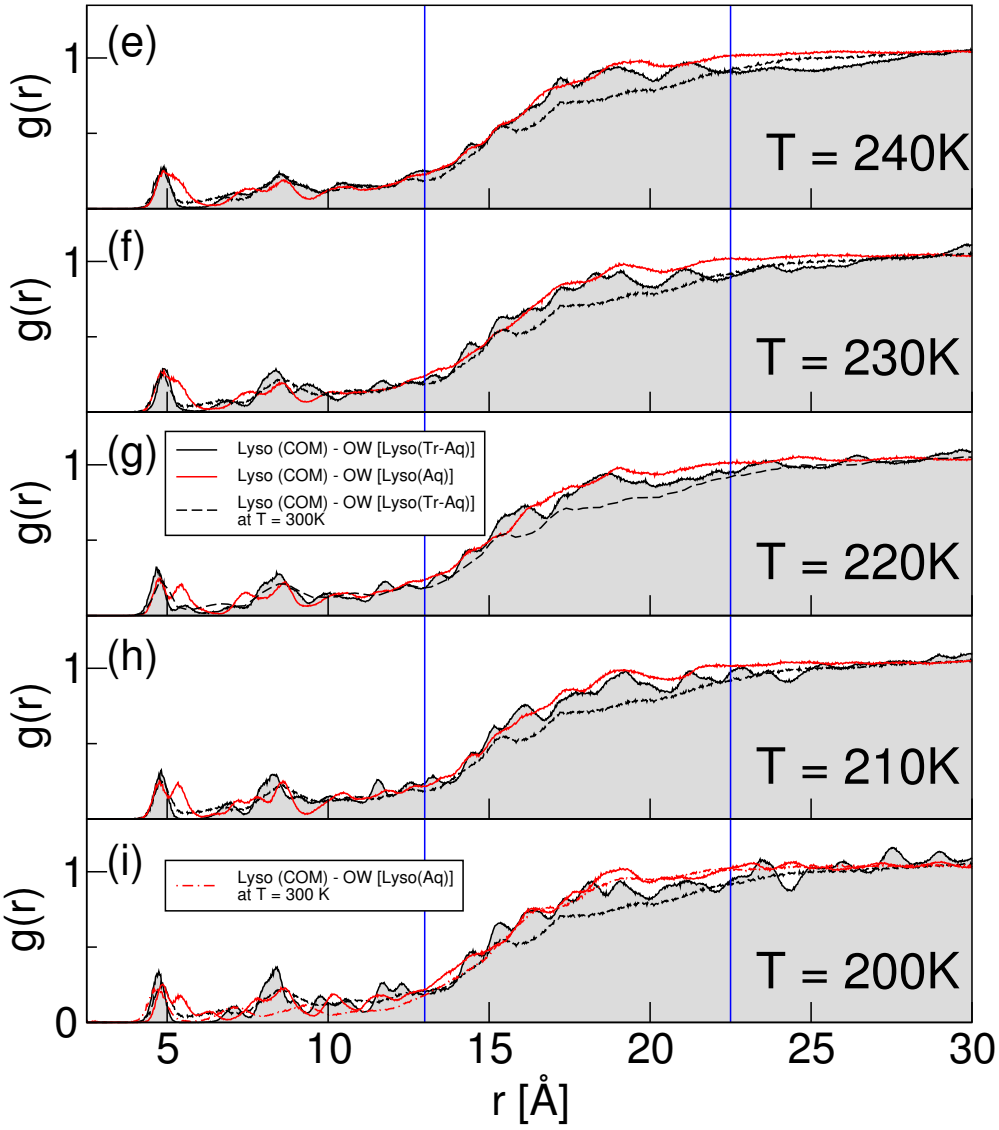

Figure 4.13: Radial Distribution Function (RDF) RDF of water around the lysozyme at different investigated temperatures. RDFs of water around the centre of mass (COM) of the lysozyme in the Lyso(Treha-Aq) system, (black lines with gray shading to baseline) and in the Lyso(Aq) system (red continuos lines). The RDF at $T = 300$ K for Lyso(Treha-Aq) is also reported in all panels (dashed black line) and the RDF at $T = 300$ K for Lyso(Aq) is reported in panel (i) (point dashed red line) for comparison. The blue vertical lines mark the minor (13 Å) and major semi-axes (22.5 Å) of the lysozyme. Note that panel (e) is the same panel (e) of Figure 4.12.

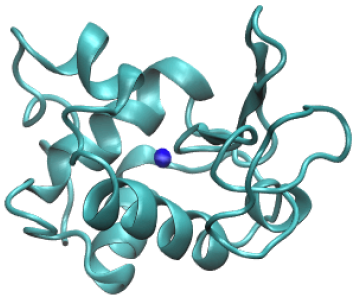

Figure 4.14: The lysozyme center of mass is indicated with a blue sphere. Lysozyme is depicted according to its tertiary structure. This configuration is taken from the simulation at $T = 300$ K.

reported, for sake of comparison, the "Lyso (COM) - OW" RDF calculated in Lyso(Aq) at the indicated temperature and, for reference, also the "Lyso (COM) - OW" RDF in Lyso(Treha-Aq) calculated at $T = 300$ K.

Geometrically the lysozyme has an ellipsoidal shape. Thus it can be approximated as a prolate ellipsoid, with a pair of equal semi-axes a and a distinct third semi-axis c, with dimensions $a = 13.0$ Å and $c = 22.5$ Å [159]. These two characteristic distances are marked in the plots, which are consequently divided in three regions of space.

The first region corresponds to the space between the COM of the protein and the smaller semi-axes. Here, no water molecules are found up to ~ 3 Å in both the systems, due to the fact that this space is excluded by the presence of the protein itself. From the first peak located in Lyso(Treha-Aq) at ~ 5 Å, several water molecules are found. The behavior in Lyso(Aq) is similar, but the first peak moves in temperature, showing that water molecules are more mobile when trehalose is absent. The water molecules inside this regions are those that penetrate deep inside the protein. It must be noted that in fact lysozyme is formed by two domains that form two lobes. Between these two lobes, there is a cleft which deepens into a cavity of about 6-8 Å in diameter [160]. Lysozyme is depicted in Figure 4.14. The COM of lysozyme is located inside this cleft, approximately on the internal surface of the cavity. The fact that we found water deep in the protein has been also checked at visual inspection of the simulation box. The cavity is filled with water molecules.

The RDFs start to increase at a distance corresponding to the first semi-axis, up to a distance corresponding to the longer semi-axis. Beyond this point, RDFs become approximately constant. This happens in both the systems.

Upon cooling the RDFs in Lyso(Aq) do not show significant modification and they actually coincides beyond the the first semi-axis event at

the lowest temperature (see Figure 4.14(i)), showing no significant modulation with the distance from the protein. The situation is different in presence of trehalose molecules: upon cooling the system, the RDFs in Lyso(Treha-Aq) increase in the intermediate region meaning that the water content in the close vicinity of the protein is growing upon cooling. Besides, those RDFs are more corrugated already at high temperature with respect to RDFs in Lyso(Aq) and upon cooling become more and more corrugated, showing several peaks even at distances beyond the second longer semi-axis.

The developing of peaks upon cooling can be due to the structuring of trehalose in the solutions.

Complementary to information given by the RDFs are the density profiles of trehalose molecules around the protein. In Figure 4.15 density profiles of trehalose COM around lysozyme COM are plotted for temperature in the range 300−200 K. These Figures show in the region corresponding to the first semi-axis and up to ~ 15 Å, a first peak, that split into a doublet at some temperature, indicating that the density of trehalose is approximately equal to its average value at long distances. This information was missing in the water RDFs. These features are then followed by a depletion region of ~ 2 Å and then a region where the density of trehalose is higher than average. This is clearly visible at higher temperature where this region extend from ~ 17 Å to ~ 27 Å. Upon cooling the system the curves become much corrugated in general, specially at long distances. In the intermediated region the density profiles keep showing peaks of density excess.

To better characterise the distribution of trehalose molecules around the lysozyme, we calculate the trehalose number density as a function of its distance from the protein surface. This quantity can be much indicative of what is the ordering of trehalose on the lysozyme surface, because this calculation does not assume spherical symmetry in respect to the RDFs. Number density of trehalose as a function of the distance from the closest protein atom are plotted in Figure 4.16 for the same temperature shown in Figure 4.15.

The curves all show a first peak at ~ 4 Å with a width of ~ 2 Å. For temperatures down to 250 K a wide depletion region appears at intermediate distances where on average lie less trehalose molecules. For temperature below 250 K after the first peak the curves show alternating regions at higher and lower number density toward the greater distance region.

From these Figures, the crowding of trehalose molecules on the surface of the lysozyme is clearly revealed by the first peak of the curves. The red curve indicated $r = 6$ Å, the distance that we used for the definition of hydration water. We can see that the first peak is located inside the 6

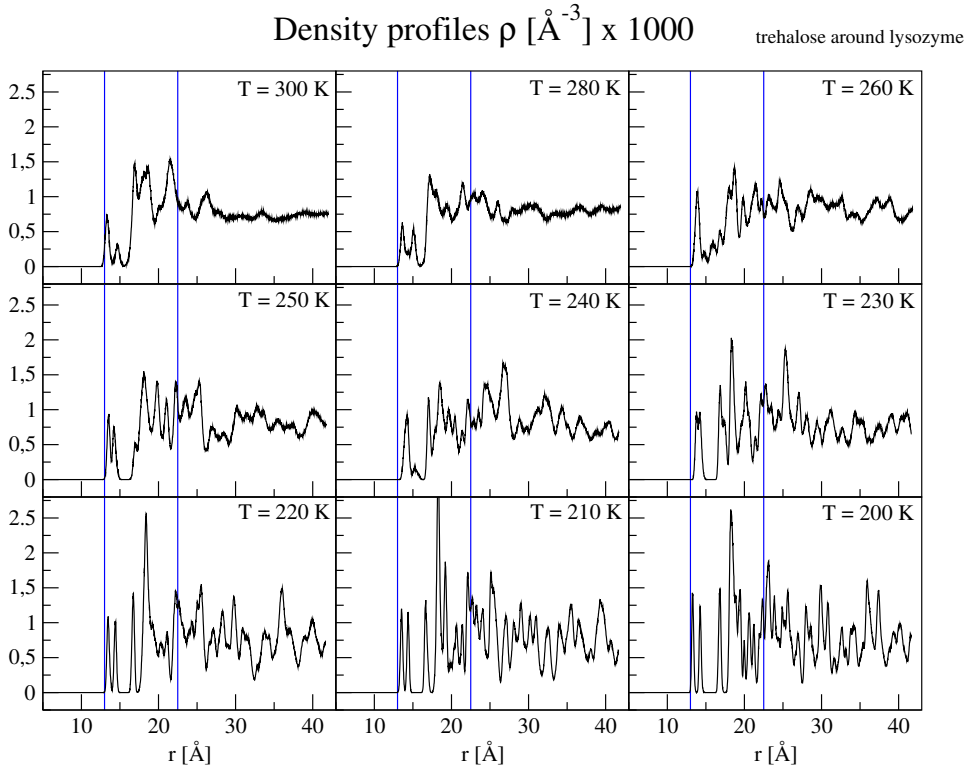

Figure 4.15: Density profile of the COM of trehalose molecules around the COM of the lysozyme shown at different temperatures. The blue vertical lines mark the minor (13 Å) and major semi-axes (22.5 Å) of the lysozyme.

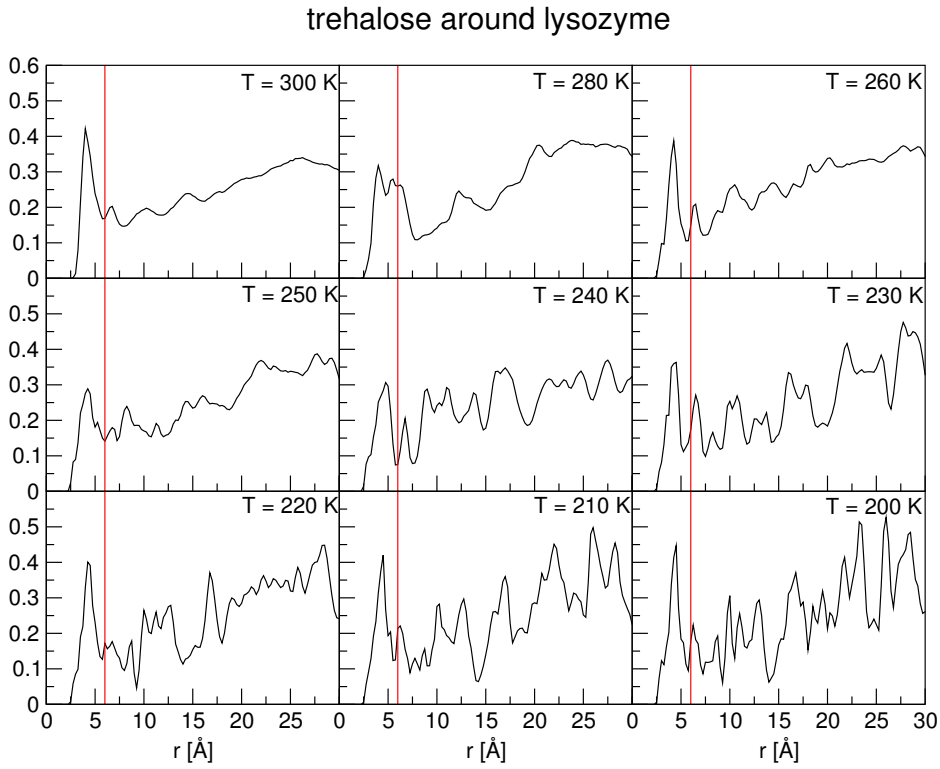

Figure 4.16: Number density profile of trehalose as a function of the distance between trehalose COM and the closest protein atom. The red vertical line marks the distance r =6 Å from the surface of the lysozyme, used in the definition of hydration water for the analysis of dynamical results.

Å-thick hydration shell of lysozyme, and indeed the first local minimum of the number densities, found beyond the first peak, occurs proper at 6 Å. This is true at each temperature, with the exclusion of $T = 280$ K where the peak at the surface of lysozyme appear broader.

Our findings prompt an important observation: when lysozyme is immersed in the cryoprotectant solution, trehalose is not completely excluded from the region closest to the protein. These molecules actually form a cage surrounding the protein. Between the protein and this cage, water molecules are nevertheless found on average (by looking at water RDFs) so that the protein is kept hydrated even at low temperature. Plausibly the trehalose molecules found in the hydration shell of lysozyme are those that most slow the hydration water dynamics and thus inhibits the crystal formation that damages biomaterial at low temperature.

4.2.4. Hydrogen Bonding in the lysozyme hydration shell

In this Subsection we present the characterization of the hydrogen bonding behavior of the water molecules inside the 6 Å-thick shell around the lysozyme in both system Lyso(Aq) and Lyso(Treha-Aq). We also compare those results with the one obtained in the bulk water system.

We have already said in the Subsec. 2.3.2 that we adopt a geometry criterion for the definition of a HB between two water molecules. Two water molecules are hydrogen bonded if the distance between their oxygen atoms is less than 3.5 Å and the angle H−O···O is less than or equal to 30°. For the calculation of water HBs in the bulk, all the water molecules of the simulation box have been analyzed. For the water HBs in the hydration shell of lysozyme, only water molecules inside this region of space are considered in the calculation of the quantity presented in this Subsection, but the search for HBs has been run also to water molecules of outer hydration shell. This is done because most of the water molecules at the outer surface of the hydration shell have first neighbors water molecules that are not inside the 6 Å shell. Without this care, many HB candidate molecules would be excluded.

In Figure 4.17 we report the percentage of the analyzed water population that form n HBs with another water molecule. Data for $n > 7$ are not reported because no molecules form those number of HBs.

In the first panel of this Figure we report data calculated for bulk water. Each curve is calculated at a different temperature spanning 300−200 K. At high temperature most of water molecules are involved in four or three HBs. Upon cooling the hydrogen bonding behavior of bulk water is enhanced, with a growing water population accepting four hydrogen bonds whereas a decreasing fraction of water accepts other n values of HBs. Correspondently the distribution shows the sharp peak at $n = 4$. This is the typical, known, behavior of hydrogen bonding in water.

In the middle panel of Figure 4.17 are presented the results relative to lysozyme hydration water in the Lyso(Aq) system. It is clear that water at the protein interface has a different HBs distribution. At high temperature the distribution appears shifted toward lower n values and wider with respect to bulk water, with water forming mostly a total of three or two HBs. Note that nevertheless the population of water forming one or four HBs is comparable to each other. Upon cooling, the behavior resembles the one of bulk water and we observe the tendency of water molecules to form four HBs. Thus the population involved in four HBs increases, but at the only expense of the fraction forming one and two HBs, the population involved in three HBs is in in fact approximately stable in temperature and correspond to highest peak also at low temperature. The fact that the hydration water forms on average less than

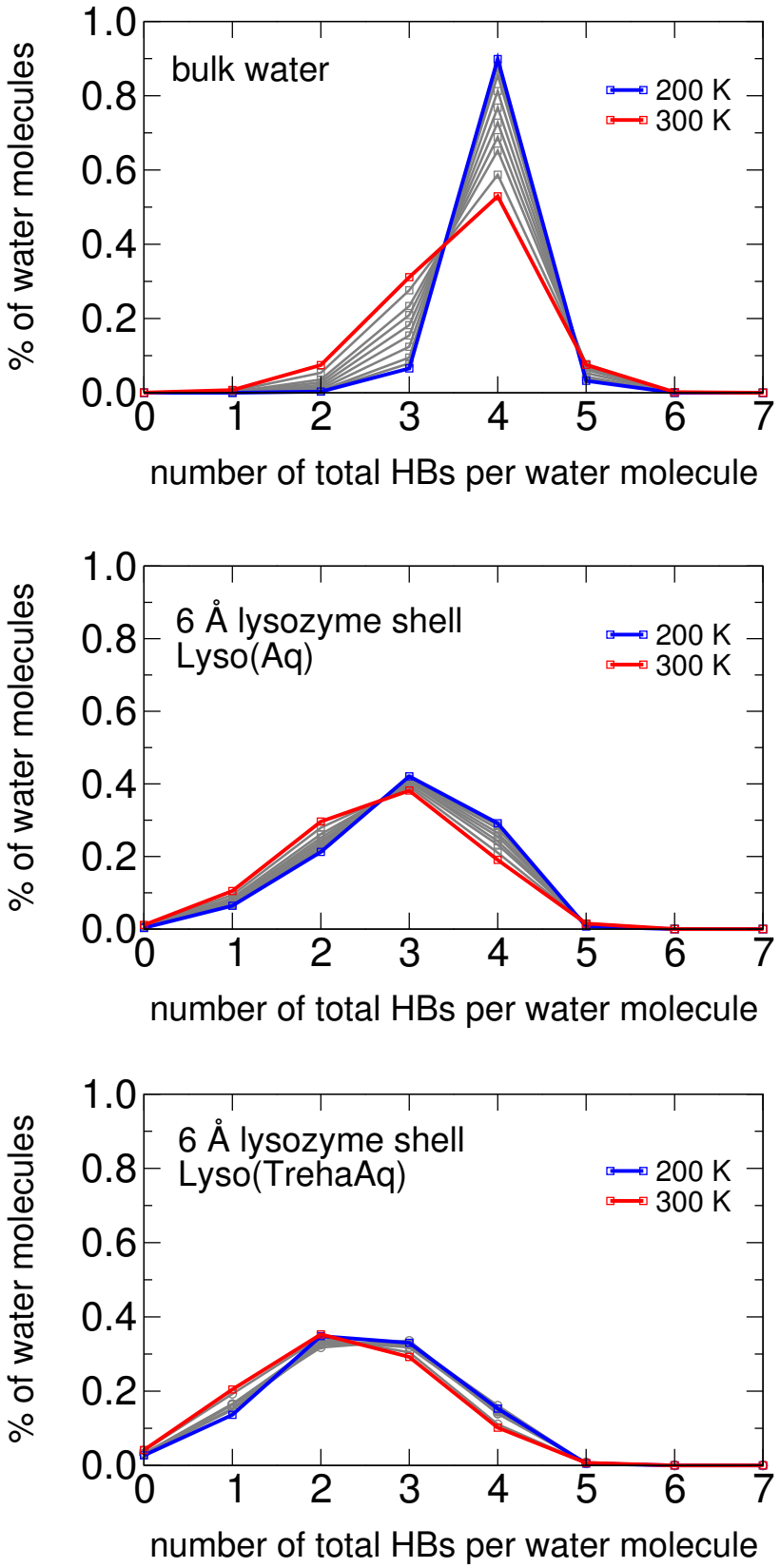

Figure 4.17: Distributions of the number of hydrogen bonds formed per water molecule in bulk water (top) and in the lysozyme hydration shell in Lyso(Aq) (middle) and Lyso(Treha-Aq) (bottom). Different curves correspond to different temperatures.

four HBs with respect to bulk water is not much surprising, because a finite fraction of these hydration water molecules also form HBs with the protein atoms.

The addiction of trehalose molecules in the solution, causes a ulterior diversification in the HBs distribution. This can be seen in the bottom panel of Figure 4.17, that shows the calculated distributions for hydration water in the Lyso(Treha-Aq) system. All the curves are smeared on the interval ranging from $n = 0$ to $n = 5$ similarly to what found in the trehalose free system and no sharp peak is observed in the distribution at any temperature. In general these distributions show less sensitiveness of the temperature of the system. Water molecules shows the tendency to form on average two or three values, approximately with the same probability. Few water molecules succeed in HB-bonding a fourth molecule, differently from the hydration water of the protein in Lyso(Aq). This is plausibly due to the HB-bonding between water and trehalose, which has already pointed out in literature as the "de-structuring effect of trehalose", which is able to form extended hydrogen-bond networks with water [14, 71, 161]. Finally is to be noted the finite population with $n = 0$, these water molecules also include some molecules forming HBs only with the protein and/or with the disaccharides molecules. Effectively the visual inspection of the simulation box reveals clustering phenomena of trehalose molecules on some region of the surface of the protein, with few or none water molecules trapped between.

HB-bonding behavior on bulk and hydration water has also been characterized analyzing the acceptor and donor behavior of the water molecules. Results are shown in Figure 4.18.

The common idea on the acceptor and donor abilities of water is represented by the picture of a water molecule accepting two HBs through the two lone pairs of the oxygen atom and donating other two HBs via the hydrogen atoms. In bulk SPC/E water (top panels), water molecules are effectively found to follow this picture, especially at low temperature, where they are most likely to accept and donate two HBs at the same time. Conversely, lysozyme hydration water in Lyso(Aq) and in Lyso(Treha-Aq) don't show this tendency. See middle and bottom panels of Figure 4.18. Distributions resemble in fact the distribution of total number of HBs, they are wide and spread between $n = 0$ and $n = 3$. At low temperature, in Lyso(Aq) however the greatest population of water molecules is the one accepting and donating two HBs, as in bulk. In Lyso(Treha-Aq) this corresponds to the population accepting and donating one hydrogen bond. The reduction on the number of double donors and acceptors could cause lack of tetrahedrality of the HB network of hydration water.

To deepen the analysis on this last point, and more in general on

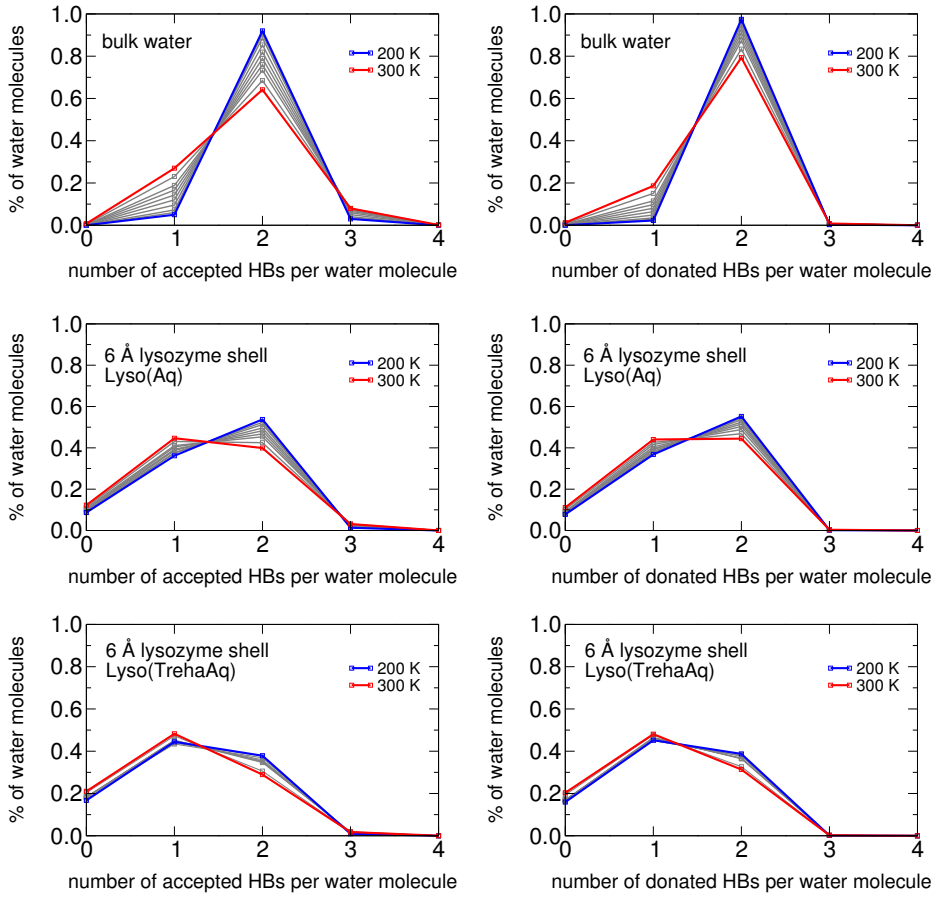

Figure 4.18: Variation in the number of hydrogen bonds accepted (left panels) and donated (right panels) per water molecule as a function of temperature in bulk water (top panels) and in the lysozyme hydration shell in Lyso(Aq) (middle panels) and Lyso(Treha-Aq) (bottom panels).

the properties of HB-network on bulk water and hydration water, we calculated the distribution of the cosine the angle γ between three nearest neighbor water molecules. Consider that the tetrahedral angle is 109.5° and corresponds to $\cos\gamma = -0.334$.

Figure 4.19 shows the temperature dependence of the distribution of $\cos\gamma$ in the three investigated systems, bulk water, lysozyme hydration water in Lyso(Aq) and lysozyme hydration water in Lyso(Treha-Aq). In Figure 4.20 we compare at two selected temperature, $T = 300$ K and $T = 200$ K, the $\cos\gamma$ distribution of the three systems. All the distribution are normalized to unit area to better compare them.

At T = 300 K, the distribution of $\cos\gamma$ in the SPC/E bulk water at any temperature has a well defined peak around 102° ($\cos\gamma = -0.21$),

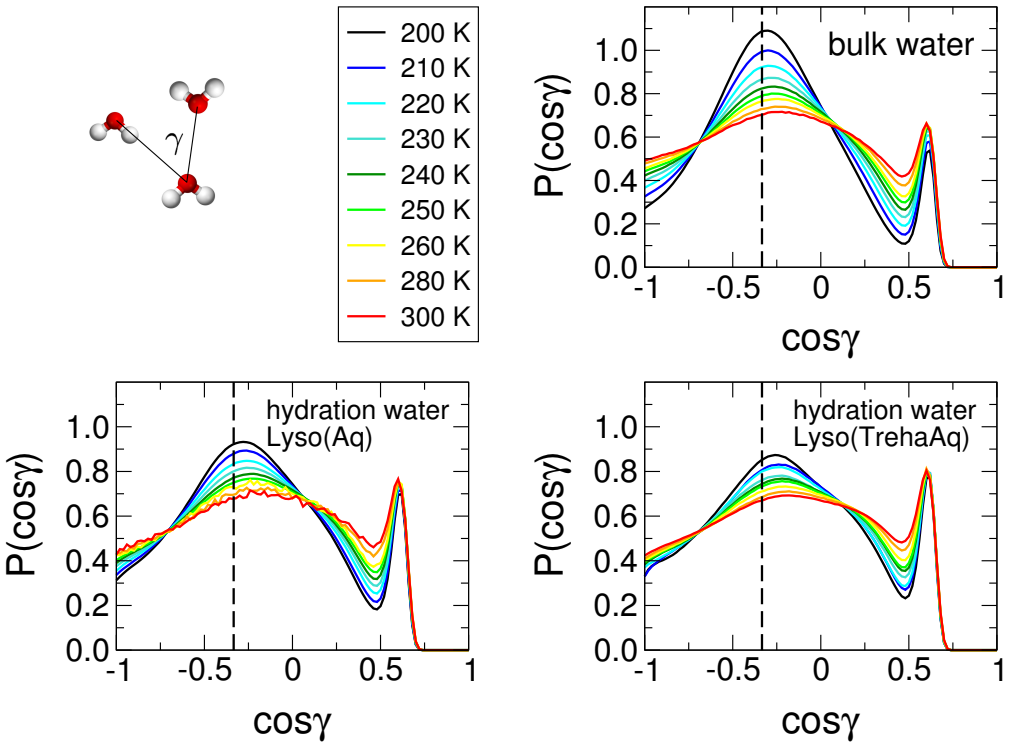

Figure 4.19: Normalized angular distribution function $P(\cos\gamma)$ of the angle between the oxygens of three nearest neighbor water molecules for bulk water (upper panel), for lysozyme hydration water in Lyso(Aq) system (bottom left) and for lysozyme hydration water in the Lyso(Treha-Aq) system (bottom right). In each panel, curves are shown from the highest simulated temperature T = 300 K down to the lowest temperature T = 200 K. Dashed vertical lines mark the cosine value of the tetrahedral angle.

this peak is the signature of the tetrahedral order present in liquid water at short range distance. Upon decreasing temperature this peak becomes sharper and sharper and at T = 200 K it reaches the value $\gamma = 108.8°$ ($\cos\gamma = -0.31$). A secondary sharp peak is found on each curve at $\sim 53°$ ($\cos\gamma = 0.6$), this peak corresponds to interstitial neighbor molecules [111]. Our findings are in agreement with experimental results on water at ambient conditions [162].

The behavior of the $\cos\gamma$ distributions calculated for hydration water is similar to bulk water behavior in both the systems Lyso(Aq) and Lyso(Treha-Aq). At T = 300 K, the distributions coincide showing a broad peak centered $\sim 99.5°$ ($\cos\gamma = -0.167$). At T = 200 K, they show the broad peak at $\sim 105.5°$ ($\cos\gamma = -0.268$) and $\sim 103.5°$ ($\cos\gamma = -0.234$), respectively. The secondary sharp peak is located $\sim 53°$. The position of the latter peak is completely unaffected by neither the enviroment (protein and trehalose molecules) nor the temperature. Differently to bulk water, at low temperature a shoulder on the broad peak located at $\sim 80°$ ($\cos\gamma = 0.160$) is more evident in protein hydration water whereas it is missing in the low temperature distribution of bulk water. Besides this is more defined in the case of hydration water of lysozyme already at high temperature, where the heigh of this shoulder is comparable with the broad peak that signs the tetrahedrality of water. This feature could be associated to a number of water molecules distorted by the protein and by the disaccharides molecules.

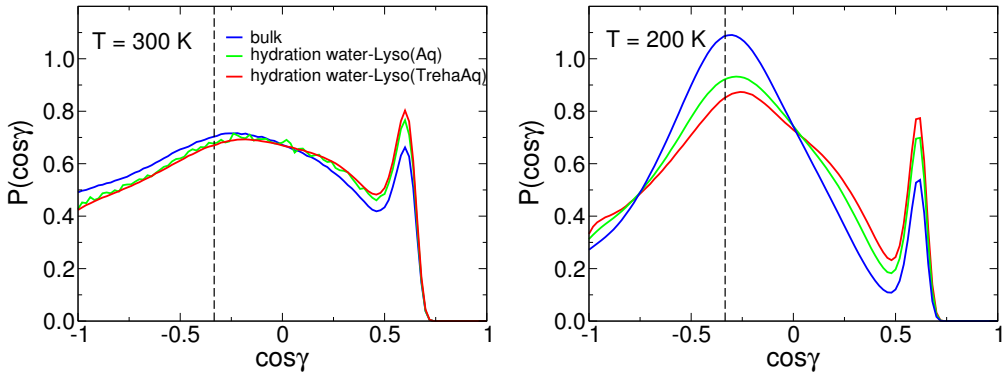

Figure 4.20: Normalized angular distribuition functions $P(\cos\gamma)$ of the angle between the oxygens of three nearest neighbor water molecules are compared between bulk water (blue), for lysozyme hydration water in Lyso(Aq) (red) and in Lyso(Treha-Aq) (green) at the highest simulated temperature T = 300 K (left panel) and at the lowest temperature T = 200 K (right panel). Dashed vertical lines mark the cosine value of the tetrahedral angle.

As a final comment on these distributions, we note that what is changing upon cooling the system is also the relative amplitude between the

tetrahedrality peak, the shoulder and the peak of interstitial water, plausibly associated to different water populations. In that respect we see that the tetrahedrality peak in bulk water is the highest at any temperature, while this is not true for protein hydration water. Three hydration water molecules are therefore less likely to be found at the tetrahedral angle at each temperature with respect to bulk pure water. This is consistent with the averaged lower number of HBs that bonds hydration water with respect to bulk water. Deviation from the tetrahedral angle in water may also lead to the distortion or the disruption of the HB-network. Anyway, we don't have evidences of a great distortion of the hydrogen bond network of hydration water, especially if compared to the angular distribution of water in the hydration layer of Vycor [111].

Globally our findings can be interpreted as a lower tendency of hydration water of forming the typical four-HBs-network. This is because less candidate molecules are found at the right (tetrahedral) angle (as seen from the angular distributions), but also because, reasonable, some water molecules will be hydrogen bonded to both the lysozyme and trehalose molecules, that, from the structural characterization of the solution, we know to crowd inside the region of space here analyzed. This however merits further investigations, and the analysis of inter-species HBs is planned to do.

4.3. Final Discussion and Conclusions

Trehalose in the solution causes a slowing down on the dynamics of hydration water. This is clear from the fact that the density-density correlators decay over much longer time when the lysozyme is immersed in the sugar-water solution than when lysozyme is immersed in water.

The translational dynamics of hydration water can be described by two different relaxations, the α-relaxation and the long-relaxation, which lie on different time-scales. Concerning the comparison with the lysozyme in water, both the processes slow down when trehalose is in the solution. The presence of trehalose induces a major slowing down of the long relaxation (up to three order of magnitude at low temperature) and a mild slowing down of the α one.

The cryoprotector seems to not to affect the phenomenology of α-relaxation in the sense of the fragile to strong crossover of τ_α. The net effect of trehalose on this process is to shift the MCT temperature and consequently the FSC temperature of the lysozyme hydration water to higher value in respect to the Lyso(Aq) (+15 degree) and bulk water (+20 degree). This is also accompanied by a decrease of the activation energies on the strong side of the α process when going from bulk, to Lyso(Aq) and to Lyso(Treha-Aq). This supports the idea that bulk water is a limiting case, placing a lower limit for the value of T_{FSC} and an upper limit for the

activation energy of hopping phenomena in hydration water.

On the connections between FSC and PDT, we highlight the fact that the FSC in hydration water is shifting from the bulk value toward the PDT temperature when trehalose is in the system. According to our definition of hydration water, we find on average 1140 hydration water molecules in within 6 Å from the lysozyme in the Lyso(Aq) system and 710 in the Lyso(Treha-Aq) system. The presence of trehalose molecules at close vicinity of the protein decreases this latter number. The exclusion in the shell of more bulk-like water molecules when going from Lyso(Aq) to Lyso(Treha-Aq) may be the reason of the increase of T_{FSC} toward the value of the PDT. It is important to note that in the case of the monolayer coverage of water on lysozyme, which corresponds to approximately 250 water molecules per lysozyme, the FSC crossover occurs in coincidence with the PDT. In that respect, decreasing the water content is expected to remove bulk water like molecules and presumably the dynamics to be completely coupled/driven by the dynamics of an hydrated protein, which exhibits the PDT. Besides, with the slowing down of the α process the dynamics of hydration water upon decreasing the hydration level can be also accompanied by the degeneracy of the two structural relaxations processes approaching similar time scales. The study of the FSC upon changing the hydration level of the protein will be the subject of next future work.

In both the protein systems, we found that the crossing between the low-temperature Arrhenius regime to the high-temperature Arrhenius regime of the long relaxation time τ_{long} occurs in coincidence with the PDT, therefore the nature of the dynamical crossover of the long relaxation is almost unaffected by the trehalose, i.e. allegedly this relaxation of hydration water remains dynamically coupled with the protein motion also in presence of the sugar. The activation energies are instead increased by trehalose on both the sides, this should quantifies the response of protein fluctuations versus the temperature.

The minor number of water molecules in the lysozyme hydration shell in the Lyso(Treha-Aq) system (about the 62%) is due to the fact that also on average about 40 trehalose molecules lie in the hydration shell (These data have been calculated by integration of our number density). At the visual inspection trehalose molecules appear to cover the protein surface not homogeneously independently of the temperature, moreover in some part of the surface they show clustering of more molecules. This is in accordance to the fact that the about 70% of the lysozyme surface remains hydrated in presence of trehalose and that they form patches over the surface [86]. The fact that trehalose form a cage on the protein surface that however do not exclude completely water can be related to the cryopreserving properties of the solution. In this system the hydration

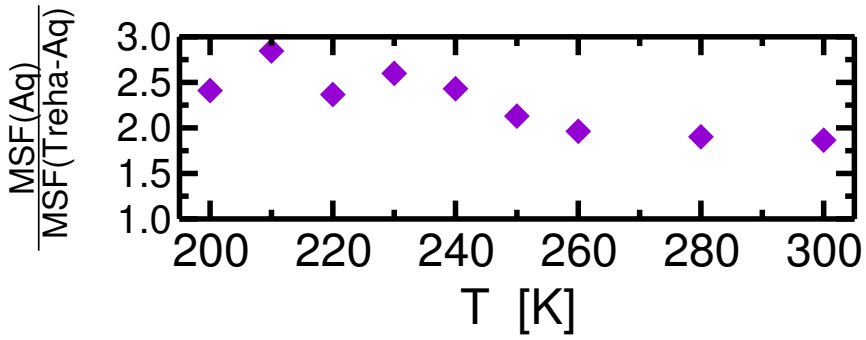

Figure 4.21: Ratio between the lysozyme MSF in Lyso(Aq) and the lysozyme MSF in Lyso(TrehaAq) as a function of the temperature.

shell of lysozyme is in fact composed of water molecules shared between the protein and the sugars near the protein surface, which also offers to water a wider interaction surface. Those sugars presumably cause the great slowing down effect of the dynamics of hydration shell. Finally, it remains to be investigated the dynamics of the sugar cage at the protein interfaces that we plan to do in the next future.

From the protein point of view, the addiction of trehalose in water, at least at the concentration of 40% trehalose, preserves both the protein dynamical transition itself and the temperature at which it occurs. The dependence on the sugar concentration of the PDT has been studied in [163] on lysozyme in glucose-water solutions and at least at diluted samples ($>$ 0.6 w(water)/w(sugar)[1]) this seems to show no statistically significant correlation with the concentration of the sugar. The protein dynamical transition is closely related to the low temperature activation of the protein and therefore to its functioning. The clustering of sugar also stiffens the local protein environment and consequently the protein is dumped in its structure fluctuations, see Figure 4.21 of a factor that reaches ~ 2.5 at low temperature. This can positively affect the stability of the protein [164] at low temperature. In this respect the bio-protection of the cryoprotectant solution seems to act almost exclusively from the dynamical point of view rather then from the thermodynamic one.

[1] Our solution is $\sim$ 1.5 w(water)/w(sugar)

5

The glass forming $LiCl{:}6H_2O$

In this Chapter the results obtained for the set of simulations at 1 bar isobar of a glass-forming solutionare presented. The solution is composed of lithium chloride and water with the electrolyte mass fraction $\phi = 0.14$. To the best of our knowledge, this is the first simulation of this system as described by the JC-TIP4P/2005 potential extended in the supercooled regime. The Chapter deals with the the dynamics of water and with the structural properties of the system. We start presenting the system.

5.1. Introduction

Since the freezing point of water can be lowered by the addition of salt, the study of electrolyte solutions upon dilution is a valuable route to extrapolate the water behavior in the no-man's land and, consequently, to explain anomalies of water. The simulations of Corradini and Gallo [165] showed that the TMD and the second critical point is present in the limits of low salt concentrations.

Lithium chloride solutions can play a paramount role in this direction because of the ease of supercooling. Moran [166], in fact in 1956 while studying the (stable) phase diagram of binary LiCl-H_2O was complaining that:

> *"Supercooling caused a great deal of trouble through its persistence over a large temperature drop, although vigorous efforts were make to induce crystallization."*

Probably, at that time, he could not imagine how much the property of the aqueous lithium chloride that he was complaining with, would have been appreciated in the years to come by the scientific community.

Figure 5.1(a) shows the phase diagram of the solutions LiCl:RH$_2$O, where R is the water-salt molar mass ratio. The system has four crystalline hydrates with $R = 1, 2, 3$ and 5. The eutectic point at 1 bar is located at temperature $T_e = 199$ K. Upon cooling the eutectic liquid, at the concentration $R_e \sim 7$, one obtains ice Ih in micro-crystals coexisting with the penta-hydrates.

More interesting to our field of research is the metastable phase diagram of LiCl-H$_2$O solutions, that has been studied since 1956 [166, 167]. This is shown in Figure 5.1(b). Dotted points represent the (calorimetric) glass transition temperatures of the solutions. In the phase diagram it is also reported the line of crystallization of ice, of the penta-hydrate and of the tri-hydrate upon cooling. Near the eutectic concentration, at concentration $R \sim 6$, there it opens a channel through which the liquid can be supercooled directly to the glass transition, without thermic or kinetics phenomena hampering it. Successive works showed that the extension of this channel can be varied from R = 4 to R = 7 [168], by changing the cooling rate of the solutions.

The LiCl:6H$_2$O is therefore a glass-forming liquid with a glass transition temperature of T_g =135 K, with the peculiarity of avoiding crystallization.

The LiCl:6H$_2$O has been intensively studied. The predictions of simple scaling for the α-relaxation and of identical scaling behavior for mechanical and electrical susceptibilities provided partial evidence for the validity of the approach of MCT in the glass transition problem. The imaginary part of the compressibility modulus shows in fact power-law behavior on both sides of the α-peak in frequency domain but the characteristic relaxation times obtained from the scaling of the moduli are better described with a Vogel-Tammann-Fulcher law since data show deviation from the MCT power law ($T_{MCT} = 164$ K, $\gamma = 4.25$) about 40 degree above the glass transition temperature [170, 171]. Successive QENS experiments [172], show a crossover in the average relaxation times on the nanosecond time scale at about 220 K, this crossover was of the type fragile-to-strong. This crossover was then questioned by the same author, demonstrating the emergence of the so-called excess wing in the high frequency tail of the structural relaxation α-peak [173]. Concerning the low frequency phonons analysis, it must be noted that LiCl:6H$_2$O has a behavior similar to what is expected for supercooled water at least down to ~ 210 K [174]. Finally, the dynamic structure factor of the supercooled solution has been wide-band characterized by the joint analysis of photon correlation spectroscopy, BLS, IUVS and IXS spectra. This investigation [175, 176], has revealed the onset of the typical structural α-relaxation of the solution and the onset of the secondary Johari-Goldstein β-relaxation. Interestingly this latter onset upon cooling at $T \sim 220$ K, in coincidence with

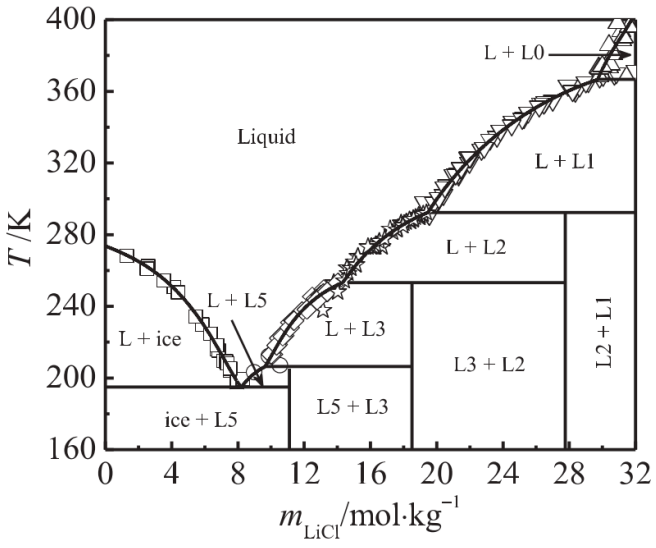

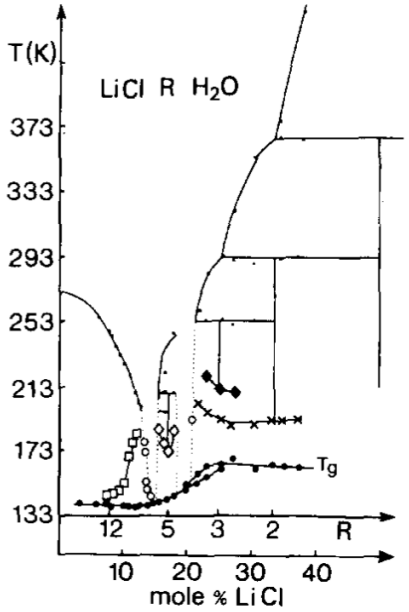

Fig. 7. Metastable phase diagram of LiCl H_2O (see text). Values for T_g(●), crystallization of ice (□), of LiCl $5H_2O$ (◇), of LiCl $3H_2O$ (◆), and of LiCl $2H_2O$ (×) are quoted. The dashed lines were obtained as described in the paper.

Figure 5.1: Stable (a) and metastable (b) Phase-diagrams of LiCl-H_2O solutions at 1 bar. Figures from Ref. [169] and Ref. [166], respectively.

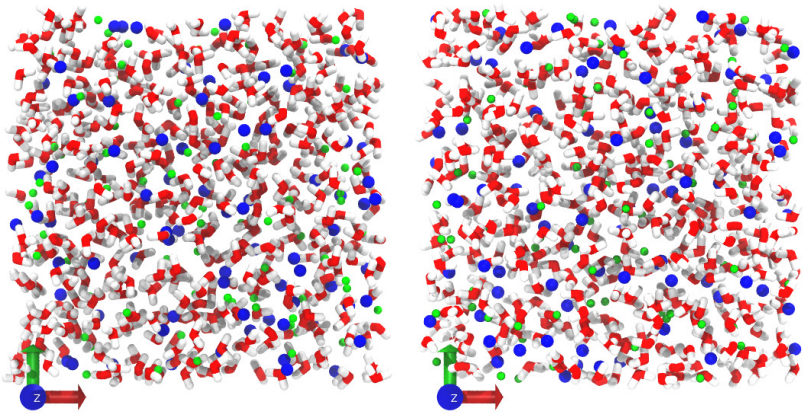

Figure 5.2: Box at T = 300 K and T = 200 K.

the temperature range at which the properties of water seem to diverge. On the other hand, the α-relaxation has a fragile character down to the glass transition.

5.2. Simulation Details

All-atoms MD simulations on the LiCl:6H_2O system were performed at constant pressure $p = 1$ bar and temperatures spanning from $T = 300$ K down to $T = 185$ K. The cubic simulation box ($L = 2.61$ nm at $T = 300$ K) contains 480 water molecules described by the TIP4P/2005 potential, 80 Cl^- ions and 80 Li^+ ions described by JC-TIP4P/2005 [101]. These force fields, have been exposed in the Subsec. 2.2.3.

The cutoff radius for the non-bonded van der Waals interactions was set to 9.5 Å. The Coulombic interaction was truncated at 9.5 Å, and the correction contribution was evaluated by using the Particle Mesh Ewald method. The equations of motion are integrated with a time step of 1 fs with the Verlet leap-frog algorithm. Berendsen method [93] was used to handle both the temperature and the pressure of the system. The MD simulations were performed using the parallelized version of GROMACS 4.5.5 [91] simulation package.

Table 5.A shows the summary of the thermodynamic points investigated in this work. Details include the density of the system ρ, the potential energy U and simulation time for equilibration and production runs. At low temperature we also run two annealing cycles, not reported in the table, comprehending a fast heating to 300 K followed by equilibration to 185K. Both the independent cycles reach the same potential energy average value within it fluctuations.

The total computational time amounts to about 1680 ns for the entire simulated isobar. The simulations were carried out on the INFN-Grid

Roma Tre cluster[1] where we achieved an average simulation times of 98 ns/day.

Table 5.A: Summary of the simulated state points at $p = 1$ bar including the temperature T, density ρ and potential energy U of the LiCl:6H_2O system. At each temperature the equilibration run of length t_{eq} is followed by the data collection for a time t_{prod}.

T (K)	ρ (g/cm^3)	U (kJ/mol)	t_{eq} (ns)	t_{prod} (ns)
300	1.777	-288531	40	30
290	1.781	-312829	60	20
280	1.787	-312829	60	20
270	1.793	-312829	100	20
260	1.797	-337058	60	20
250	1.800	-349416	60	20
240	1.803	-361738	60	40
230	1.803	-374200	60	40
220	1.806	-386309	120	40
210	1.813	-398196	120	40
205	1.825	-404481	120	40
200	1.804	-409764	120	40

Two cubic simulation boxes at the highest and lowest simulated temperature are shown in Figure 5.2.

5.3. Results

5.3.1. Water Self-Intermediate Scattering Functions

We characterized the density fluctuations of water in the supercooled solution by looking at the oxygen SISFs. The curves calculated at the peak of the oxygen-oxygen structure factor of water $q = 2.25$ Å^{-1} are shown in Figure 5.3 for all the twelve simulated temperatures that span from $T = 300$ K down to $T = 200$ K.

The SISFs of the water contained in the solution show upon cooling similar behavior to the SISFs of bulk water. As predicted by mode coupling theory, a two step relaxation scenario is observed as supercooling proceeds. The dynamics is however slower than pure bulk water, as the second step of the relaxation, the α-relaxation bump, is visible already at the highest temperatures. It is a general finding that popular water models like SPC/E, TIP4P, TIP4P/2005, do not show the α-relaxation bump already at $T = 300$ K. The boson peak - overshoot feature it is also observed for temperatures lower than 250 K.

[1] http://web-cluster.fis.uniroma3.it/

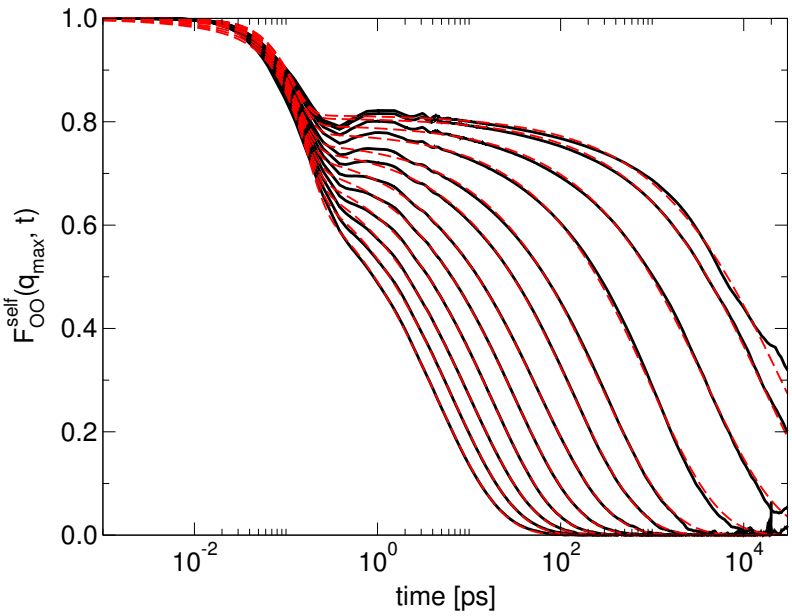

Figure 5.3: Oxygen-oxygen SISFs in LiCl:6H_2O. The bottom curve correspond to the temperature $T = 300$ K, the top curve correspond to $T = 200$ K. q is fixed at 2.25 Å^{-1}.

The overall curves can be fitted with the formula:

$$F_s(q,t) = [1 - f(q)]e^{-(t/\tau_s)^2} + f(q)e^{-(t/\tau_\alpha)^\beta} \tag{5.1}$$

the same used in Chapter 3 for the fitting the SISFs of SPC/E bulk water. The best fitting curve at each temperature is shown superimposed to data point in Figure 5.3. This model well reproduces the line-shape of the correlators, apart for low temperature curves at long times due to the poorer statistics of our calculation.

The parameters extracted from the fitting procedure are shown in Figures 5.4 and 5.5.

In the top panel of Fig. 5.4, the characteristic time of the Gaussian term of Eq. (5.1), τ_s, is plotted as a function of temperature. It is of order 0.15 ps as in SPC/E water and has a weak temperature dependence as expected in the ballistic regime. The Lamb-Mössbauer factor, $f(q)$, which arises from the cage effect, is plotted in the middle panel of the same Figure. It increases upon cooling reflecting the decrease of the characteristic distance over which the particle rattles inside the cage due to the interactions with first nearest neighbor molecules. Through the relation $f(q) = e^{-a^2q^2/3}$ we can estimate the scale length a of this motion, which gives $a = 0.43$ Å at T = 300 K and $a = 0.35$ Å at T = 200 K. Both the

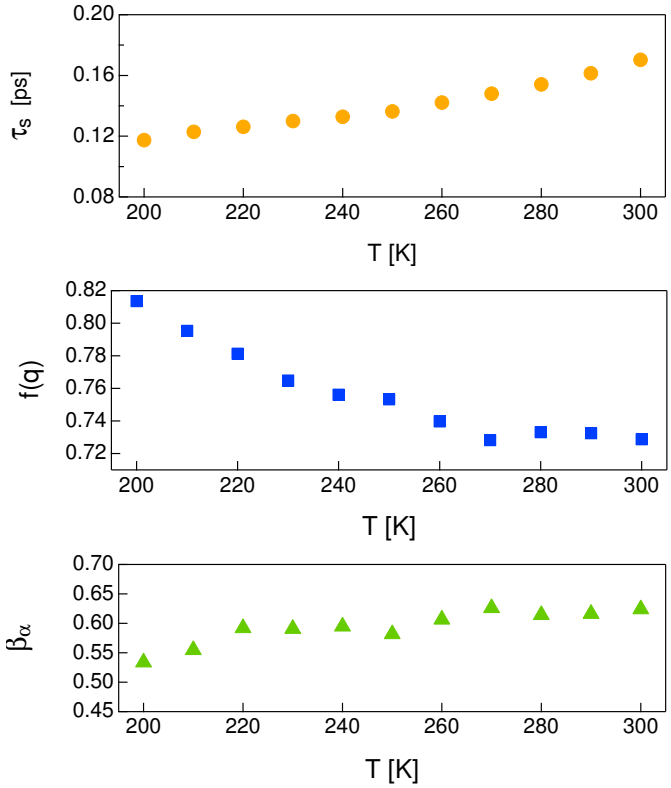

Figure 5.4: Fast-relaxation times τ_s, Lamb-Mössbauer factors $f(q)$ and stretching parameters of the α-relaxation, β_α, extracted from the fit procedure via Eq. (5.1) of the oxygen-oxygen SISFs in LiCl:6H_2O. Data are shown as a function of the temperature of the system.

distances are well shorter than the distance of the first nearest neighbors (evidences for this will be given in RDFs shown in the next Section). Finally on this Figure, it is reported the stretching parameter of the α-relaxation, β_α. It is rather constant in temperature from T~300 K down to T~220 K and it decreases slightly below this temperature. There is no available simulations data in literature to compare its value with bulk system's, but along the 1 bar isobar β_α of SPC/E water varies within the interval 0.9–0.6 upon cooling, and the same occurs in the TIP4P series of water potential along the 1 g/cm^3 isochores [38, 47]. Our β_α values reveal the fact that the dynamics of water is more stretched in LiCl:6H_2O than in bulk water.

The other relevant quantity that characterizes the dynamics of supercooled water is the structural α-relaxation time, τ_α. This quantity, as extracted from the fit of SISFs, is plotted in the log-lin plot on Figure 5.5 as a function of temperature. The α-relaxation in LiCl:6H_2O is clearly slower than in bulk water. Typically, τ_α in bulk water varies from 1 to

1000 ps upon cooling the system in the range 300 - 200 K.

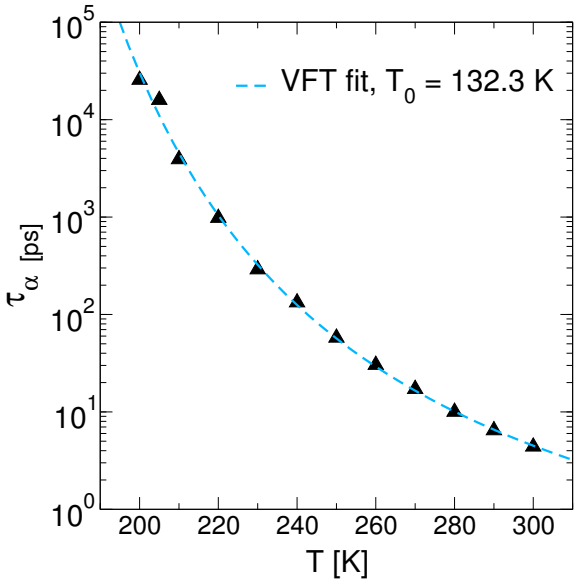

Figure 5.5: Structural α-relaxation times of water in LiCl:6H_2O as a function of temperature. Data are extracted from the fit procedure via Eq. (5.1) of the oxygen-oxygen SISFs. The Vogel-Fulcher-Tammann approximation is also shown superimposed to the data points.

It is common in literature to describe the temperature behavior of relaxation times and viscosities of glass-forming liquids with the phenomenological Vogel-Fulcher-Tammann (VFT) law, given by:

$$\tau_\alpha = \tau_0 \exp\left[\frac{DT_0}{T - T_0}\right] \tag{5.2}$$

where τ_0, τ_0 and T_0 are constants. T_0 is often referred as the temperature of *ideal* glass transitions, but its relation with the real glass transition temperature is highly debated [2]. D is the fragility parameter whose variations between 5 and 100 can described supercooled liquids from fragile to strong extremes in the Angel plot [46].

The relaxation times of water in LiCl:6H_2O are found to obey a Vogel-Fulcher-Tammann law with $D = 7.56$, which classified the water of our solution as a fragile liquid and $T_0 = 132.3$ K, which is close to the values reported in literatures by NSE 148$\pm$16 on LiCl:7.3H_2O [177]. The VFT law, reported in Figure 5.5, well describes the temperature behavior of τ_α in the entire regime of temperature that we simulated. Finally, we can also extrapolate the glass transition temperature of the solution extrapolating the value of τ_α from the VFT equation, since conventionally $\tau_\alpha(T_g) = 10^2$

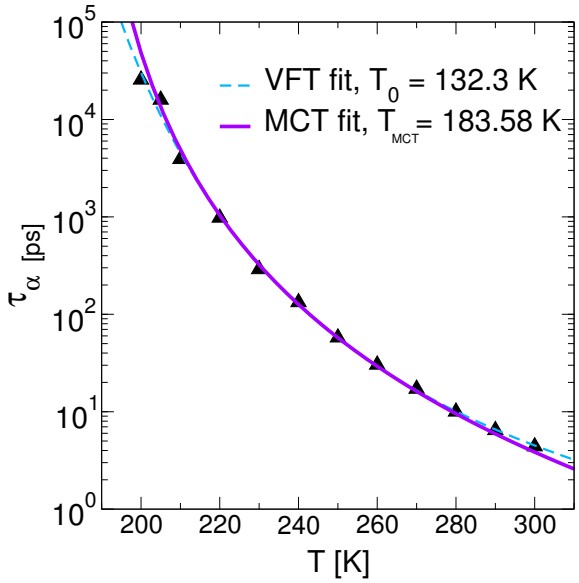

Figure 5.6: Structural α-relaxation time of water in LiCl:6H_2O as a function of the temperature. Data are extracted from the fit procedure via Eq. (5.1) of the oxygen-oxygen SISFs, same of Figure 5.5.

s. We found T_g =159.5 K. This temperature is higher than in the real solution, of ~ 25 degree.

As stated in the introduction, fragile glass-former liquids show super-Arrhenius behavior of relaxation times and can be described or with the VFT law or with MCT power law. Next Section deals with the analysis *à la* Mode Coupling of τ_α(T).

5.3.2. α-relaxation and MCT

Figure 5.6 shows that in the range of temperature that we studied in the mild supercooled region, the temperature dependence of the τ_α follows the power law prediction of the MCT:

$$\tau_\alpha \sim (T - T_{MCT})^{-\gamma} \tag{5.3}$$

The best fit shown is obtained by excluding the two lowest temperature points. Nonetheless also at low temperature the agreement with the MCT law is rather good. This can be also appreciated in Figure 5.7, where the structural α-relaxation times and its MCT power law are show as a function of inverse temperature in an Arrhenius plot on the left panel and as function of the distance from the MCT temperature on the right panel.

The extracted parameter are $\gamma = 4.60$ and $T_{MCT} = 185.0$ K. The γ value should be in principle universal, in practice it depends on the system

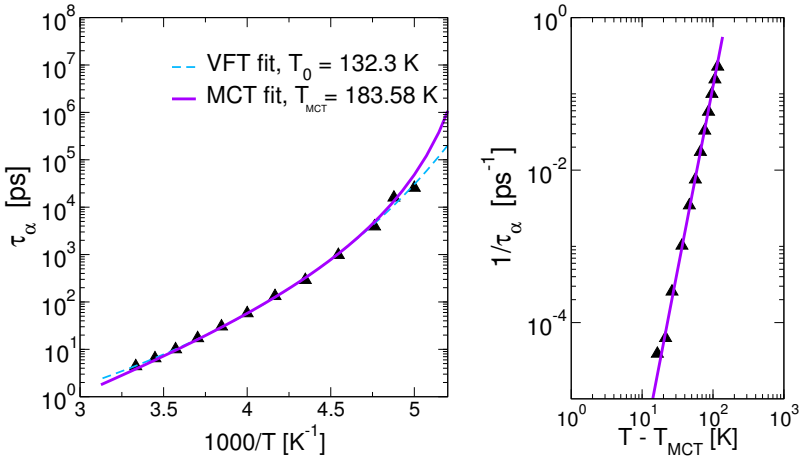

Figure 5.7: Structural α-relaxation time of water in LiCl:6H_2O. Left Panel: τ_α as function of the inverse temperature. Right Panel: log-log plot of $1/\tau_\alpha$ vs. $T - T_{MCT}$. The MCT fit is also shown as the continuos line superimposed to the data points.

and given the system, simulation works show that it also depends on the interaction potential employed. The value of γ is rather high with respect to the bulk. For sake of comparison, $\gamma \sim 3$ in TIP4P/2005 water, along isochores where ρ varies in 0.95−1.03 g/cm^3) [38]. In any case it has been shown that in NaCl solutions, already at very diluted condition, the γ exponent differentiates from its bulk value [134]. Concerning the MCT temperature, it has been shown [37] that for fragile liquid holds $\frac{T_{MCT}}{T_g} \leq 1.2$, in our case we estimated 1.15, which gives further support to the fact that the MCT temperature found is compatible with a fragile behavior of the glass-forming.

Globally the MCT power law describes well the structural relaxation times of the water in LiCl:6H_2O in a temperature region starting from T = 300 K until the mild supercooled region is reached. Upon further cooling the system, plausibly the VFT can best described τ_α behavior down to the glass temperature, given the deviation from the MCT power law that onsets at ~ 205 K upon cooling. The extension of simulations to lower temperature is required to clarify this point.

Nevertheless, it must be noted that the α relaxation of LiCl-6H2O as measured by Neutron Spin Echo, shows a behavior similar to our. From high temperature it obeys to power scaling law similar to MCT prediction down to T ~ 200 K [178]. Similar behavior is also found for the viscosity of the eutectic liquids [179]: the viscosity data are consistent with the MCT power law from high temperature down to ~ 220 K, while the VFT law describes the temperature behavior over the entire temperature range investigated in that work (down to 180 K).

5.3.3. Structural properties

In this Subsection the structural properties calculated from the equilibrated trajectories stored in the production run are presented. The properties investigated are radial distribution functions, angular distribution of three water molecules and hydrogen bonding distribution function. We start from the structure of water.

Water correlations

The structure of the water contained in our electrolyte solution has been characterized by calculating the three RDFs $g_{ij}(r)$, where i,j are the oxygen and hydrogen atoms (i,j = O, H). The calculation is performed between an atom pair i,j not belonging to the same molecule, so that in our $g_{ij}(r)$ the intramolecular peaks are absent with respect to experimental measured RDFs [180]. This is done because we employed a rigid potential model for water and the intramolecular peak is therefore fixed to the values of TIP4P/2005.

In Figure 5.8 we present the oxygen-oxygen $g_{OO}(r)$, oxygen-hydrogen $g_{OH}(r)$ and hydrogen-hydrogen $g_{HH}(r)$ RDFs of water, calculated at the highest, T = 300 K, and at the lowest, T = 200 K, simulated temperatures. The RDFs of water calculated at intermediate temperatures are shown in Appendix A, Figure A.1. From the comparison between the two extremes simulated temperature, it is clear that the local maxima of every RDF become in general sharper and alternating to deeper minima. This is the typical behavior of pair correlation functions upon cooling. The effect of decreasing temperature it is however more pronounced in the correlations between the oxygen atoms of two water molecules: $g_{OO}(r)$ develops in fact a shoulder to the right of the first peak clearly visible at low temperature. Correlations which implies an hydrogen atoms seems to be less sensitive to the temperature and no onset of new shoulders or peaks is detected. Overall neither the short range nor the long range order of water is strongly affected by the temperature, being the position of maxima and minima unchanged within the range of temperatures investigated. The positions of the first sharp intermolecular peaks of O-O, OH and HH correlations are resumed in Table 5.B.

To see the effect of ions on the water structure, it is desirable to compare the O-O, O-H and H-H RDFs calculated for the water in LiCl:6H_2O with the respective RDFs of bulk TIP4P/2005 water. This however must be done at comparable densities of water. For our concentrated solution, the excluded volume by ions must to be take into account in the calculation of the density of water ρ_w. Following the method used in Ref. [181] for hydrophobic solutes in water, the excluded volume due to the X ion can be approximated by a sphere of diameter equal to the LJ length between the ion and the oxygen, σ_{OX}. The total excluded volume in our

system is therefore given by:

$$V_{Excl} = \frac{\pi}{6} \left(N_{cl}\sigma_{OCl} + N_{Li}\sigma_{OLi}\right) \tag{5.4}$$

where N_{Ll}, N_{Li} is the number of Li, Cl ions in the simulation box. The density of water can be calculated as:

$$\rho_w = \frac{N_w}{V - V_{Excl}} \frac{p}{N_A} \tag{5.5}$$

where N_w is the number of water molecules, p_w is the molecular weight of water, V is the simulation box volume and N_A is the Avogadro number. Through Eq. 5.5 we calculated the equivalent water density in our system, which results to be ρ_w = 0.990 g/cm^3 at T = 300 K and ρ_w = 1.009 g/cm^3 at T = 200 K. We compared the RDF of water in the solution with the bulk TIP4P/2005 water RDFs at the closest temperature available. These O-O RDFs are reported on the same Figure 5.8.

From the comparison, we can see that LiCl has the strongest effect on the oxygen-oxygen RDFs, while leaves almost unchanged the oxygen-hydrogen and hydrogen-hydrogen RDFs. The fact that H-H correlations, which represents the orientational correlation between neighboring pure water molecules, are essentially unchanged in the aqueous solution, as well the first peak of O-H correlations at about 3.5 Å, reveals the formation of hydrogen bonds between water molecules in the system.

Nevertheless, also O-O correlations characterize the hydrogen bond network of water. The position of the first peak is unaffected by LiCl which ulteriorly confirms the formation of water HBs in the system; the broadening of this peak that degenerates into a shoulder at 3.2 Å at low temperature is the signature of the densification of oxygen atoms due to the interactions with ions. The major effect of LiCl on water, it is however the collapse of the outer hydration shells toward the first. This last point has been found in several electrolyte aqueous solutions RDFs and resumes the effect of ions on water, i.e. they act on the water HB-network as the increase of the pressure acts on pure bulk water. Finally, the collapse of the second hydration shell is directly associated to the angular perturbation of the water tetrahedral network, we will give in the next Subsection further evidences of this point.

Water ions correlations

In Figure 5.9 the cross correlations between the water oxygen atom and the two ions, $g_{\mathrm{OX}}(r)$ where X = Li, Cl are shown at two selected temperature, T = 300 K and T = 200 K, to better compare them.

OX correlations exhibit no appreciable differences upon cooling, apart from the general sharpening of peaks. The complete set calculated is reported in Appendix A, Figures A.2 and A.3.

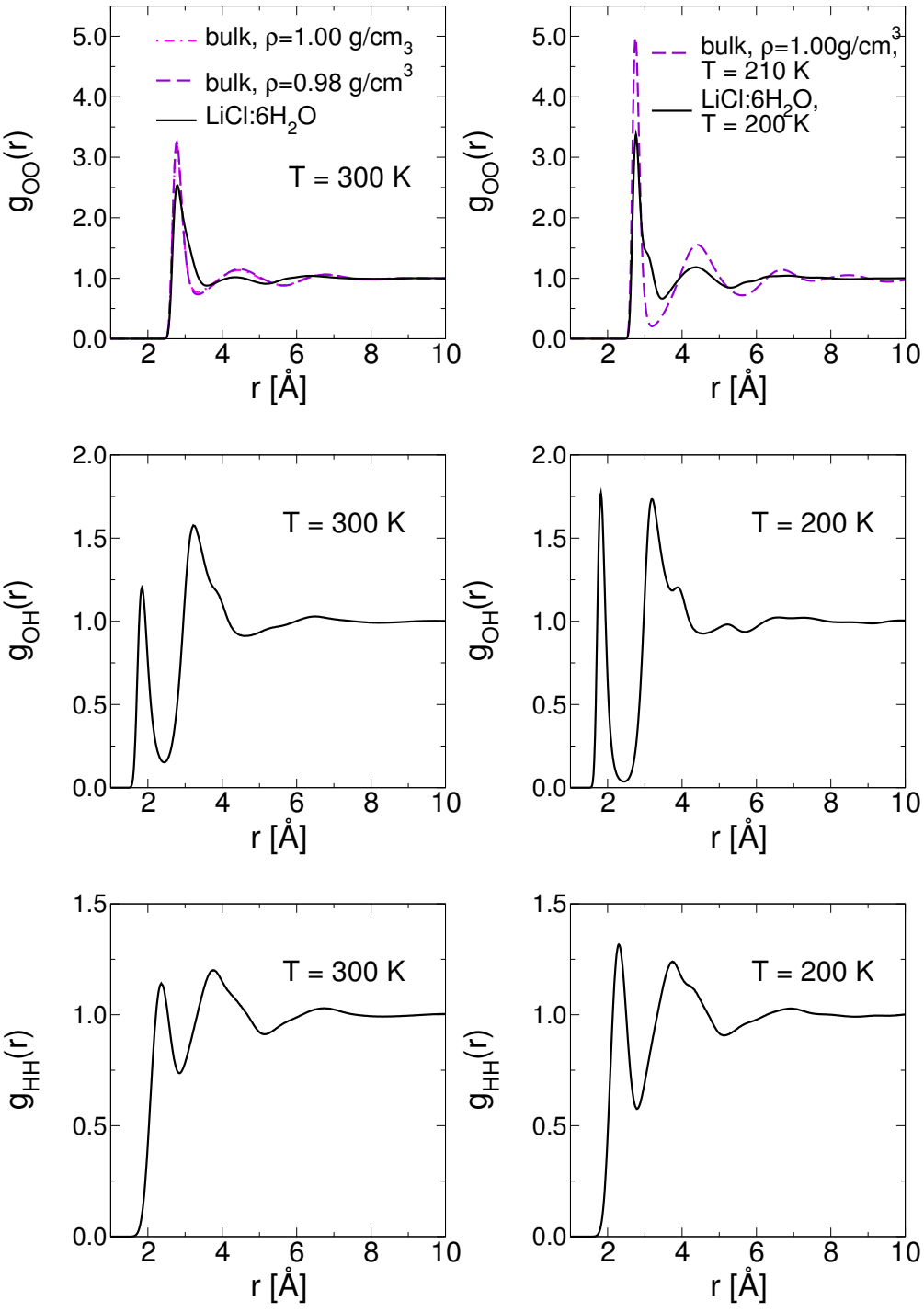

Figure 5.8: Water oxygen-oxygen RDFs (top panel), oxygen-hydrogen RDFs (middle panel) and hydrogen-hydrogen RDFs (bottom panel) in LiCl:6H_2O at select temperatures. The curves shown for T ≠ 300 K are shifted by a step of 0.4 on the y axis for the sake of clarity.

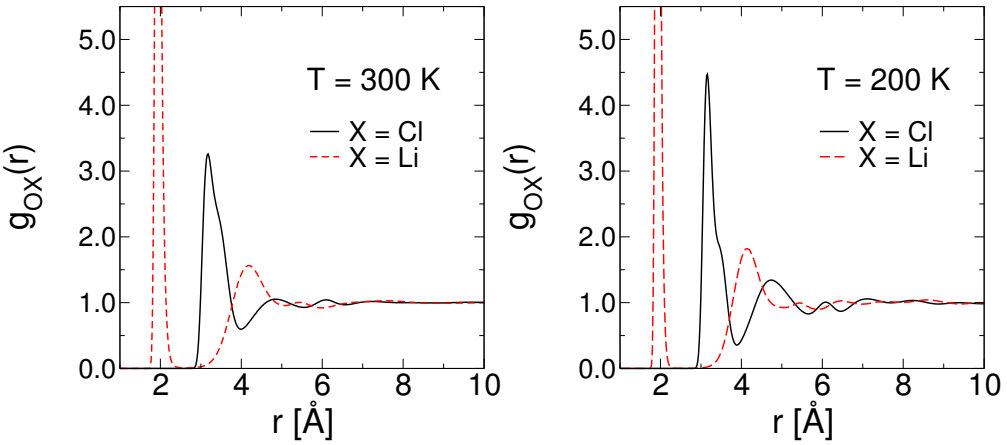

Figure 5.9: Oxygen-chlorine RDFs (top panel) and oxygen-lithium RDFs (bottom panel) in LiCl:6H_2O at select temperatures. The curves shown for T $\neq$ 300 K are shifted by a step of 0.5 in the top plot and of 5 in the bottom plot along the y axis for the sake of clarity.

In the case of lithium, a well defined shell of lithium atoms forms around the oxygen, as seen from the intense first peak located at 1.9 Å (also note the high intensity, see Fig. A.2) followed by a deep first minimum. The first shell of chlorine atoms around the oxygen is centered at 3.2 Å and it is less sharp defined with respect to the lithium first shell, as indicated by the shoulder already present at ambient temperature and the less deep first minimum. The positions of the peaks are unchanged at the two temperatures. From this comparison it can be also appreciated that chlorine coordination shells lye between lithium coordination shells, i.e. they alternates resembling the structure of the solid LiCl crystal and indicating charge ordering around the oxygen atoms.

Figure 5.10 is the analogous of Figure 5.9 for the hydrogen-ions correlations, $g_{\mathrm{HX}}(r)$, X = Li, Cl. Also in this case the decrease of temperature does not produce appreciable changes in the RDFs, the position of the principal peaks are in fact unchanged. The first peaks in the H-Cl RDF lye at 2.2, 3.6 and 3.9 Å. The coordination shells of lithium shifts to longer distances with respect to the chlorine, at 2.6 Å and 4.7 Å, between them a left-shoulder to the second peak is observed at 3.4 Å. The charge ordering of shells is still present.

The cross correlations shown at this points have been replotted in Figure 5.11, to better understand the spatial arrangement of the alternating shells of oxygen and hydrogen atoms surrounding the ions. From this Figure in fact it is clear that the position of the first peak of the g_{LiH} is shifted to a higher distance with respect to the position of the first

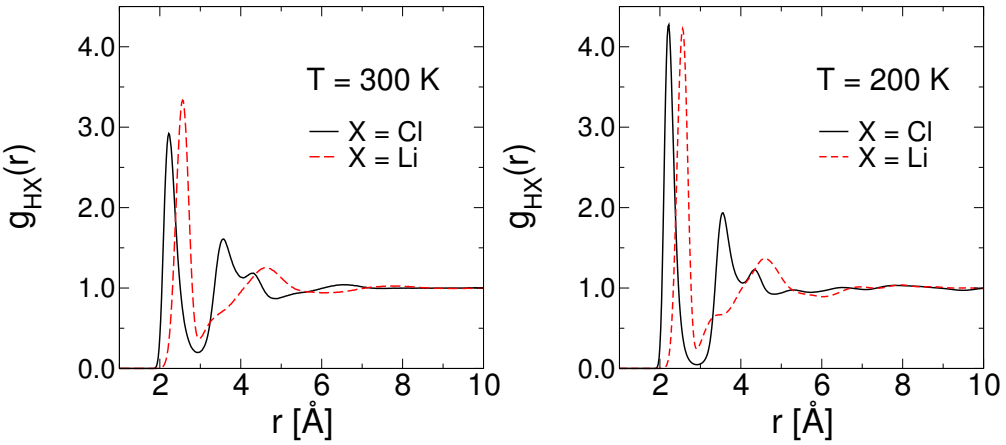

Figure 5.10: Hydrogen-chlorine RDFs (top panel) and hydrogen-lithium RDFs (bottom panel) in LiCl:6H_2O at select temperatures. The curves shown for T ≠ 300 K are shifted by a step of 0.5 on the y axis for the sake of clarity.

peak of the g_{LiO} and that the opposite is true for g_{ClH} and g_{ClO}. This is the consequence of the electrostatic interactions between the polar water molecule and the charged ions, with water molecules that arrange in such a way the oxygen is exposed to the positive charged ion, Li^+, and the hydrogen atoms oriented to the negative charged ion, Cl^-.

Ions structure

In Figure 5.12 the RDFs that characterized the ion-ion structure are shown. In the top panel, $g_{\mathrm{LiCl}}(r)$ is shown at two selected temperatures, T = 300 K and T = 200 K. Both the curves show a much intense first maximum at 2.3 Å and a second peak at 4.5 Å. The separation between these two peaks reveals the presence of a water molecule included between the two ions. In the bottom panels, Li-Li and Cl-Cl RDFs are reported. Li-Li RDF presents at T = 300 K the broad peak at 5.6 Å also observed experimentally, and a well defined pre-peak at 3.96 Å, this feature has been observed in hyperquenched samples (for the discussion of this peak see Ref. [101]). At low temperature the position of this pre-peak is unchanged, while the second shell is modulated in a double peak structure. At long distance other peaks are observed. $g_{ClCl}(r)$ appears more structured with respect to $g_{LiLi}(r)$, showing a second and third shell sharply defined both at high and low temperature (see Table 5.B for the values). The diversification on the long range order between the two ions can be due to their different sizes. Finally, the structure of ions seems to be the more temperature dependent, especially for the long distance behavior of the RDF. The complete set of ion-ion RDFs, calculated in our system are reported in Figure A.4 in the Appendix A.

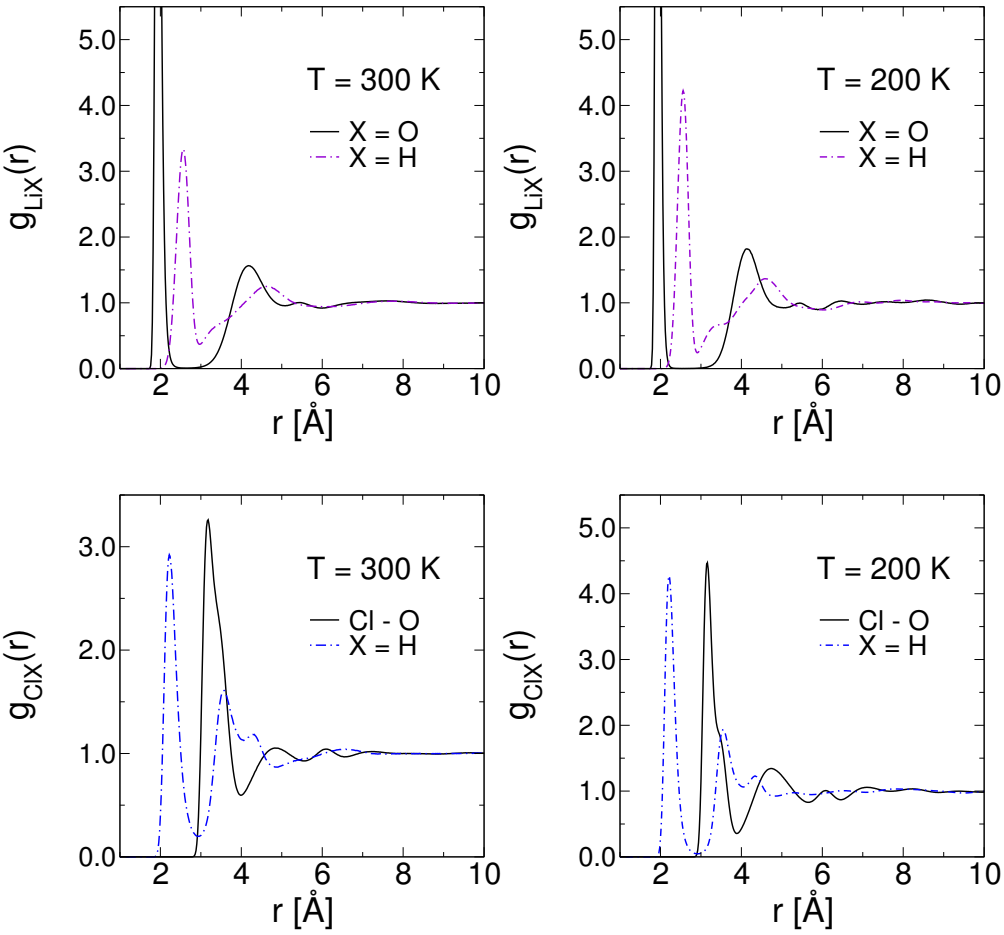

Figure 5.11: Litium-water RDFs (top panel) and chlorine-water RDFs (bottom panel) in LiCl:6H_2O at select temperatures.

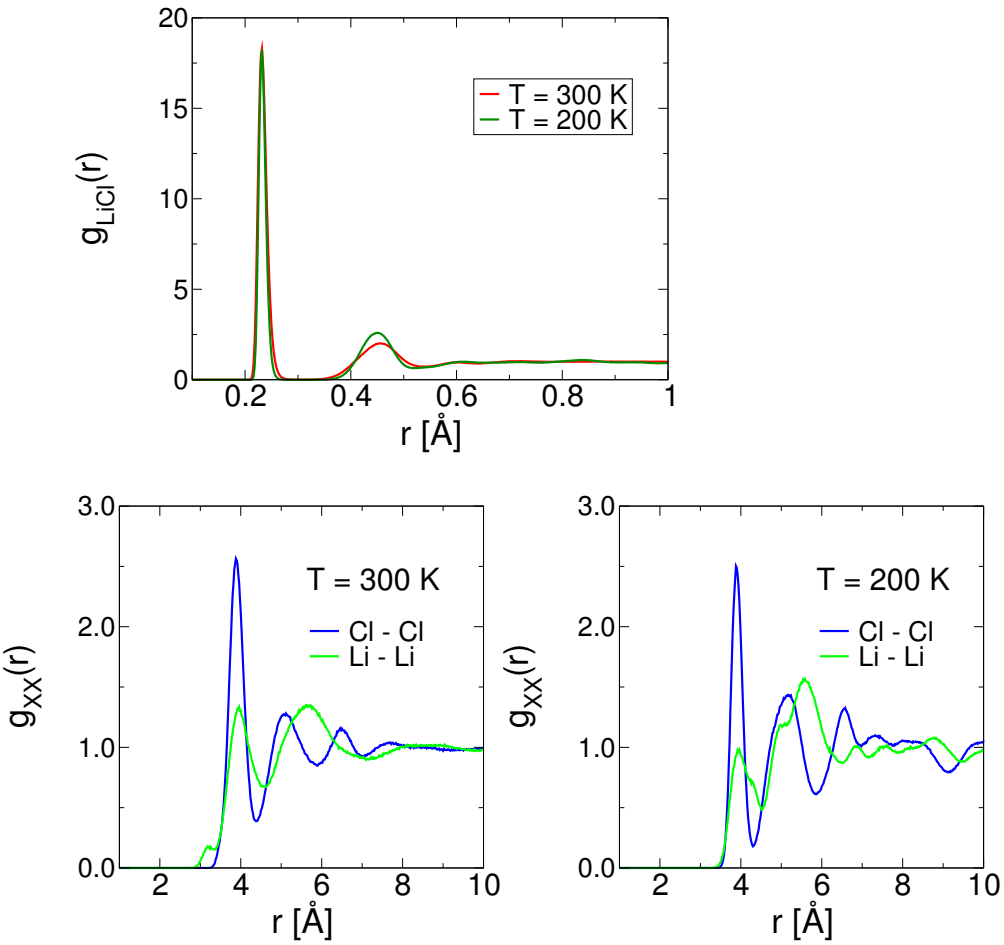

Figure 5.12: Litium-litium RDFs (top panel), chlorine-chlorine RDFs (middle panel) and litium-chlorine RDFs(bottom panel) in LiCl:6H_2O at select temperatures. The curves shown for T ≠ 300 K are shifted on the y axis by a step of 0.5, 0.5 and 5 respectively for the sake of clarity.

Table 5.B: Intermolecular peak positions extracted by the correlations of the LiCl:6H_2O system. Between parenthesis the value of ref. [180]. the value of water are reported.

Type	1st (Å)	2nd (Å)	3rd (Å))
O-O	2.8 (2.9)[1]	4.3 (4.4)	
O-H	1.8 (1.88)[1]	3.2 (3.37)	3.8
H-H	2.3 (2.4)	3.7 (3.7)	4.1
Li-Cl	2.3	4.5	-
Li-O	1.9 (2)	4.3	
Li-H	2.6	4.7	
Li-Li	4.0	5.6(+prepeak)	
Cl-O	(3.175)[1]	4.7	
Cl-H	2.2 (2.225)	3.6 (3.625)	3.9
Cl-Cl	3.9	5.1/2	6.5/6

In conclusion, since this is the first simulation at low temperature that we perform on the system LiCl:6H_2O as described by TIP4P/2005-JC, we want to comment the values reported in parenthesis in Table 5.B. Those values competes the supercooled LiCl:6H_2O at T = 162 K, derived from neutron pair correlation functions investigated by Prével et al. [180]. The [1] appended to the parenthesis refers to data of the glassy LiCl:6H_2O at T = 120 K [180]. We report these values when no available data for the supercooled liquids are found because Prével et al. [180] have found that no significant changes are between the glassy and the (deep) supercooling liquids RDFs. We see that most of the positions that we derived at much higher temperature are in very good agreement with the experimental values of both the liquids and the glass. This shows that the JC-TIP4P/2005 model well describes the molecular interactions of LiCl:6H_2O, also at low temperature.

Hydrogen Bond Network

The water radial distribution functions reveal distortion of the hydrogen bond network in our solution. This motivated the calculation of the angular distribution of water, $P(\gamma)$, in LiCl:6H_2O solution.

γ is defined to be the H-O···O angle of three water molecules. As shown in Chapter 4, the distribution of the values of γ angles assumed by water molecules, characterizes the short range order present in bulk liquid water. Therefore it is possible to monitor perturbation on the water hydrogen bond network due to the addiction of ions, by looking at this quantity. We recall now that in bulk water, especially at low temperature, the cosγ distribution is expected to have a defined peak at about the tetrahedral value of $\gamma = 109.5$ plus a secondary peak located $\sim 54°$, due to interstitial water molecules.

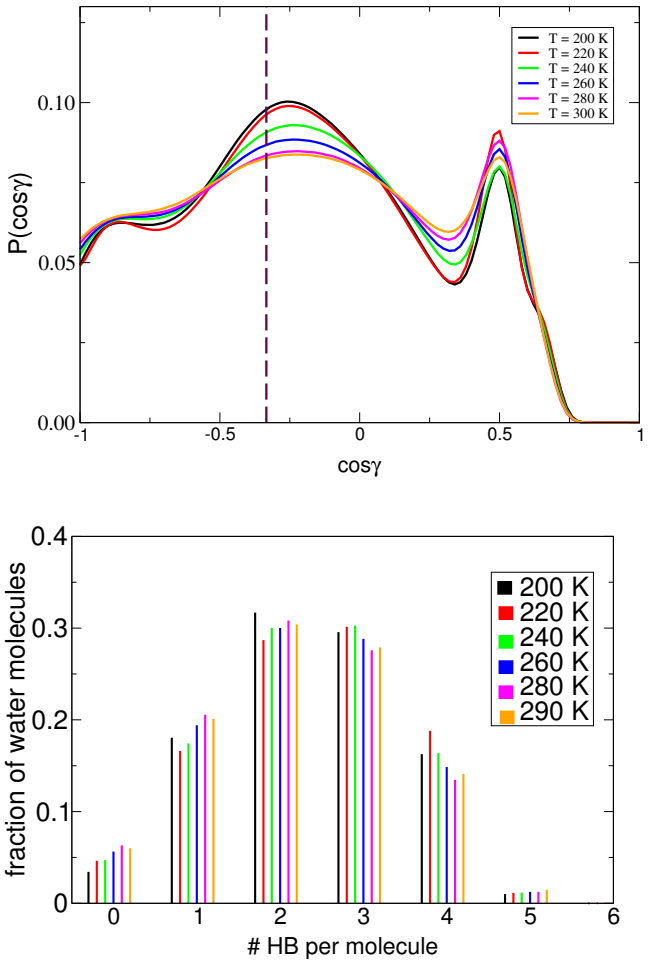

Figure 5.13: Top panel: normalized angular distribution function $P(\cos\gamma)$ of the angle between the oxygens of three nearest neighbor water molecules for water contained in the LiCl:6H_2O solution. Curves are shown from the highest simulated temperature T = 300 K down to the lowest temperature T = 200 K. The dashed vertical line marks the cosine value of the pure tetrahedral angle. Bottom panel: distributions of the number of hydrogen bonds formed per water molecule. In both the graphs, different colors correspond to different temperatures.

We calculated $P(\gamma)$ as defined in Sec. 4.2.4, by averaging the γ angle between all the couples $O_{2,3}$ of oxygen atoms that lies at a distance less than $r = 3.5$ Å from the considered O_1 atom. This cut-off length corresponds to the first minimum of the O-O RDF calculated in the solution.

The resulting water angular distribution $P(cos\gamma)$ in LiCl:6H_2O is shown in Figure 5.13. These curves show the peak at 60.3°, which is the analogous of secondary peak of bulk water due to interstitial water molecules; a peak at 104.9°, which is the signature of the tetrahedral order present in liquid water; and a third peak, missing in bulk water at any temperature, that sharpens toward low temperature, located ~ 149.9° ($cos\gamma = -0.866$).

We can see that the tetrahedral peak of the angular distribution is not totally depressed and thus conclude that bulk-like hydrogen bonds form in the system, but also that this HB network is different from the one of bulk water, being partially deformed due to the onset of a population of water molecules that assume high γ angle value.

Finally, the distribution of hydrogen bonds in the system has been calculated. We adopted the same geometry criterion for the definition of a hydrogen bond between two water molecules, i.e. O-O distance less that 3.5 Å and the H-O···O angle less than or equal to 30°.

In the bottom panel of Figure 5.13, it is shown the distribution of water population involved in $n = 0$, 1, 2, 3, 4 and 5 hydrogen bonds with an other water molecules. For sake of comparison, it must be taken into account that this distribution in bulk water typically shows its maximum at $n = 4$, while other values of n are strongly depressed upon cooling. In the case of the water in LiCl:6H_2O, most of water molecules are involved in the formation of 2 or 3 hydrogen bonds. The lack of the fourth HB is plausibly related to distortion of water network in the solution, with water molecules found at high angle that can not anymore satisfying our geometrical constrain. In connection to this, remarkably it is the non-zero population of water involved in zero HB.

5.4. Conclusions

We performed MD computer simulations of the glass forming solution LiCl:6H_2O, under ambient pressure $p = 1$ bar for temperature ranging in the interval 300 - 200 K. The potential used for describing the intermolecular interactions of atoms and molecules contained in the solution is the JC-TIP4P/2005 [101], in which water is described with the four-site TIP4P/2005 potential and modified Lorentz-Berthelot mixing rules were implemented to better reproduce experimental properties of the system at ambient condition.

In this Chapter we have shown the dynamical properties of the water contained in the solutions, derived from the oxygen-oxygen SISFs, and

structural properties that characterize the short and long range order of the system.

Water in the solutions is strongly slowed down by the interaction with ions, this conclusion is based on the longer (~ a factor 10) time scale of the typical α-relaxation of bulk liquid water. Water is also found to behave as a fragile liquid upon supercooling, which it is in accordance with experimental determination. The MCT describes well the phenomenology, i.e. the cage effect, of the SISFs at any investigated temperature. The α-relaxation time is found to follow the MCT prediction down to the mild supercooling region, nevertheless below ~ 210 K the structural relaxation times of LiCl:6H_2O water seems to deviates from the predicted law. But this last point merits further investigation by extending simulations well below 200 K.

From the structural point of view, in analogy with other ionic aqueous solutions, the LiCl salt, while preserving the water hydrogen bond in the system, strongly affects the O-O coordination shells of water. The principal effect is on the second shell of the O-O radial distribution function, which affects the tetrahedral structure of the water network. This have been also observed by the direct calculation of the angular distribution of three water molecules, that also gives the basic idea of the distortion induced by LiCl: a certain number of water molecules are in fact found at larger angle than the nearly tetrahedral one that characterized bulk water.

Overall the JC-TIP4P/2005 is found to perform well also at low temperature in reproducing the structure of the supercooled LiCl:6H_2O solution.

6

General Conclusions and Outlooks

With this work we aimed to the description of supercooled water in different environments with respect to that of bulk phase. We study two systems of biological relevance where a protein is immersed in water and in a trehalose-water solutions, and a water salt solution. Detailed discussion and conclusions about our findings on three studied systems were drawn at the end of each Chapter. Here we intend to resume the main findings an to draw general conclusions, highlighting the future works that will be done and that are inspired by the results presented here.

Most of the time during the three-years PhD program, was dedicated to the study of the hydration water in bio-systems. A massive set of very long simulation of this system and the possibility to perform multicore analysis on the trajectories created, revealed new features about relaxations at protein interfaces, and these features have become central in my work. The presence of two structural relaxations of hydration water is now well-established along the 1 bar isobar for temperatures from 300 K down to 200 K. The two structural relaxations times lye on two separated time scales and behave differently upon cooling. The long relaxation of hydration water exhibits a strong behavior over the entire range of investigated temperatures, nonetheless showing a crossover to a higher activation energy regime upon cooling, in coincidence with the protein dynamical transition accompanying the consequent reduced softness of the protein at low temperature. This prompts to a dynamical coupling of the protein and its hydration water. The faster one, the α-relaxation time, shows a fragile-to-strong crossover shifted toward higher temperature with respect the fragile-to-strong crossover of bulk water. This crossover is related to the anomalies of water, and the fact that it occurs

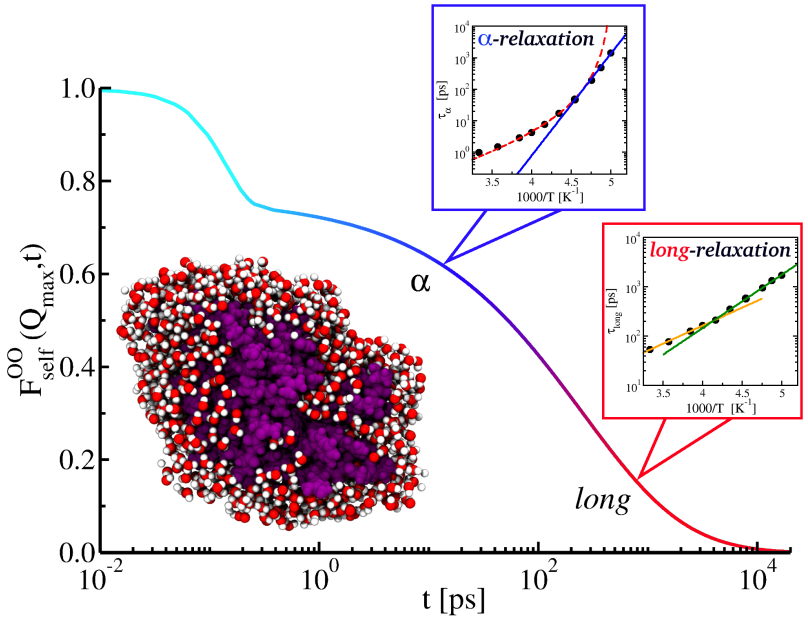

at higher temperature stresses the possibility to find a liquid-liquid critical point also in the phase diagrams of protein hydration water. In the picture of this conclusive Chapter, the two relaxations are shown.

The study of the tertiary solution evidenced that the presence of the cryoprotectant trehalose in the protein-water solution, strongly slows down the dynamics of all the system, including hydration water. In the previous work of my research group [121], density-density autocorrelation functions calculated inside the hydration shell of the protein revealed the α-relaxation, but the long relaxation was not clearly detected, because of the low long-time statistics. With the present work, we overcame this issue, especially at the higher temperature, and we were able to characterize both the α and the long relaxation upon cooling. Importantly trehalose seems to influence most this long process. In particular, trehalose causes a strong slowing down of this process, without changing neither its dynamical feature, i.e. its strong-to-strong crossover, nor the temperature at which it occurs. We also found that this process remains coupled with the protein motion, as we detected the protein dynamical transition at almost unchanged temperature with respect to the lysozyme protein dynamical transition detected when lysozyme is immersed in bulk water. We observed sugar molecules forming a cage around the surface of the protein that keeps however the protein hydrated. This

presumably permits to create a viscous water rich environment that prevent the damage upon freezing. The dynamics of this trehalose cage upon cooling remains to be investigated, as it could be coupled with the protein and hydration water revealing some new microscopic mechanism for bio-protection.

We have evidences, drawn by the comparison of our results, that the shift of peculiar water dynamics, i.e. the α relaxation, in protein hydration water depends on the considered protein hydration level. Future work in the research field on supercooled water aimed to enter into the no-man's land, will be devoted to the calculation of the α relaxation in narrower protein hydration shells. In that respect, we think that a reasonable upper limit for the fragile-to-strong crossover in protein hydration water is the protein dynamical transition. This work is already started. We have proved that for our systems, the hydrogen bond networks of the water close to the protein is not greatly affected. Reasonably, this is the reason for the existence in protein hydration water of the α-relaxation, which is connected to the continuos breaking and forming of hydrogen bonds.

Finally, the dynamics and the structure of the glass-forming $LiCl{:}6H_2O$, as described by the JC-TIP4P/2005 potential, were studied. We found that this is a very good potential that reproduces the experimental features of the system. This potential reproduces the correct fragile behavior of the solution down to 200 K and also the structure of the system, as investigated through radial distribution functions, is in accordance with the experimental determination. Due to the good agreement of this potential with the experimental findings, we will perform further work in this mixtures as function of concentrations.

I hope that with this Thesis we have add a further piece to the unfinished puzzle that is, still today, water.

A

$LiCl{:}6H_2O$ Radial Distribution Functions

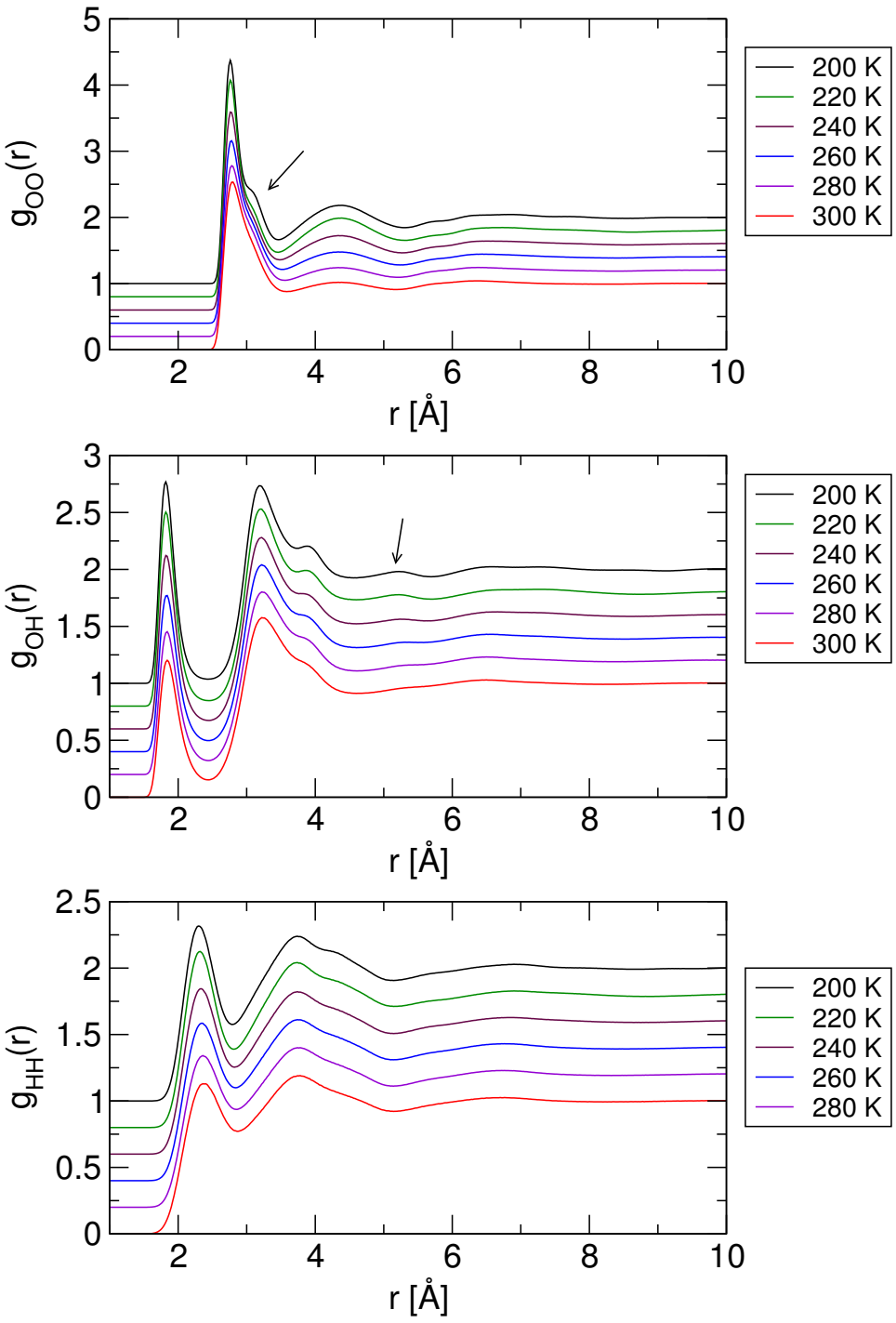

Figure A.1: Water oxygen-oxygen RDFs (top panel), oxygen-hydrogen RDFs (middle panel) and hydrogen-hydrogen RDFs (bottom panel) in LiCl:6H_2O at select temperatures. The curves shown for T ≠ 300 K are shifted by a step of 0.4 on the y axis for the sake of clarity.

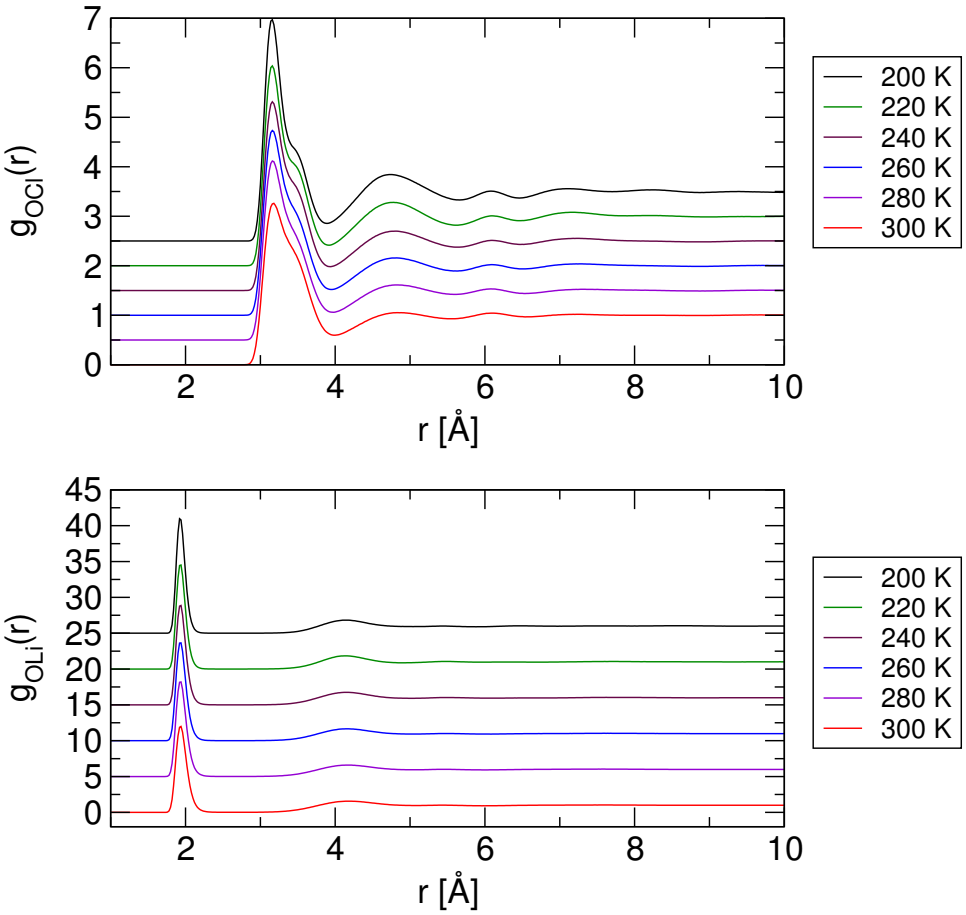

Figure A.2: Oxygen-chlorine RDFs (top panel) and oxygen-lithium RDFs (bottom panel) in LiCl:6H_2O at select temperatures. The curves shown for T $\neq$ 300 K are shifted by a step of 0.5 in the top plot and of 5 in the bottom plot along the y axis for the sake of clarity.

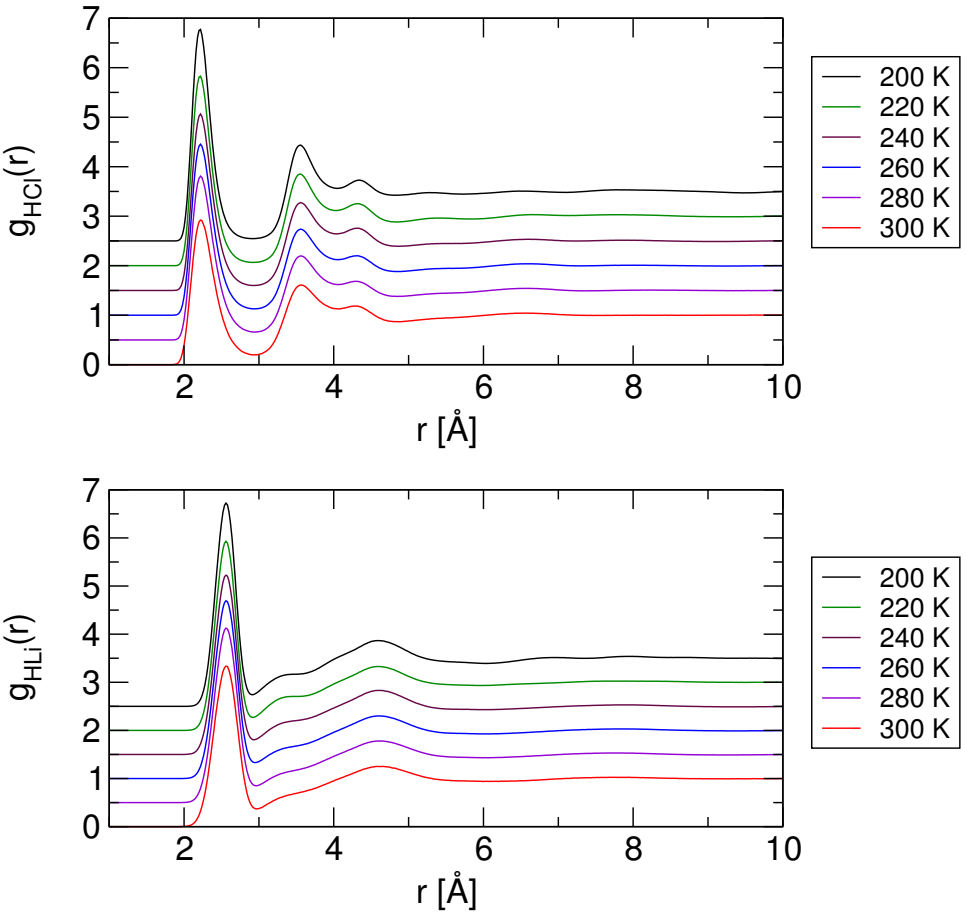

Figure A.3: Hydrogen-chlorine RDFs (top panel) and hydrogen-lithium RDFs (bottom panel) in LiCl:6H_2O at select temperatures. The curves shown for T ≠ 300 K are shifted by a step of 0.5 on the y axis for the sake of clarity.

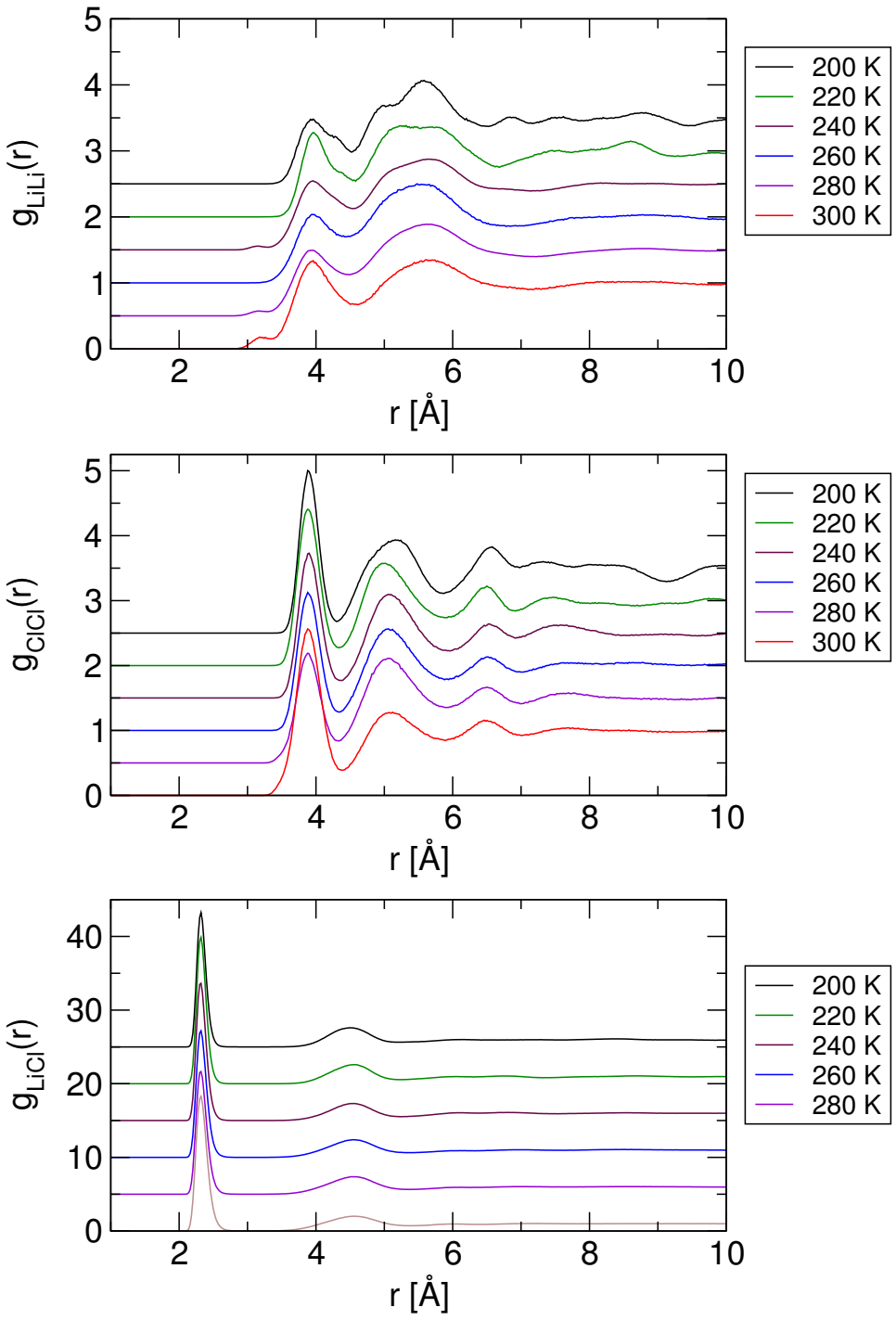

Figure A.4: Litium-litium RDFs (top panel), chlorine-chlorine RDFs (middle panel) and litium-chlorine RDFs(bottom panel) in LiCl:6H_2O at select temperatures. The curves shown for T $\neq$ 300 K are shifted on the y axis by a step of 0.5, 0.5 and 5 respectively for the sake of clarity.

B

Publications and Presentations

List of publications relative to the results presented in this Thesis

- G. Camisasca, M. De Marzio, D. Corradini, P. Gallo, *Low Temperature Dynamic Crossovers in Protein Hydration Water*, J. Chem. Phys. 145, 44503 (2016).
- G. Camisasca, M. De Marzio, Mauro Rovere and P. Gallo, *Slow dynamics and structure of supercooled water in confinement*, submitted to Entropy, Special Issue "Nonequilibrium Phenomena in Confined Systems" (2016).
- M. De Marzio, G. Camisasca, Mauro Rovere and P. Gallo, *Fragile to strong crossover and Widom line in supercooled water: a comparative study*, Submitted to Front. Phys. (2016).
- G. Camisasca, M. De Marzio and P. Gallo, *Structural characterization of trehalose cryoprotectant solutions*, in preparation (2017).
- G. Camisasca, M. De Marzio and P. Gallo, *Dynamics and structure of the glass-forming LiCl:6H_2O*, in preparation (2017).

List of presentations (on the results of biological systems)

- Workshop *Roma Tre Workshop on Water under Extreme Conditions*,10-12 Jun 2015. Held at Università degli Studi Roma Tre, Rome. Oral Presentation
- Conference *Frontiers in Water Biophysics*, 7-12 Sept 2015. Held at Ettore Majorana Foundation and Center for Scientific Culture in Erice, Italy. Poster Presented.

- Conference *MRS Fall Meeting and Exhibit 2015, Symposium Liquids and Glassy Soft Matter-Theoretical and Neutron Scattering Studies*, 30 Nov-5 Dec 2015. Held in Boston, USA. Poster Presented.
- Conference *Sitges Conference on Statistical Mechanics: "Nonequilibrium Phenomena in Con- fined Systems"*, 6-10 Jun 2016. Held in Barcelona, Spain. Oral Presentation.
- Conference *STAT-PHYS 2016 satellite meeting: Water X: exotic properties of water under extreme conditions*, 23-26 Jul 2016. Held in Nice, France. Poster Presented.

Bibliography

[1] Ball, P. Water: Water — an enduring mystery. *Nature* **452**, 291–292 (2008).

[2] Debenedetti, P. G. Supercooled and glassy water. *J. Phys. Condens. Matter* **15**, R1669–R1726 (2003).

[3] Angell, C. A., Bressel, R. D., Hemmati, M., Sare, E. J., and Tucker, J. C. Water and its anomalies in perspective: tetrahedral liquids with and without liquid–liquid phase transitions. *Phys. Chem. Chem. Phys.* **2**, 1559–1566 (2000).

[4] Debenedetti, P. G. and Stanley, H. E. Supercooled and glassy water. *Phys. Today* **56**, 40–46 (2003).

[5] Gallo, P., Amann-Winkel, K., Angell, C. A., Anisimov, M. A., Caupin, F., Chakravarty, C., Lascaris, E., Loerting, T., Panagiotopoulos, A. Z., Russo, J., Sellberg, J. A., Stanley, H. E., Tanaka, H., Vega, C., Xu, L., and Pettersson, L. G. M. Water: A Tale of Two Liquids. *Chem. Rev.* **116**, 7463–7500 (2016).

[6] Mishima, O. and Stanley, H. E. The relationship between liquid, supercooled and glassy water. *Nature* **396**, 329–335 (1998).

[7] Angell, C. A., Shuppert, J., and Tucker, J. C. Anomalous properties of supercooled water. Heat capacity, expansivity, and proton magnetic resonance chemical shift from 0 to -38%. *J. Phys. Chem.* **77**, 3092–3099 (1973).

[8] Errington, J. R. and Debenedetti, P. G. Relationship between structural order and the anomalies of liquid water. *Nature* **409**, 318–21 (2001).

[9] Poole, P. H., Sciortino, F., Essmann, U., and Stanley, H. E. Phase behaviour of metastable water. *Nature* **360**, 324–328 (1992).

[10] Mishima, O. and Stanley, H. E. Decompression-induced melting of ice IV and the liquid-liquid transition in water. *Nature* **392**, 164–168 (1998).

[11] Franks, F. *Water : A Matrix of Life*. RSC Paperbacks. The Royal Society of Chemistry Cambridge, UK 2nd editio edition (2000). ISBN 978-0-85404-583-9.

[12] Rasmussen, B. F., Stock, A. M., Ringe, D., and Petsko, G. A. Crystalline ribonuclease A loses function below the dynamical transition at 220 K. *Nature* **357**, 423–424 (1992).

[13] Ringe, D. and Petsko, G. A. The 'glass transition' in protein dynamics: what it is, why it occurs, and how to exploit it. *Biophys. Chem.* **105**, 667–680 (2003).

[14] Cordone, L., Cottone, G., Cupane, A., Emanuele, A., Giuffrida, S., and Levantino, M. Proteins in saccharides matrices and the trehalose peculiarity: Biochemical and biophysical properties. *Curr. Org. Chem.* **19**, 1684–1706 (2015).

[15] Császár, A. G., Czakó, G., Furtenbacher, T., Tennyson, J., Szalay, V., Shirin, S. V., Zobov, N. F., and Polyansky, O. L. On equilibrium structures of the water molecule. *J. Chem. Phys.* **122**, 214305 (2005).

[16] Silvestrelli, P. L. and Parrinello, M. Structural, electronic, and bonding properties of liquid water from first principles. *J. Chem. Phys.* **111**, 3572–3580 (1999).

[17] Cmglee, W. C. Phase diagram of water as a log-lin chart with pressure from 1 pa to 1 tpa and temperature from 0 k to 650 k, https://it.wikipedia.org/wiki/file:phase_diagram_of_water.svg (2007).

[18] Simeoni, G. G., Bryk, T., Gorelli, F., Krisch, M., Ruocco, G., Santoro, M., and Scopigno, T. The Widom line as the crossover between liquid-like and gas-like behaviour in supercritical fluids. *Nat. Phys.* **6**, 503–507 (2010).

[19] Gallo, P., Corradini, D., and Rovere, M. Widom line and dynamical crossovers as routes to understand supercritical water. *Nat. Commun.* **5**, 5806 (2014).

[20] Chaplin, M. Water Structure and Science (2000).

[21] Angell, C. A. and Kanno, H. Density maxima in high-pressure supercooled water and liquid silicon dioxide. *Science (80-.).* **193**, 1121–2 (1976).

[22] Mallamace, F., Branca, C., Broccio, M., Corsaro, C., Mou, C.-Y., and Chen, S.-H. The anomalous behavior of the density of water in the range 30 K < T < 373 K. *Proc. Natl. Acad. Sci.* **104**, 18387–18391 (2007).

[23] Brovchenko, I., Geiger, A., and Oleinikova, A. Multiple liquid–liquid transitions in supercooled water. *J. Chem. Phys.* **118**, 9473 (2003).

[24] Liu, D., Zhang, Y., Chen, C.-C., Mou, C.-Y., Poole, P. H., and Chen, S.-H. Observation of the density minimum in deeply supercooled confined water. *Proc. Natl. Acad. Sci.* **104**, 9570–9574 (2007).

[25] Speedy, R. J. and Angell, C. A. Isothermal compressibility of supercooled water and evidence for a thermodynamic singularity at −45°C. *J. Chem. Phys.* **65**, 851 (1976).

[26] Debenedetti, P. G. *Metastable liquids: concepts and principles*. Princeton University Press Princeton, NJ (1996).

[27] Yan, Z., Buldyrev, S. V., Kumar, P., Giovambattista, N., Debenedetti, P. G., and Stanley, H. E. Structure of the first- and second-neighbor shells of simulated water: Quantitative relation to translational and orientational order. *Phys. Rev. E - Stat. Nonlinear, Soft Matter Phys.* **76**, 051201 (2007).

[28] Nilsson, A. and Pettersson, L. G. M. The structural origin of anomalous properties of liquid water. *Nat. Commun.* **6**, 8998 (2015).

[29] Agarwal, M., Alam, M. P., and Chakravarty, C. Thermodynamic, diffusional, and structural anomalies in rigid-body water models. *J. Phys. Chem. B* **115**, 6935–6945 (2011).

[30] Poole, P. H., Sciortino, F., Grande, T., Stanley, H. E., and Angell, C. A. Effect of Hydrogen Bonds on the Thermodynamic Behavior of Liquid Water. *Phys. Rev. Lett.* **73**, 1632–1635 (1994).

[31] Sastry, S., Debenedetti, P. G., Sciortino, F., and Stanley, H. E. Singularity-free interpretation of the thermodynamics of supercooled water. *Phys. Rev. E* **53**, 6144–6154 (1996).

[32] Xu, L., Kumar, P., Buldyrev, S. V., Chen, S.-H., Poole, P. H., Sciortino, F., and Stanley, H. E. Relation between the Widom line and the dynamic crossover in systems with a liquid-liquid phase transition. *Proc. Natl. Acad. Sci. U. S. A.* **102**, 16558–62 (2005).

[33] Holten, V., Bertrand, C. E., Anisimov, M. A., and Sengers, J. V. Thermodynamics of supercooled water. *J. Chem. Phys.* **136**, 094507 (2012).

[34] Ito, K., Moynihan, C. T., and Angell, C. A. Thermodynamic determination of fragility in liquids and a fragile-to-strong liquid transition in water. *Nature* **398**, 492–495 (1999).

[35] Harrington, S., Poole, P. H., Sciortino, F., and Stanley, H. E. Equation of state of supercooled water using the extended simple point charge intermolecular potential. *J. Chem. Phys.* **107**, 7512 (1997).

[36] Scala, A., Starr, F. W., La Nave, E., Stanley, H. E., and Sciortino, F. Free energy surface of supercooled water. *Phys. Rev. E* **62**, 8016–8020 (2000).

[37] Götze, W. *Complex Dynamics of Glass-Forming Liquids*. Oxford University Press New York, USA (2009). ISBN 9780199235346.

[38] De Marzio, M., Camisasca, G., Rovere, M., and Gallo, P. Mode Coupling Theory And Fragile To Strong Transition In Supercooled TIP4P/2005 Water. *J. Chem. Phys.* **144**, 074503 (2016).

[39] Rössler, E., Sokolov, A. P., Kisliuk, A., and Quitmann, D. Low-frequency Raman scattering on different types of glass formers used to test predictions of mode-coupling theory. *Phys. Rev. B* **49**, 14967–14978 (1994).

[40] Starr, F. W., Nielsen, J. K., and Stanley, H. E. Hydrogen-bond dynamics for the extended simple point-charge model of water. *Phys. Rev. E* **62**, 579–587 (2000).

[41] Goldstein, M. Viscous Liquids and the Glass Transition: A Potential Energy Barrier Picture. *J. Chem. Phys.* **51**, 3728–3739 (1969).

[42] Gallo, P., Sciortino, F., Tartaglia, P., and Chen, S.-H. Slow Dynamics of Water Molecules in Supercooled States. *Phys. Rev. Lett.* **76**, 2730–2733 (1996).

[43] Sciortino, F., Gallo, P., Tartaglia, P., and Chen, S.-H. Supercooled water and the kinetic glass transition. *Phys. Rev. E* **54**, 6331–6343 (1996).

[44] Götze, W. and Sjogren, L. Relaxation processes in supercooled liquids. *Reports Prog. Phys.* **55**, 241–376 (1992).

[45] Li, G., Du, W., Chen, X., Cummins, H. Z., and Tao, N. J. Testing mode-coupling predictions for alpha and beta relaxation in Ca0.4K0.6(NO3)1.4 near the liquid-glass transition by light scattering. *Phys. Rev. A* **45**, 3867–3879 (1992).

[46] Angell, C. A. Liquid Fragility and the Glass Transition in Water and Aqueous Solutions. *Chem. Rev.* **102**, 2627–2650 (2002).

[47] Gallo, P. and Rovere, M. Mode coupling and fragile to strong transition in supercooled TIP4P water. *J. Chem. Phys.* **137**, 164503 (2012).

[48] Zanotti, J.-M., Bellissent-Funel, M.-C., and Chen, S.-H. Relaxational dynamics of supercooled water in porous glass. *Phys. Rev. E* **59**, 3084–3093 (1999).

[49] Liu, L., Chen, S.-H., Faraone, A., Yen, C.-W., and Mou, C.-Y. Pressure dependence of fragile-to-strong transition and a possible second critical point in supercooled confined water. *Phys. Rev. Lett.* **95**, 117802 (2005).

[50] Zhang, L., Wang, L., Kao, Y.-T., Qiu, W., Yang, Y., Okobiah, O., and Zhong, D. Mapping hydration dynamics around a protein surface. *Proc. Natl. Acad. Sci. U. S. A.* **104**, 18461–6 (2007).

[51] Li, T., Hassanali, A. A., Kao, Y.-T., Zhong, D., and Singer, S. J. Hydration dynamics and time scales of coupled water-protein fluctuations. *J. Am. Chem. Soc.* **129**, 3376–82 (2007).

[52] Paciaroni, A., Cornicchi, E., Marconi, M., Orecchini, A., Petrillo, C., Haertlein, M., Moulin, M., and Sacchetti, F. Coupled relaxations at the protein-water interface in the picosecond time scale. *J. R. Soc. Interface* **6 Suppl 5**, S635–40 (2009).

[53] Fenimore, P. W., Frauenfelder, H., McMahon, B. H., and Young, R. D. Bulk-solvent and hydration-shell fluctuations, similar to alpha- and beta-fluctuations in glasses, control protein motions and functions. *Proc. Natl. Acad. Sci. U. S. A.* **101**, 14408–13 (2004).

[54] Chen, S.-H., Liu, L., Fratini, E., Baglioni, P., Faraone, A., Mamontov, E., and Fomina, M. Observation of fragile-to-strong dynamic crossover in protein hydration water. *Proc. Natl. Acad. Sci. U. S. A.* **103**, 9012–6 (2006).

[55] Chen, S.-H., Lagi, M., Chu, X.-q., Zhang, Y., Kim, C., Faraone, A., Fratini, E., and Baglioni, P. Dynamics of a globular protein and its hydration water studied by neutron scattering and MD simulations. *Spectrosc. Int. J.* **24**, 1–24 (2010).

[56] Schirò, G., Fomina, M., and Cupane, A. Communication: Protein dynamical transition vs. liquid-liquid phase transition in protein hydration water. *J. Chem. Phys.* **139**, 121102 (2013).

[57] Wood, K., Frölich, A., Paciaroni, A., Moulin, M., Härtlein, M., Zaccai, G., Tobias, D. J., and Weik, M. Coincidence of dynamical transitions in a soluble protein and its hydration water: direct measurements by neutron scattering and MD simulations. *J. Am. Chem. Soc.* **130**, 4586–7 (2008).

[58] Schirò, G., Fichou, Y., Gallat, F.-X., Wood, K., Gabel, F., Moulin, M., Härtlein, M., Heyden, M., Colletier, J.-P., Orecchini, A., Paciaroni, A., Wuttke, J., Tobias, D. J., and Weik, M. Translational diffusion of hydration water correlates with functional motions in folded and intrinsically disordered proteins. *Nat. Commun.* **6**, 6490 (2015).

[59] Lagi, M., Chu, X.-q., Kim, C., Mallamace, F., Baglioni, P., and Chen, S.-H. The low-temperature dynamic crossover phenomenon in protein hydration water: simulations vs experiments. *J. Phys. Chem. B* **112**, 1571–5 (2008).

[60] Kumar, P., Yan, Z., Xu, L., Mazza, M. G., Buldyrev, S. V., Chen, S.-H., Sastry, S., and Stanley, H. E. Glass transition in biomolecules and the liquid-liquid critical point of water. *Phys. Rev. Lett.* **97**, 177802 (2006).

[61] Markelz, A. G., Knab, J. R., Chen, J. Y., and He, Y. Protein dynamical transition in terahertz dielectric response. *Chem. Phys. Lett.* **442**, 413–417 (2007).

[62] Wood, K., Plazanet, M., Gabel, F., Kessler, B., Oesterhelt, D., Tobias, D. J., Zaccai, G., and Weik, M. Coupling of protein and hydration-water dynamics in biological membranes. *Proc. Natl. Acad. Sci. U. S. A.* **104**, 18049–54 (2007).

[63] van den Tweel, W., Harder, A., and Buitelaar, R., editors. *Stability and Stabilization of Enzymes: Proceedings of an International Symposium Held in Maastricht, The Netherlands, 22-25 November 1992*. Elsevier (1993). ISBN 1483291332.

[64] Cleland, J. L. and Langer, R. Design and Development Strategies. In *Formul. Deliv. Proteins Pept.* chapter 1, pages 1–19. ACS Symposium Series (1994).

[65] Crowe, J. H., Carpenter, J. F., Crowe, L. M., and Anchordoguy, T. J. Are freezing and dehydration similar stress vectors? A comparison of modes of interaction of stabilizing solutes with biomolecules. *Cryobiology* **27**, 219–231 (1990).

[66] Kajiwara, K. and Franks, F. Crystalline and amorphous phases in the binary system water-raffinose. *J. Chem. Soc. Faraday Trans.* **93**, 1779–1783 (1997).

[67] Di Fonzo, S., Masciovecchio, C., Bencivenga, F., Gessini, A., Fioretto, D., Comez, L., Morresi, A., Gallina, M. E., De Giacomo, O., and Cesàro, A. Concentration-temperature dependencies of

structural relaxation time in trehalose-water solutions by brillouin inelastic UV scattering. *J. Phys. Chem. A* **111**, 12577–83 (2007).

[68] Paolantoni, M., Comez, L., Gallina, M. E., Sassi, P., Scarponi, F., Fioretto, D., and Morresi, A. Light scattering spectra of water in trehalose aqueous solutions: Evidence for two different solvent relaxation processes. *J. Phys. Chem. B* **113**, 7874–7878 (2009).

[69] Lupi, L., Comez, L., Paolantoni, M., Fioretto, D., and Ladanyi, B. M. Dynamics of Biological Water: Insights from Molecular Modeling of Light Scattering in Aqueous Trehalose Solutions. *J. Phys. Chem. B* **116**, 7499–7508 (2012).

[70] Pagnotta, S. E., Alegría, A., and Colmenero, J. Dynamical behavior of highly concentrated trehalose water solutions: a dielectric spectroscopy study. *Phys. Chem. Chem. Phys.* **14**, 2991–6 (2012).

[71] Branca, C., Magazù, S., Maisano, G., and Migliardo, P. Anomalous cryoprotective effectiveness of trehalose: Raman scattering evidences. *J. Chem. Phys.* **111**, 281 (1999).

[72] Lerbret, A., Bordat, P., Affouard, F., Descamps, M., and Migliardo, F. How homogeneous are the trehalose, maltose, and sucrose water solutions? An insight from molecular dynamics simulations. *J. Phys. Chem. B* **109**, 11046–57 (2005).

[73] Lee, S. L., Debenedetti, P. G., and Errington, J. R. A computational study of hydration, solution structure, and dynamics in dilute carbohydrate solutions. *J. Chem. Phys.* **122**, 204511 (2005).

[74] Lerbret, A., Bordat, P., Affouard, F., Guinet, Y., Hédoux, A., Paccou, L., Prévost, D., and Descamps, M. Influence of homologous disaccharides on the hydrogen-bond network of water: complementary Raman scattering experiments and molecular dynamics simulations. *Carbohydr. Res.* **340**, 881–7 (2005).

[75] Malsam, J. and Aksan, A. Hydrogen bonding and kinetic/thermodynamic transitions of aqueous trehalose solutions at cryogenic temperatures. *J. Phys. Chem. B* **113**, 6792–6799 (2009).

[76] Magno, A. and Gallo, P. Understanding the Mechanisms of Bioprotection: A Comparative Study of Aqueous Solutions of Trehalose and Maltose upon Supercooling. *J. Phys. Chem. Lett.* **2**, 977–982 (2011).

[77] Di Fonzo, S., Masciovecchio, C., Gessini, A., Bencivenga, F., and Cesàro, A. Water Dynamics and Structural Relaxation in Concentrated Sugar Solutions. *Food Biophys.* **8**, 183–191 (2013).

[78] Jain, N. K. and Roy, I. Effect of trehalose on protein structure. *Protein Sci.* **18**, 24–36 (2009).

[79] GhattyVenkataKrishna, P. K. and Carri, G. A. The effect of complex solvents on the structure and dynamics of protein solutions: The case of Lysozyme in trehalose/water mixtures. *Eur. Phys. J. E* **36**, 14 (2013).

[80] Cottone, G. A comparative study of carboxy myoglobin in saccharide-water systems by molecular dynamics simulation. *J. Phys. Chem. B* **111**, 3563–9 (2007).

[81] Cordone, L., Cottone, G., and Giuffrida, S. Role of residual water hydrogen bonding in sugar/water/biomolecule systems: a possible explanation for trehalose peculiarity. *J. Phys. Condens. Matter* **19**, 205110 (2007).

[82] Giuffrida, S., Panzica, M., Giordano, F. M., and Longo, A. SAXS study on myoglobin embedded in amorphous saccharide matrices. *Eur. Phys. J. E* **34**, 87 (2011).

[83] Crowe, J. H., Crowe, L. M., and Jackson, S. A. Preservation of structural and functional activity in lyophilized sarcoplasmic reticulum. *Arch. Biochem. Biophys.* **220**, 477–484 (1983).

[84] Green, J. and Angell, C. A. Phase Relations and Vitrification in Saccharide-Water Solutions and the Trehalose Anomaly. *J. Phys. Chem.* **93**, 2880–2882 (1989).

[85] Belton, P. S. and Gil, A. M. IR and Raman spectroscopic studies of the interaction of trehalose with hen egg white lysozyme. *Biopolymers* **34**, 957–61 (1994).

[86] Fedorov, M. V., Goodman, J. M., Nerukh, D., and Schumm, S. Self-assembly of trehalose molecules on a lysozyme surface: the broken glass hypothesis. *Phys. Chem. Chem. Phys.* **13**, 2294–2299 (2011).

[87] Allen, M. P. and Tildesley, D. J. *Computer simulation of liquids*. Oxford university press (1989).

[88] Leach, A. R. *Molecular modelling: principles and applications*. Pearson education (2001).

[89] Rahman, A. Correlation in the Motion of Atoms in Liquid Argon. *Phys. Rev.* **136**, 405–411 (1964).

[90] Rahman, A. and Stillinger, F. H. J. Molecular dynamics study of liquid water. *J. Chem. Phys.* **55**, 3336–3359 (1971).

[91] Pronk, S., Páll, S., Schulz, R., Larsson, P., Bjelkmar, P., Apostolov, R., Shirts, M. R., Smith, J. C., Kasson, P. M., van der Spoel, D., Hess, B., and Lindahl, E. GROMACS 4.5: a high-throughput and highly parallel open source molecular simulation toolkit. *Bioinformatics* **29**, 845–54 (2013).

[92] Verlet, L. Computer "experiments" on classical fluids. I. Thermodynamical properties of Lennard-Jones molecules. *Phys. Rev.* **159** , 98–103 (1967).

[93] Berendsen, H. J. C., Postma, J. P. M., van Gunsteren, W. F., DiNola, A., and Haak, J. R. Molecular dynamics with coupling to an external bath. *J. Chem. Phys.* **81**, 3684 (1984).

[94] Berendsen, H. J. C., Grigera, J. R., and Straatsma, T. P. The missing term in effective pair potentials. *J. Phys. Chem.* **91**, 6269–6271 (1987).

[95] Berendsen, H. J. C., Postma, J. P. M., Gunsteren, W. F. V., and Hermans, J. *Interaction models for water in relation to protein hydration* pages 331–342. Springer Netherlands Dordrecht (1981). ISBN 978-90-481-8368-5.

[96] Jorgensen, W. L. and Madura, J. D. Temperature and size dependence for Monte Carlo simulations of TIP4P water. *Mol. Phys.* **56**, 1381–1392 (1985).

[97] Abascal, J. L. F., Sanz, E., Fernández, R. G., and Vega, C. A potential model for the study of ices and amorphous water: TIP4P/Ice. *J. Chem. Phys.* **122**, 234511 (2005).

[98] Horn, H. W., Swope, W. C., Pitera, J. W., Madura, J. D., Dick, T. J., Hura, G. L., and Head-Gordon, T. Development of an improved four-site water model for biomolecular simulations: TIP4P-Ew. *J. Chem. Phys.* **120**, 9665–9678 (2004).

[99] Abascal, J. L. F. and Vega, C. A general purpose model for the condensed phases of water: TIP4P/2005. *J. Chem. Phys.* **123**, 234505 (2005).

[100] Vega, C., Abascal, J. L. F., Conde, M. M., and Aragones, J. L. What ice can teach us about water interactions: a critical comparison of the performance of different water models. *Faraday Discuss.* **141**, 251 (2009).

[101] Aragones, J. L., Rovere, M., Vega, C., and Gallo, P. Computer simulation study of the structure of LiCl aqueous solutions: Test of non-standard mixing rules in the ion interaction. *J. Phys. Chem. B* **118**, 7680–7691 (2014).

[102] Joung, I. S. and Cheatham, T. E. Determination of alkali and halide monovalent ion parameters for use in explicitly solvated biomolecular simulations. *J. Phys. Chem. B* **112**, 9020–9041 (2008).

[103] MacKerell, A. D., Bashford, D., Bellott, M., Dunbrack, R. L., Evanseck, J. D., Field, M. J., Fischer, S., Gao, J., Guo, H., Ha, S., Joseph-McCarthy, D., Kuchnir, L., Kuczera, K., Lau, F. T., Mattos, C., Michnick, S., Ngo, T., Nguyen, D. T., Prodhom, B., Reiher, W. E., Roux, B., Schlenkrich, M., Smith, J. C., Stote, R., Straub, J., Watanabe, M., Wiórkiewicz-Kuczera, J., Yin, D., and Karplus, M. All-atom empirical potential for molecular modeling and dynamics studies of proteins. *J. Phys. Chem. B* **102**, 3586–616 (1998).

[104] MacKerell, A. D., Feig, M., and Brooks, C. L. Extending the treatment of backbone energetics in protein force fields: limitations of gas-phase quantum mechanics in reproducing protein conformational distributions in molecular dynamics simulations. *J. Comput. Chem.* **25**, 1400–15 (2004).

[105] MacKerell, A. D. and Banavali, N. K. All-atom empirical force field for nucleic acids: II. Application to molecular dynamics simulations of DNA and RNA in solution. *J. Comput. Chem.* **21**, 105–120 (2000).

[106] Foloppe, N. and MacKerell, A. D. All-Atom Empirical Force Field for Nucleic Acids : I . Parameter Optimization Based on Small Molecule and Condensed Phase Macromolecular Target Data. *J. Comput. Chem.* **21**, 86–104 (2000).

[107] Feller, S. E. and MacKerell, A. D. An Improved Empirical Potential Energy Function for Molecular Simulations of Phospholipids Supporting 2. *J. Phys. Chem. B* **104**, 7510–7515 (2000).

[108] Guvench, O., Hatcher, E. R., Venable, R. M., Pastor, R. W., and MacKerell, A. D. CHARMM Additive All-Atom Force Field for Glycosidic Linkages between Hexopyranoses. *J. Chem. Theory Comput.* **5**, 2353–2370 (2009).

[109] Guvench, O., Greene, S. N., Kamath, G., Brady, J. W., Venable, R. M., Pastor, R. W., and MacKerell, A. D. Additive empirical force field for hexopyranose monosaccharides. *J. Comput. Chem.* **29**, 2543–64 (2008).

[110] Hansen, J.-P. and McDonald, I. R. *Theory of simple liquids*. Elsevier (1990).

[111] Gallo, P., Rapinesi, M., and Rovere, M. Confined water in the low hydration regime. *J. Chem. Phys.* **117**, 369 (2002).

[112] Gabriel, E., Fagg, G. E., Bosilca, G., Angskun, T., Dongarra, J. J., Squyres, J. M., Sahay, V., Kambadur, P., Barrett, B., Lumsdaine, A., Castain, R. H., Daniel, D. J., Graham, R. L., and Woodall, T. S. Open {MPI}: Goals, Concept, and Design of a Next Generation {MPI} Implementation. In *Proceedings, 11th Eur. PVM/MPI Users' Gr. Meet.* pages 97–104 Budapest, Hungary (2004).

[113] Rocchi, C., Bizzarri, A. R., and Cannistraro, S. Water dynamical anomalies evidenced by molecular-dynamics simulations at the solvent-protein interface. *Phys. Rev. E* **57**, 3315–3325 (1998).

[114] Bizzarri, A. R. and Cannistraro, S. Molecular Dynamics of Water at the Protein−Solvent Interface. *J. Phys. Chem. B* **106**, 6617–6633 (2002).

[115] Cottone, G., Giuffrida, S., Ciccotti, G., and Cordone, L. Molecular dynamics simulation of sucrose- and trehalose-coated carboxymyoglobin. *Proteins* **59**, 291–302 (2005).

[116] Perticaroli, S., Comez, L., Sassi, P., Paolantoni, M., Corezzi, S., Caponi, S., Morresi, A., and Fioretto, D. Hydration and aggregation of lysozyme by extended frequency range depolarized light scattering. *J. Non. Cryst. Solids* **407**, 472–477 (2015).

[117] Perticaroli, S., Russo, D., Paolantoni, M., Gonzalez, M. A., Sassi, P., Nickels, J. D., Ehlers, G., Comez, L., Pellegrini, E., Fioretto, D., and Morresi, A. Painting biological low-frequency vibrational modes from small peptides to proteins. *Phys. Chem. Chem. Phys.* **17**, 11423–31 (2015).

[118] Barbosa, R. d. C. and Barbosa, M. C. Hydration shell of the TS-Kappa protein: Higher density than bulk water. *Physica A* **439**, 48–58 (2015).

[119] Comez, L., Lupi, L., Morresi, A., Paolantoni, M., Sassi, P., and Fioretto, D. More Is Different: Experimental Results on the Effect

of Biomolecules on the Dynamics of Hydration Water. *J. Phys. Chem. Lett.* **4**, 1188–1192 (2013).

[120] Corezzi, S., Sassi, P., Paolantoni, M., Comez, L., Morresi, A., and Fioretto, D. Hydration and rotational diffusion of levoglucosan in aqueous solutions. *J. Chem. Phys.* **140**, 184505 (2014).

[121] Corradini, D., Strekalova, E. G., Stanley, H. E., and Gallo, P. Microscopic mechanism of protein cryopreservation in an aqueous solution with trehalose. *Sci. Rep.* **3**, 1218 (2013).

[122] Pal, S. K., Peon, J., Bagchi, B., and Zewail, A. H. Biological Water: Femtosecond Dynamics of Macromolecular Hydration. *J. Phys. Chem. B* **106**, 12376–12395 (2002).

[123] Pal, S. K., Peon, J., and Zewail, A. H. Biological water at the protein surface: Dynamical solvation probed directly with femtosecond resolution. *Proc. Natl. Acad. Sci.* **99**, 1763–1768 (2002).

[124] Strynadka, N. C. J. and James, M. N. G. Lysozyme revisited: Crystallographic evidence for distortion of an N-acetylmuramic acid residue bound in site D. *J. Mol. Biol.* **220**, 401–424 (1991).

[125] Hess, B., Kutzner, C., van der Spoel, D., and Lindahl, E. GROMACS 4: Algorithms for Highly Efficient, Load-Balanced, and Scalable Molecular Simulation. *J. Chem. Theory Comput.* **4**, 435–447 (2008).

[126] Gallo, P., Rovere, M., and Chen, S.-H. Dynamic Crossover in Supercooled Confined Water: Understanding Bulk Properties through Confinement. *J. Phys. Chem. Lett.* **1**, 729–733 (2010).

[127] Gallo, P., Rovere, M., and Chen, S.-H. Water confined in MCM-41: a mode coupling theory analysis. *J. Phys. Condens. Matter* **24**, 064109 (2012).

[128] Starr, F. W., Sciortino, F., and Stanley, H. E. Dynamics of simulated water under pressure. *Phys. Rev. E* **60**, 6757–6768 (1999).

[129] Corradini, D., Gallo, P., Buldyrev, S. V., and Stanley, H. E. Fragile-to-strong crossover coupled to the liquid-liquid transition in hydrophobic solutions. *Phys. Rev. E* **85**, 051503 (2012).

[130] Franzese, G. and Bianco, V. Water at Biological and Inorganic Interfaces. *Food Biophys.* **8**, 153–169 (2013).

[131] Mallamace, F., Corsaro, C., Mallamace, D., Vasi, S., Vasi, C., Stanley, H. E., and Chen, S.-H. Some thermodynamical aspects of protein hydration water. *J. Chem. Phys.* **142**, 215103 (2015).

[132] Corradini, D., Gallo, P., and Rovere, M. Thermodynamic behavior and structural properties of an aqueous sodium chloride solution upon supercooling. *J. Chem. Phys.* **128**, 244508 (2008).

[133] Corradini, D., Rovere, M., and Gallo, P. A route to explain water anomalies from results on an aqueous solution of salt. *J. Chem. Phys.* **132**, 134508 (2010).

[134] Gallo, P., Corradini, D., and Rovere, M. Fragile to strong crossover at the Widom line in supercooled aqueous solutions of NaCl. *J. Chem. Phys.* **139**, 204503 (2013).

[135] Mallamace, F., Branca, C., Corsaro, C., Leone, N., Spooren, J., Stanley, H. E., and Chen, S.-H. Dynamical crossover and breakdown of the Stokes-Einstein relation in confined water and in methanol-diluted bulk water. *J. Phys. Chem. B* **114**, 1870–8 (2010).

[136] Mallamace, F., Corsaro, C., Baglioni, P., Fratini, E., and Chen, S.-H. The Dynamical Crossover phenomenon in bulk water, confined water and protein hydration water. *J. Phys. Condens. Matter* **24**, 064103 (2012).

[137] Richert, R. and Blumen, A. *Disorder effects on relaxational processes: glasses, polymers, proteins*. Springer Science & Business Media (2012).

[138] Gillen, K. T., Douglass, D. C., and Hoch, M. J. R. Self-Diffusion in Liquid Water to −31°C. *J. Chem. Phys.* **57**, 5117 (1972).

[139] Dehaoui, A., Issenmann, B., and Caupin, F. Viscosity of deeply supercooled water and its coupling to molecular diffusion. *Proc. Natl. Acad. Sci.* **112**, 12020–12025 (2015).

[140] Fletcher, N. H. The Chemical Physics of Ice. Cambridge University (1970).

[141] Wikfeldt, K. T., Nilsson, A., and Pettersson, L. G. M. Spatially inhomogeneous bimodal inherent structure of simulated liquid water. *Phys. Chem. Chem. Phys.* **13**, 19918 (2011).

[142] Mallamace, F., Chen, S.-H., Broccio, M., Corsaro, C., Crupi, V., Majolino, D., Venuti, V., Baglioni, P., Fratini, E., Vannucci, C., and Stanley, H. E. Role of the solvent in the dynamical transitions of proteins: the case of the lysozyme-water system. *J. Chem. Phys.* **127**, 045104 (2007).

[143] Parak, F. and Knapp, E. W. A consistent picture of protein dynamics. *Proc. Natl. Acad. Sci.* **81**, 7088–7092 (1984).

[144] Zanotti, J.-M., Bellissent-Funel, M.-C., and Kolesnikov, A. I. Phase transitions of interfacial water at 165 and 240 K. Connections to bulk water physics and protein dynamics. *Eur. Phys. J. Spec. Top.* **141**, 227–233 (2007).

[145] Combet, S. and Zanotti, J.-M. Further evidence that interfacial water is the main "driving force" of protein dynamics: a neutron scattering study on perdeuterated C-phycocyanin. *Phys. Chem. Chem. Phys.* **14**, 4927–34 (2012).

[146] Gallo, P. Single particle slow dynamics of confined water. *Phys. Chem. Chem. Phys.* **2**, 1607–1611 (2000).

[147] Bizzarri, A. R., Paciaroni, A., and Cannistraro, S. Glasslike dynamical behavior of the plastocyanin hydration water. *Phys. Rev. E* **62**, 3991–3999 (2000).

[148] Venturini, F., Gallo, P., Ricci, M. A., Bizzarri, A. R., and Cannistraro, S. Study of the β relaxation in supercooled confined water. *Philos. Mag. Part B* **82**, 507–515 (2002).

[149] Kumar, P., Wikfeldt, K. T., Schlesinger, D., Pettersson, L. G. M., and Stanley, H. E. The Boson peak in supercooled water. *Sci. Rep.* **3**, 1980 (2013).

[150] Wang, Z., Liu, K.-H., Le, P., Li, M., Chiang, W.-S., Leão, J. B., Copley, J. R. D., Tyagi, M., Podlesnyak, A., Kolesnikov, A. I., Mou, C.-Y., and Chen, S.-H. Boson Peak in Deeply Cooled Confined Water: A Possible Way to Explore the Existence of the Liquid-to-Liquid Transition in Water. *Phys. Rev. Lett.* **112**, 237802 (2014).

[151] Cupane, A., Fomina, M., and Schirò, G. The boson peak of deeply cooled confined water reveals the existence of a low-temperature liquid-liquid crossover. *J. Chem. Phys.* **141**, 18C510–1—-7 (2014).

[152] Wang, Z., Kolesnikov, A. I., Ito, K., Podlesnyak, A., and Chen, S.-H. Pressure Effect on the Boson Peak in Deeply Cooled Confined Water: Evidence of a Liquid-Liquid Transition. *Phys. Rev. Lett.* **115** , 235701 (2015).

[153] Mallamace, F., Corsaro, C., Mallamace, D., Wang, Z., and Chen, S.-H. The Boson peak in confined water: An experimental investigation of the liquid-liquid phase transition hypothesis. *Front. Phys.* **10**, 106103 (2015).

[154] De Marzio, M., Camisasca, G., Rovere, M., and Gallo, P. Microscopic origin of the Fragile to Strong Crossover in Supercooled Water: the role of Activated Processes. *Submitt. to J. Chem. Phys.* (2016).

[155] Chen, X., Weber, I., and Harrison, R. W. Hydration Water and Bulk Water in Proteins Have Distinct Properties in Radial Distributions Calculated from 105 Atomic Resolution Crystal Structures. *J. Phys. Chem. B* **112**, 12073–12080 (2008).

[156] Ramadugu, S. K., Chung, Y.-H., Xia, J., and Margulis, C. J. When sugars get wet. A comprehensive study of the behavior of water on the surface of oligosaccharides. *J. Phys. Chem. B* **113**, 11003–11015 (2009).

[157] Das, J., Flenner, E., Rheinstadter, M., and Kosztin, I. Sub-Diffusion and Super-Diffusion of Hydration Water Molecules at Biological Interfaces. *Biophys. J.* **98**, 666a (2010).

[158] Yamamoto, E., Akimoto, T., Yasui, M., and Yasuoka, K. Origin of subdiffusion of water molecules on cell membrane surfaces. *Sci. Rep.* **4**, 4720 (2014).

[159] Sanders, L. K., Guáqueta, C., Angelini, T. E., Lee, J. W., Slimmer, S. C., Luijten, E., and Wong, G. C. L. Structure and stability of self-assembled actin-lysozyme complexes in salty water. *Phys. Rev. Lett.* **95**, 108302 (2005).

[160] Matthews, B. W. and Remington, S. J. The three dimensional structure of the lysozyme from bacteriophage T4. *Proc. Natl. Acad. Sci. U. S. A.* **71**, 4178–82 (1974).

[161] Giuffrida, S., Cottone, G., Bellavia, G., and Cordone, L. Proteins in amorphous saccharide matrices: structural and dynamical insights on bioprotection. *Eur. Phys. J. E. Soft Matter* **36**, 79 (2013).

[162] Jedlovszky, P., Brodholt, J. P., Bruni, F., Ricci, M. A., Soper, A. K., and Vallauri, R. Analysis of the hydrogen-bonded structure of water from ambient to supercritical conditions. *J. Chem. Phys.* **108**, 8528 (1998).

[163] Cornicchi, E., Marconi, M., Onori, G., and Paciaroni, A. Controlling the protein dynamical transition with sugar-based bioprotectant matrices: a neutron scattering study. *Biophys. J.* **91**, 289–297 (2006).

[164] Fields, P. A. Review: Protein function at thermal extremes: Balancing stability and flexibility. *Comp. Biochem. Physiol. - A Mol. Integr. Physiol.* **129**, 417–431 (2001).

[165] Corradini, D. and Gallo, P. Liquid-Liquid coexistence in NaCl aqueous solutions: a simulation study of concentration effects. *J. Phys. Chem. B* **115**, 14161–6 (2011).

[166] Moran, H. E. System Lithium Chloride–Water. *J. Phys. Chem.* **60**, 1666–1667 (1956).

[167] Elarby-Aouizerat, A., Jal, J. F., Chieux, P., Letoff, J. M., Claudy, P., and Dupuy, J. Metastable crystallization products and metastable phase diagram of the glassy and supercooled aqueous ionic solutions of LiCl. *J. Non. Cryst. Solids* **104**, 203–210 (1988).

[168] Kobayashi, M. and Tanaka, H. Possible Link of the <math display="inline"> <mi mathvariant="sans-serif">V</mi> </math> - Shaped Phase Diagram to the Glass-Forming Ability and Fragility in a Water-Salt Mixture. *Phys. Rev. Lett.* **106**, 125703 (2011).

[169] Li, D., Zeng, D., Han, H., Guo, L., Yin, X., and Yao, Y. Phase diagrams and thermochemical modeling of salt lake brine systems. I. LiCl+H2O system. *Calphad* **51**, 1–12 (2015).

[170] Halalay, I. and Nelson, K. a. Time-resolved spectroscopy and scaling behavior in LiCl/H_ {2} O near the liquid-glass transition. *Phys. Rev. Lett.* **69**, 636–639 (1992).

[171] Halalay, I., Yang, Y., and Nelson, K. A. Time-resolved measurements of scaling behavior in LiCl/H2O near the liquid-glass transition. *J. Non. Cryst. Solids* **172**, 175–180 (1994).

[172] Mamontov, E. Diffusion Dynamics of Water Molecules in a LiCl Solution: A Low-Temperature Crossover. *J. Phys. Chem. B* **113**, 14073–8 (2009).

[173] Nakanishi, M., Griffin, P., Mamontov, E., and Sokolov, A. P. No fragile-to-strong crossover in LiCl-H2O solution. *J. Chem. Phys.* **136**, 124512 (2012).

[174] Gallina, M. E., Bove, L. E., Dreyfus, C., Polian, A., Bonello, B., Cucini, R., Taschin, A., Torre, R., and Pick, R. M. The low frequency phonons dynamics in supercooled LiCl, 6 H2O. *J. Chem. Phys.* **131**, 124504 (2009).

[175] Santucci, S., Comez, L., Scarponi, F., Monaco, G., Verbeni, R., Legrand, J. F., Masciovecchio, C., Gessini, A., and Fioretto, D. Onset of the alpha-relaxation in the glass-forming solution LiCl-6H2O revealed by Brillouin scattering techniques. *J. Chem. Phys.* **131**, 154507 (2009).

[176] Comez, L., Masciovecchio, C., Monaco, G., and Fioretto, D. Chapter One – Progress in Liquid and Glass Physics by Brillouin Scattering Spectroscopy. In Camley, R. E. and Stamps, R. L., editors, *Solid State Phys.* volume 63 pages 1–77. Academic Press (2012). ISBN 9780123970282.

[177] Mamontov, E. and Ohl, M. Slow dynamics of water molecules in an aqueous solution of lithium chloride probed by neutron spin-echo. *Phys. Chem. Chem. Phys.* **15**, 10732–9 (2013).

[178] Prével, B., Dupuy-Philon, J., Jal, J. F., Legrand, J. F., and Chieux, P. Structural relaxation in supercooled glass-forming solutions: a neutron spin-echo study of LiCl,6D 2 O. *J. Phys. Condens. Matter* **6**, 1279–1290 (1994).

[179] Turton, D. A., Corsaro, C., Candelaresi, M., Brownlie, A., Seddon, K. R., Mallamace, F., and Wynne, K. The structure and terahertz dynamics of water confined in nanoscale pools in salt solutions. *Faraday Discuss.* **150**, 493 (2011).

[180] Prével, B., Jal, J. F., Dupuy-Philon, J., and Soper, A. K. Structural characterization of an electrolytic aqueous solution, LiCl□ 6H2O, in the glass, supercooled liquid, and liquid states. *J. Chem. Phys.* **103**, 1886 (1995).

[181] Gallo, P. and Rovere, M. Structural properties and liquid spinodal of water confined in a hydrophobic environment. *Phys. Rev. E - Stat. Nonlinear, Soft Matter Phys.* **76**, 061202 (2007).